Universidade de Santiago de Compostela
FACULTAD DE FÍSICA
Departamento de Física de Partículas

An investigation into quasi-free scattering of light neutron-rich nuclei around N=14

Paloma Díaz Fernández

Septiembre de 2013

Universidade de Santiago de Compostela
FACULTAD DE FÍSICA
Departamento de Física de Partículas

An investigation into quasi-free scattering of light neutron-rich nuclei around N=14

Memoria presentada por:
Paloma Díaz Fernández
como disertación para optar al
Grado de Doctora
en Ciencias Físicas
Septiembre de 2013

UNIVERSIDADE DE SANTIAGO DE COMPOSTELA

Héctor Álvarez Pol, Profesor Titular del Departamento de Física de Partículas de la Universidad de Santiago de Compostela,

CERTIFICA:

que la memoria titulada **An investigation into quasi-free scattering of light neutron-rich nuclei around N=14** ha sido realizada bajo su dirección por **Paloma Díaz Fernández** en el **Departamento de Física de Partículas de esta Universidad**, y constituye el **Trabajo de Tesis** que presenta para optar al **Grado de Doctora en Ciencias Físicas**.

Santiago de Compostela, a 26 de Septiembre de 2013

Fdo. Héctor Álvarez Pol

Contents

Chapter 1

Introduction

Nuclear physics investigations began in 1911 when Ernest Rutherford discovered that each atom contains a positively charged nucleus [1]. Each nucleus is characterized by its number of protons (Z) and its number of neutrons (N). An element can have more than one isotope (same Z but different N). Since the initial discovery of the nucleus, more than 2800 isotopes have been identified and it is predicted that more than 7000 live long enough to be observed [2]. Figure 1.1 shows the experimentally known nuclei, representing the number of protons vs. the number of neutrons. In this image, the stable isotopes are shown as black cells, while the other square cells represent the radioactive isotopes, the color relating to their half-lives.

The first section of this chapter is a brief overview about the models which have tried to describe the nucleus throughout history, predominantly: the "liquid-drop model" and the "shell model". The first tries to explain the macroscopic properties of the nuclei, while the second focuses on the microscopic ones. Technological advances since the 80's have allowed the exploration of the nuclei far from β-stability where new phenomena appear and modifications of these models are needed to explain these new observations. Later, some aspects concerning how the structure of the nuclei are studied through nuclear reactions will be outlined, to focus in the next section on the reaction mechanism used in this work; namely quasi-free scattering.

The last section of this chapter is dedicated to explain the aim of this work and to summarize the structure of the dissertation.

1.1 Nuclear structure

The first model trying to describe the general properties of the nucleus (binding energies, sizes, shapes, etc.) used the similarity of the nucleus with
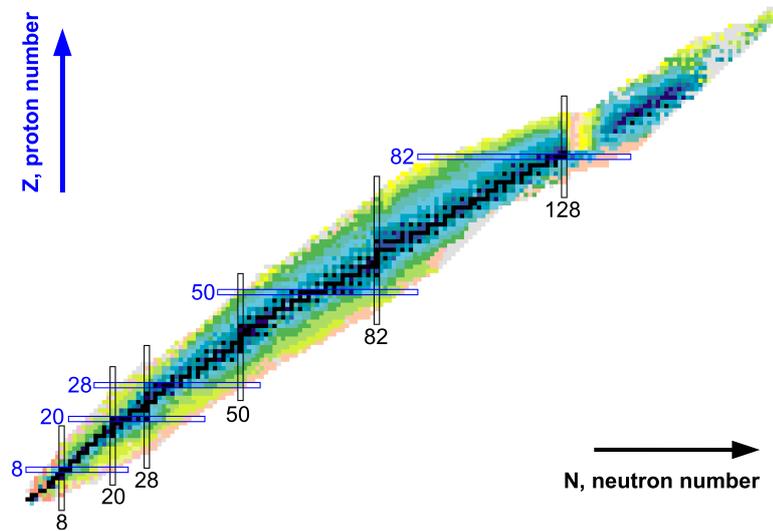
Figure 1.1: The chart of nuclides, showing the number of protons (Z) against the number of neutrons (N). The stable isotopes are indicated by black cells. The other cells represent the radioactive isotopes that have been observed. The color of the cells indicate the half-life of the isotopes. Image taken from National Nuclear Data Center, information extracted from the Chart of Nuclides database, http://www.nndc.bnl.gov/chart/.

a drop of liquid leading to its name "liquid-drop model" [3]. In this context, the nucleus is described as an incompressible liquid drop, made by nucleons which stay together because of the nuclear force. But this model was not able to reproduce the properties of the lighter nuclei and also showed strong deviations at certain neutron and proton numbers. The existence of some nucleon numbers which exhibit high abundance and are very stable was observed by M. Goeppert Mayer [4] and also in an independent work by J. H. Jensen et al. [5]. These nucleon numbers 2, 8, 20, 28, 50, 82 and 126 (only for neutrons) are known as *magic numbers*. Among the above mentioned properties, the *magic* nuclei also present a high first excited state energy and a weak electrical quadrupole momentum. This evidence suggested that the nuclei, like the atoms, have a shell structure. A new model called "the shell model" was postulated, where the nucleons, which are fermions, may occupy the shells in pairs, allowing to explain even/odd Z and N effects known from experimental results. Magic nuclei have a full outer shell and are characterized by a large energy gap to the next available shell. To reproduce all the magic numbers, the model includes an *strong spin-orbit interaction* [6].
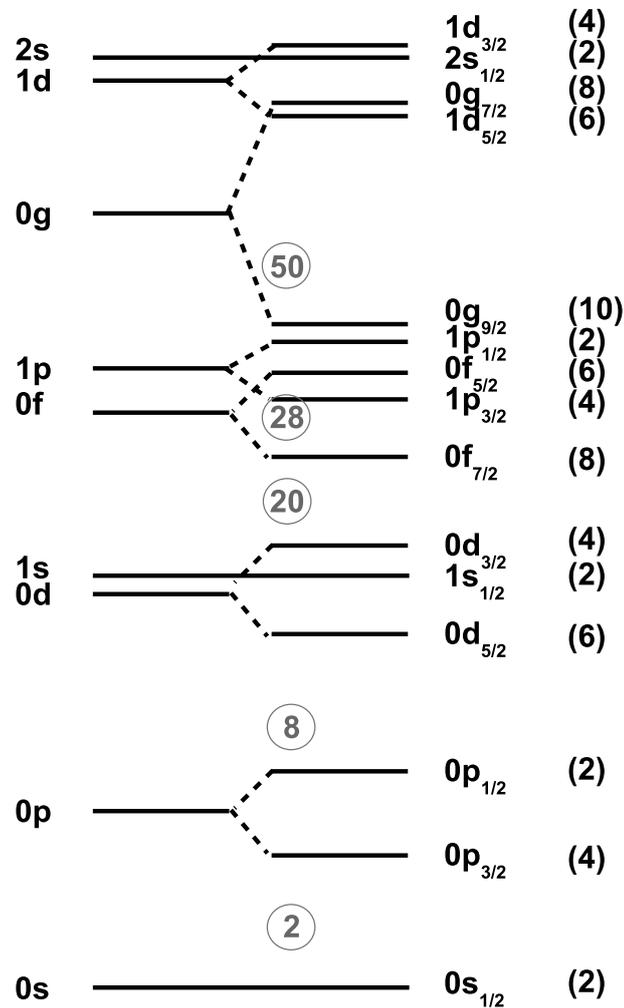
Figure 1.2: Schematic view of the energy levels in a single-particle shell model with harmonic oscillator and spin-orbit coupling terms. For each level are indicated the quantum numbers: n, l and j. Inside the parenthesis are given the maximum occupancies for each shell. Above the levels, (in a circle) are indicated the magic numbers. This figure is based on one from [2].

The single-particle energies in a shell model with a harmonic oscillator potential and spin-orbit interaction are shown in figure 1.2. For each level are indicated the principal quantum number n, the orbital angular momentum l and the total angular momentum j (j = l + s); inside parenthesis the number of nucleons which can occupy each shell, given by (2j+1); above the levels (in a circle), are indicated as well the *magic numbers* (circled).

In general, the shell model explains very well the nuclear structure of

nuclei close to the stability line. In those stable nuclei, the magic numbers predicted by Mayer and Jensen are valid, but when we move to exotic nuclei, which are nuclei close to the drip-lines, the large energy gaps characterizing magic nuclei are not that pronounced or even disappear. As a result, some exotic nuclei that were expected to be magic are not and others, which were not expected, are.

In the recent decades, new facilities were able to produce fast radioactive beams, allowing the investigation of regions far from the β-stability valley. The experimental research with this type of beams started at Lawrence Berkeley National Laboratory in California in 1979 [7]. From those days to the present date, important discoveries have been made in nuclear structure.

In 1985 an experiment performed by Tanihata and collaborators [8] showed for the first time the experimental evidence for a type of nuclei that would be called later "halo nuclei". The first observed nucleus with halo was ^{11}Li. Halo nuclei have a larger radii compared with their expected values, indicating an extended wave function of the valence nucleons [9]. Years later, knockout experiments performed at MSU allowed to extract spectroscopic information on exotic nuclei [10]. In these type of reactions, a fast projectile impinges in a target at rest. If the impact parameter is large enough, the projectile would breakup into one or more nucleons that will be emitted at large angles, and a core (spectator) that will not be affected by the reaction and will continue its trajectory with almost the same energy than the projectile. These type of reactions allow to study the external part of the wave function. Later, other laboratories like GSI [11], GANIL [12] and RIKEN [13] have been using exotic beams to study the nuclear shell properties.

All these works have shown that the magic numbers are not as universal as it was thought; they evolve when we move far from the stability. According to the shell model, ^{11}Li would be a magic nucleus, with the two valence neutrons in the orbital $0p_{1/2}$. But this is not in agreement with the experimental observation of its large radius. It was found that this nucleus has a mixture of the $0p_{1/2}$ and the $1s_{1/2}$ shells, making disappear the magicity of the N = 8. Another example of an expected magic number which can not be confirmed by experiments occurs at N = 20 for the oxygen isotopes. There is no evidence for the ^{28}O to be bound. The isotopic chain of the oxygens finishes with the ^{24}O which was found to be a doubly-magic nucleus, and N = 16 a new magic number. Experimentally it was observed for the ^{24}O that the valence neutrons mainly populate the $1s_{1/2}$ orbital, creating a large gap between the $1s_{1/2}$ and $0d_{3/2}$ orbits making this nucleus doubly magic [14, 15, 16]. It has been observed [17] that the first excited state energy for the ^{22}O is relatively high making the N=14 to be a sub-shell closure for the oxygen isotopes. This behaviour seen in N = 14 is not observed with the

same strengh for the ^{21}N [18, 19] and it is vanished for the ^{20}C [20].

Quasi-free scattering is a technique that was used in the past, and is being used nowadays to explore the nuclear structure. This reaction mechanism offers the possibility to study not only the outer part of the wave function, but allows the exploration of deeper regions inside the nucleus. In the following sections the quasi-free scattering mechanism will be explained in more detail.

1.2 Direct reactions for nuclear spectroscopy

There are three types of direct reactions which are particular suitable to study the single-particle properties of the nuclei: transfer reactions, nucleon removal and quasi-free scattering. These reactions have shown along history a great success in disentangling the structure of nuclei.

Transfer reactions occur when a projectile and a target exchange one or more nucleons. They are useful to study the outer shells of the nuclei [9].

One-neutron knockout reactions study the external part of the wave function. They will be discussed here in more detail than the transfer reactions (due to their similarity with the quasi-free scattering) are . As it was mentioned in the previous section, these reactions have been used to study the "halo" nuclei and the single-particle properties of exotic nuclei. The information obtained in experiments, combined with theoretical models of the reaction mechanism, allow the determination of the single-particle occupancies (exclusive cross sections) and the orbital angular momentum of the states (momentum distributions).

The one-neutron knockout reactions have three contributions to their cross sections: Coulomb breakup, diffractive breakup and neutron stripping. The first contribution includes Coulomb dissociation and can be neglected as long as light targets as Be or C are used. The second term accounts for the dissociation of a nucleon from the projectile via a two-body process with the target. The last contribution is neutron stripping and includes events where a nucleon of the projectile reacts with the target being excited from its ground state.

The stripping and diffractive cross sections are calculated using eikonal or Glauber theory, where two approximations are assumed. The first one is that the projectile has a relatively high velocity, so the reaction is very fast and we can neglect the no internal motion of the nucleons inside the nucleus during their interaction time with the target (they are considered as spectators). The other approximation is called eikonal and assumes that the survival nucleus follows a straight line.

The single-particle cross section is given by (once the Coulomb part is

taken out)

$$\sigma_{s-p} = \sigma_{s-p}^{diff} + \sigma_{s-p}^{str} \tag{1.1}$$

where σ_{s-p}^{diff} and σ_{s-p}^{str} are the single-particle cross-sections corresponding to the diffraction and stripping processes. The two components are calculated as integrals on the impact parameter [21].

The occupancies of the single-particle states are calculated by measuring the absolute spectroscopic factors. If γ rays stemming from the deexcitation of the fragment were measured, their coincidence with the fragment allows the determination of the contributions to the single-particle states. The spectroscopic factors $C^2 S\left(I^\pi, nlj\right)$, which are proportional to the cross sections and measure the overlap between the initial and final state I^π, can be determined as follows,

$$\sigma(I^\pi) = \sum_j C^2 S\left(I^\pi, nlj\right) \sigma_{s-p}\left(I^\pi, nlj\right) \tag{1.2}$$

To conclude, the use of one-neutron removal reactions allows to determine the cross sections for each state, their spectroscopic factors and the angular momentum of the removed nucleon from the fragment momentum distribution.

The third type of reactions of interest on the study of the single-particle properties will be the quasi-free scattering described in the next section.

1.3   Quasi-free scattering

A quasi-free scattering reaction is a direct reaction where a bound nucleon (proton or neutron) or a cluster (^{2}H, ^{4}He, ^{8}Be) in a nucleus ^{A}Z, is knocked-out by a high energy particle (100-1000 MeV) (proton (p,2p) or electron (e, e′p)) and without interaction between the nucleus and the projectile or the two outgoing particles [22, 23]. The description of this type of reactions was given in 1952 at the Berkeley laboratory by O. Chamberlain and E. Segrè and J. B. Cladis, W. N. Hess, and B . J. Moyer [24, 25].

These experiments shown that when light targets (lithium [24] or deuterium, carbon and oxygen [25]) are bombarded with a proton beam with an energy of 350 MeV, proton pairs emerge from the collision sharing an opening angle of approximately 90°. This is explained by the assumption of the incoming protons impinging upon a proton in the nucleus as if both particles were free. The opening angle of both particles is not exactly 90° (free scattering) because the collision takes place in the presence of nuclear

matter where the proton in the target is not at rest and it has a momentum distribution. Later in 1957, an experiment performed by Tyren, Maris and Hillman [26] not only proved the validity of the quasi-free interaction between protons, but also demonstrated that it is a very interesting tool to study the inner nuclear shell structure. Other experiments performed later have confirmed the previous results and also that the removed particle in the nucleus could be a deuteron, an alpha, etc.
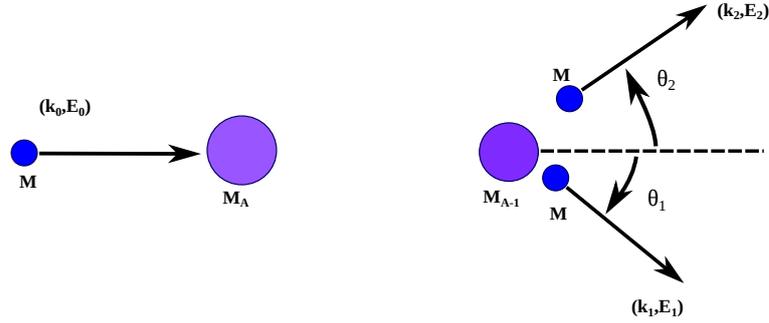
Figure 1.3: Schematic view of a quasi-free scattering reaction. The incoming fast proton M collides with a target of mass M_A leaving a hole in the residual nucleus and removing a nucleon (or a cluster). The two outgoing particles share an opening angle of about 90°.

To discuss about the kinematics, the projectile will have a subscript 0: its energy and momentum will be E_0 and $\vec{k}_0$, respectively. It collides with a bound nucleon (or cluster) as if both particles were free, leaving a hole in the residual nucleus. The separation energy of a nucleon or a cluster inside a nucleus can be written as follows,

$$B = T_0 - (T_1 + T_2 + T_{A-1}) \tag{1.3}$$

where T indicates the kinetic energy of the particles. The indices A and A-1 denote the initial and residual nucleus. The indices 0, 1 and 2 denote the incident proton and the two outgoing nucleons.

From energy-momentum conservation:

$$E_0 + M_A c^2 = E_1 + E_2 + E_{A-1} \tag{1.4}$$

$$\vec{k}_0 = \vec{k}_1 + \vec{k}_2 + \vec{k}_{A-1} \tag{1.5}$$

with

$$E_{A-1} = M_{A-1} + E_{exc} + T_{A-1} \tag{1.6}$$

E_{exc} being the excitation energy of the residual nucleus. The recoil momentum of the M_{A-1} fragment is the same opposite in sign as the momentum of the knocked-out nucleon ($\vec{k}_3$) when it was bound in the nucleus before the collision.

$$\vec{k}_{A-1} = \vec{k}_0 - \vec{k}_1 - \vec{k}_2 = -\vec{k}_3 \qquad (1.7)$$

Using quasi-free scattering reactions it is possible to study not only the surface of the nuclei, like in knockout reactions but also the inner regions of the nuclei.

In recent experiments performed at GSI Helmholtzzentrum für Schwerionenforschung, in Darmstadt, Germany [11] within the R^{3}B collaboration [27], inclusive and exclusive measurements of (p,2p) in inverse kinematics using the LAND-R^{3}B setup have been carried out. In these experiments with rare beams in inverse kinematics, the nucleus of interest is the projectile due to the difficulty to have stationary targets made of unstable isotopes. The use of inverse kinematics present some advantages. A difference with the reactions in direct kinematics, the fragments produced here in the reaction escape from the target due to their high velocities making possible to measure their energies and angles after the reaction. Reactions such ^{12}C(p,2p)^{11}B [28, 29] and ^{17}Ne(p,2p)^{16}F→^{15}O+2p [30] have already been studied, probing the validity of this technique.

In the first example, a ^{12}C beam at 400 AMeV was guided to the experimental area. The setup was very similar to the one used in the experiment analyzed in this work, so it will only be outlined. The beam impinges upon a CH$_2$ target, which was surrounded by silicon detectors allowing for identification of the two protons from the reaction and the measurement of their angular distributions and energies. The target and the silicon detectors were inside a vacuum chamber surrounded by a 4π calorimeter to obtain exclusive observables by measuring the γ rays. The outgoing fragments were deflected by a large acceptance magnet and identified in the three branches located behind it, one for neutrons, one for heavy fragments and one for protons. The energy differential cross section obtained for ^{11}B is shown in figure 1.4. In this plot the different breakup channels studied are included together with the γ rays. The results are found to be in very good agreement with previous experiments studying the same reaction in direct kinematics (see references [28, 29] for more information).

For the second example, a ^{17}Ne beam at 500 AMeV has been used to study this borromean nucleus. Borromean nuclei are formed by three components; if one of them is separated from the others, the other two become unbound (^{15}O+p+p). When a proton is removed from the ^{17}Ne, the ^{16}F decays into
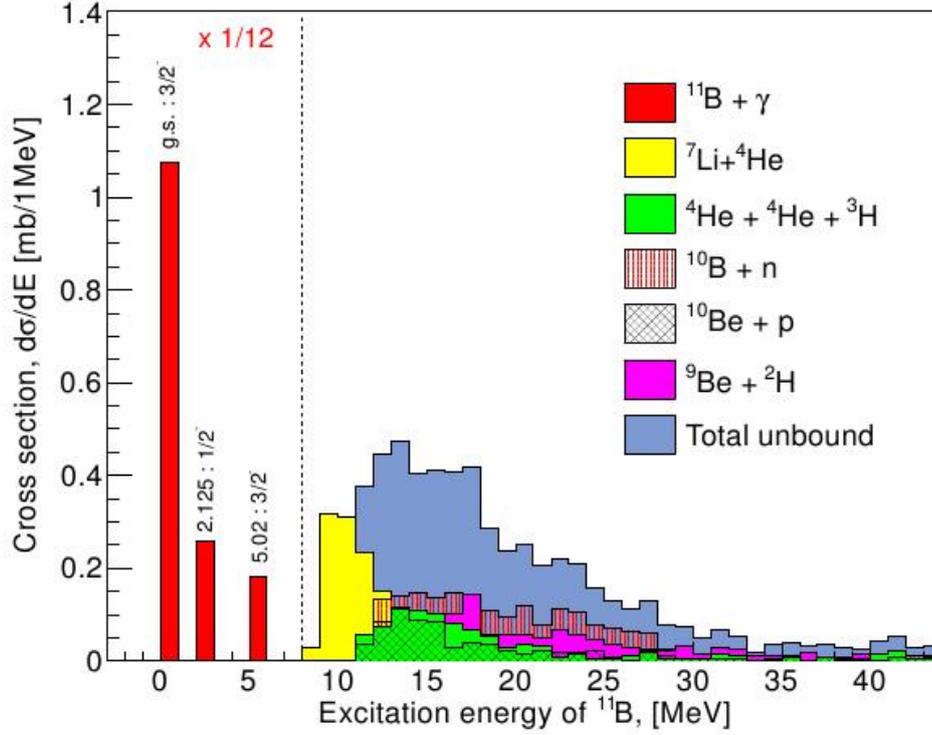
Figure 1.4: Excitation energy spectrum for the ^{11}B. The different decay channels are shown in different colors. Figure taken from [28].

^{15}O+p. This nucleus was investigated in inverse kinematics via electromagnetic dissociation, one-proton removal and quasi-free scattering. Using this reaction mechanism, the excitation energy spectrum for the ^{16}F (^{15}O+p), the inclusive two-proton removal cross sections for ^{17}Ne→^{15}O+X and transverse momentum distributions of ^{16}F were extracted. From the comparison of the momentum distributions with theoretical calculations the spectroscopic factors were also obtained, finding good agreement with previous experiments (see [30] for more details).

These two experiments have demonstrated that this reaction type is a very good tool to study the nuclear structure of exotic nuclei. The future FAIR [31] facility will open new investigations with exotic beams, where the R^{3}B setup will be located. This also includes important improvements with respect to the actual LAND-R^{3}B setup [32].

1.4   This work

Quasi-free scattering reactions have been used in this work to study the nuclear structure of light neutron-rich nuclei around N = 14 for charges 7 and 8. The same projectiles, ^{23}O, ^{22}O and ^{21}N have been investigated through (p,pn) and (p,2p) reactions in complete and inverse kinematics, allowing the investigation at the same time of both valence nucleons and also deep-hole states. Thus, a complete study of the whole wave function would be in principle possible.

The experiment [33] was performed in the LAND/R^{3}B reaction setup in August-September, 2010, at GSI Helmholtzzentrum für Schwerionenforschung, in Darmstadt, Germany [11]. The studied physics topics are very diverse including the measurement of astrophysical reaction rates relevant for r-process nucleosynthesis using heavy-ion induced electromagnetic excitation and quasi-free knockout reactions to study the evolution of shell and cluster structures close to and beyond the dripline. Unbound (ground and excited) states could be populated and identified in (p,2p) reactions. The quenching of single-particle strength in neutron-proton asymmetric nuclei will be addressed by knocking out deeply bound protons and neutrons in (p,2p) and (p,pn) reactions for nuclei with varying neutron-proton asymmetry. The analysis of the complete set of data is still in progress, but the first results have already been presented in dissertations [34] and conferences, like for example [35, 36, 37, 38].

The details about the experimental setup, including a description of each detector, will be given in Chapter 2. The following chapter will explain the calibration procedures used for the different detectors. Chapter 4 will be devoted to the procedures used to identify and study the different reaction channels. The fifth chapter will be dedicated to explain and show the results obtained in simulation. The sixth and seventh chapters will show and discuss the results obtained for the studied reactions which are mainly: inclusive momentum distributions of the (p,pn) and (p,2p) channels, inclusive cross sections of the (p,pn) and (p,2p) channels, the deexcitation γ rays spectra measured in coincidence with the outgoung fragments and the excitation energy distributions for the one neutron breakup channels.

Chapter 2

Experimental Setup

In August 2010, the S393 [33] experiment was performed at the laboratory GSI Helmholtzzentrum für Schwerionenforschung, in Darmstadt, Germany. The main goal of this experiment was to study light neutron-rich nuclei using inverse and complete kinematic measurements via quasi-free scattering reactions at relativistic energies. In about twenty days, data for six different settings centred at different A/Q ratios, were collected in the LAND-R^{3}B experimental area at Cave C. Within this chapter the main features of the beam production and the experimental setup will be described in detail.

2.1 GSI Helmholtzzentrum für Schwerionenforschung GmbH

GSI[1] is a laboratory located near Darmstadt, in Germany. A schematic view of the facility at 2010, when the experiment was performed, is shown in Fig. 2.1.

A primary beam is produced in an ion source and injected in the linear accelerator UNILAC (UNIversal Linear ACcelerator). In our case the primary beam was ^{40}Ar. This ^{40}Ar^{+11} beam is then inserted in the SchwerIonenSynchrotron (SIS-18) where it is accelerated to the desired energy. In our case the primary beam leaves the SIS with an energy of about 490 AMeV and goes to the FRagment Separator area (FRS), a high resolution forward spectrometer [39]. At its entrance there is a production target of Be, 4.011 g/cm^2. When the primary beam impinges upon this target, a range of ions are produced by nuclear fragmentation. The FRS separates the species of interest depending on their mass-to-charge ratio (A/Q): when a particle

---

[1]http://gsi.de/portrait/index.html
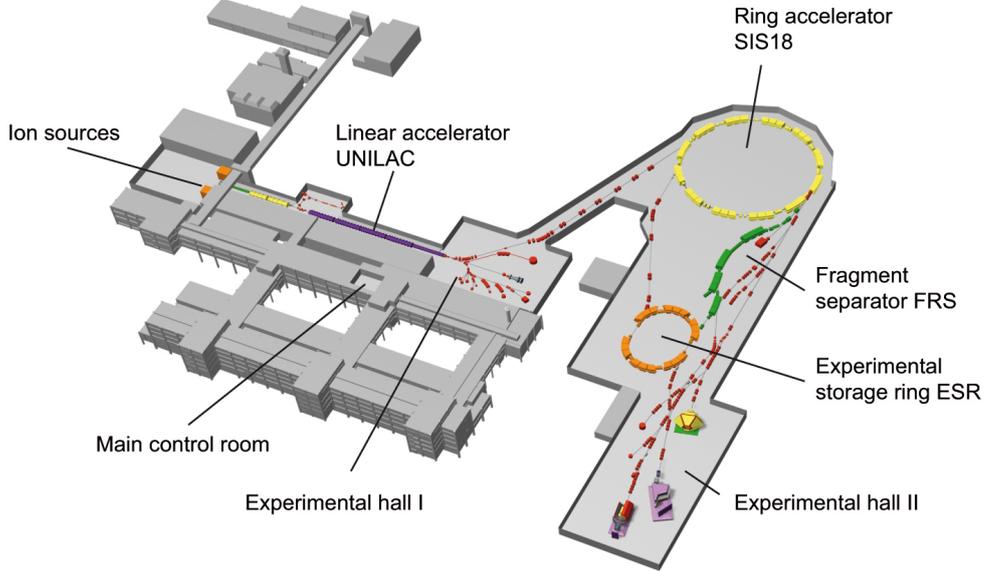
Figure 2.1: Schematic view of the GSI facility in 2010. The LAND-R^{3}B experimental area is located in the *Experimental Hall II.*

with charge Q and mass A travels through a magnetic field of strength B it experiences the Lorentz force. Also, if the initial particle velocity β is perpendicular to the uniform magnetic field into which it is moving, the magnetic force will have the characteristics of a centripetal force, and the particle will move in a circle of radius ρ, with

$$B\rho = \frac{p}{Q} \propto \frac{A}{Z} \cdot \beta\gamma \tag{2.1}$$

where p is the momentum of the particle, Q was replaced by Z due to the non existence of charge states and γ is the Lorentz factor. The formula shows that only ions with a given A/Z ratio will follow the trajectory determined by the beam line.

The selection of the ions of interest is made in two stages (see figure 2.2). In the first one, where two dipoles and a plastic scintillator (S2) are involved, the magnetic rigidity of the fragments produced in the target is determined. Only fragments with an appropriate combination of mass, charge and velocity are transmitted. At the intermediate focal plane a degrader is placed to slow down the beam in order to enable a finer selection. In the second
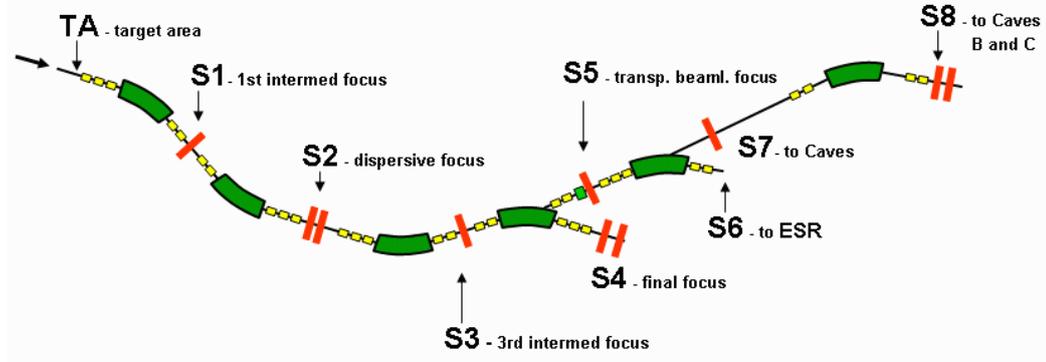
Figure 2.2: Schematic drawing of the FRS. The beam coming from the SIS arrives to the target area (TA). The fragment selection is performed in two stages. Every stage contains two dipoles (indicated in green). The last detector of the FRS is the scintillator paddle S8.

stage, formed by other two dipoles and an additional plastic scintillator (S8), the fragments are selected according to their A/Z ratio by their velocities (determined from time-of-flight) and their magnetic rigidities. After the last scintillator (S8) the secondary beam (also called "cocktail beam" because of the presence of different species) is identified in mass, atomic number and velocity.

2.2 ALADIN-LAND setup

After the last scintillator of the FRS area, the beam travels around 55m to Cave C where the LAND - R^{3}B setup is placed. In figure 2.3 a schematic layout of the setup is shown. The velocity of the beam is measured by using the last scintillator of FRS and the first detector of Cave C, which is another scintillator read-out by two photomultipliers. An active collimator called ROLU is used to center the beam. After ROLU, for tracking and energy loss measurements, a position sensitive silicon detector, PSP, is placed. The beam, then, enters a vacuum chamber where the target, surrounded by eight silicon detectors is located. The chamber is embedded in the Crystal Ball, a 4π calorimeter. After the reaction, the products travelling in forward directions are deflected by the ALADIN magnet and, according to their mass and charge, are going to one of three branches: neutrons are not deflected and are detected by LAND; heavy fragments are tracked via two scintillating fibre detectors GFIs, and a time-of-flight wall TFW; protons are bent further and detected via two proton drift chambers PDCs and a time-of-flight wall

DTF.
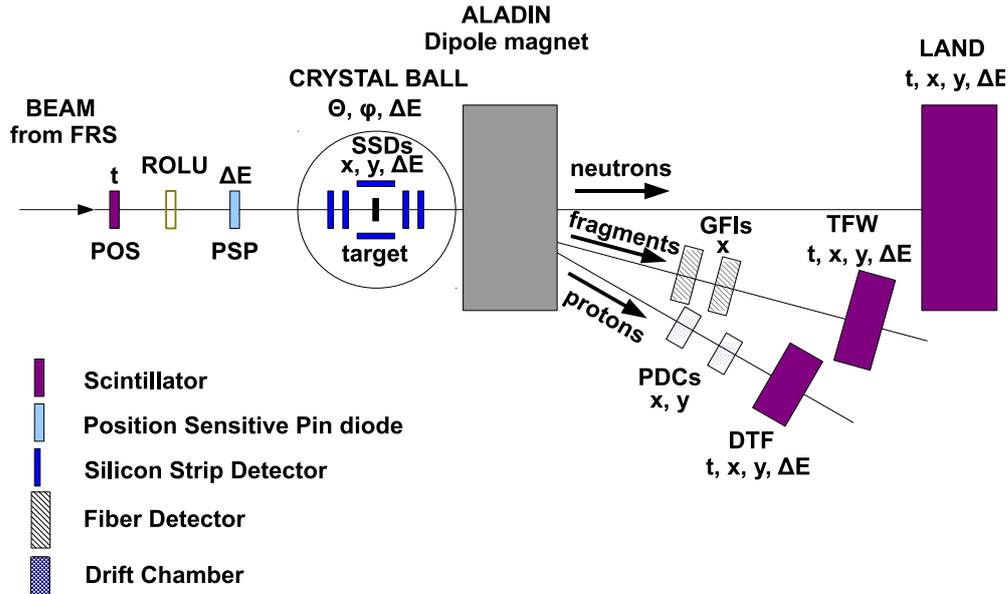
Figure 2.3: Schematic draft of the experimental setup for the S393 experiment in Cave C (not to scale). The beam comes from the left and finds the following detectors: POS: together with a plastic scintillator detector from the FRS measure time-of-flight which allows to determine the velocity of the fragments, it can also be used to determine the position of the particles; ROLU: 4 movable plastic scintillators, define the accepted beam spot size; PSP: provides energy loss information of the incoming beam from which the charge is obtained; SSDs: used to track and identify the fragments and the quasi-free scattering nucleons; Crystal Ball: array of NaI detectors, γ rays and quasi-free scattering nucleons detection in $\sim 4\pi$; ALADIN: large acceptance dipole magnet to bend the particles depending on their A/Q; LAND: tracking and determination of the momentum of the neutrons; GFI's: used to track the heavy fragments; TFW: tracking, energy loss and time-of-flight measurements of the heavy fragments; PDCs: used for the tracking of the protons; DTF: tracking, energy loss and time-of-flight measurements of the protons.

2.2.1 Incoming beam detectors

The secondary beam needs to be identified in charge and mass. In order to do that, four incoming detectors were used. The names of these detectors are S8, POS, ROLU and PSP.

- S8 is a scintillator formed by one paddle and used for the time-of-flight (ToF) measurements. The time signals are provided by two photomultipliers located at both ends of the paddle.

- POS (see Fig. 2.4) is a scintillator with square shape, 5.5x5.5 cm^2, used as start for the time-of-flight measurements. The scintillation light produced in the detector is read-out by four photomultipliers, which deliver time and amplitude signals.
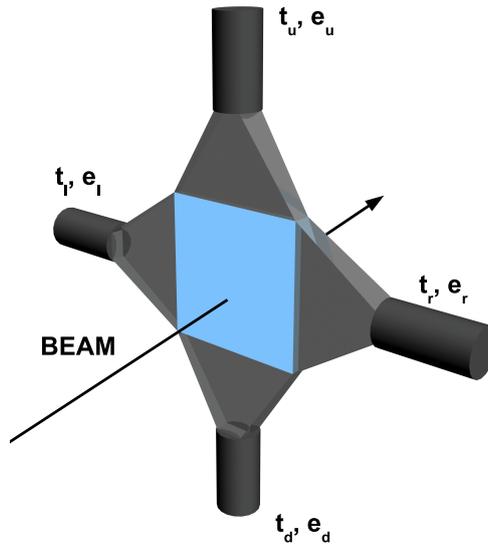
Figure 2.4: Schematic view of POS detector with the direction of the beam indicated. The four photomultiplier outputs provide time and amplitude information, used to calculate time-of-flight, position and energy loss.

- ROLU ("Rechts", "Oben", "Links", and "Unten") (see Fig. 2.5) is a detector comprising four movable plastic scintillators used to define

the beam spot size. Each scintillator is read-out by a photomultiplier and can be moved in order to define the size and position of the beam, acting as a veto for all the particles hitting the scintillators.
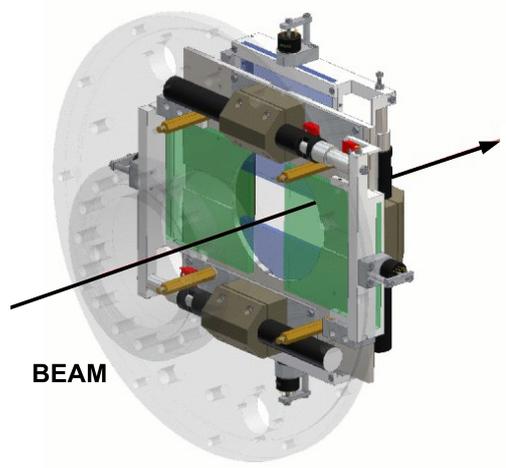
BEAM

Figure 2.5: Schematic layout of ROLU, with the beam direction indicated, which is formed by four movable plastic scintillators which define the beam size on the target.

- PSP (the figure 2.6) is a Position Sensitive silicon Pin diode with square shape and an active area of 4.5x4.5 cm^2. The detector has four anodes that provide position information (x,y) and one cathode providing the energy loss of the ion which is related to its charge Z via the Bethe-Bloch formula

$$-\frac{dE}{dx} = \frac{4\pi Z^2}{m_e c^2 \beta^2} \frac{N_a Z \rho}{M_u} \left(\frac{e^2}{4\pi\epsilon_0}\right)^2 \left[ln\frac{2m_e v^2}{I} - ln\left(1 - \frac{v^2}{c^2}\right) - \frac{v^2}{c^2}\right]$$

(2.2)

where E is the energy of the particle, x the distance travelled by the particle, m_e the electron rest mass, c the speed of light, v the velocity of the particle, N_a the Avogadro's number, e the electron charge, ϵ_0
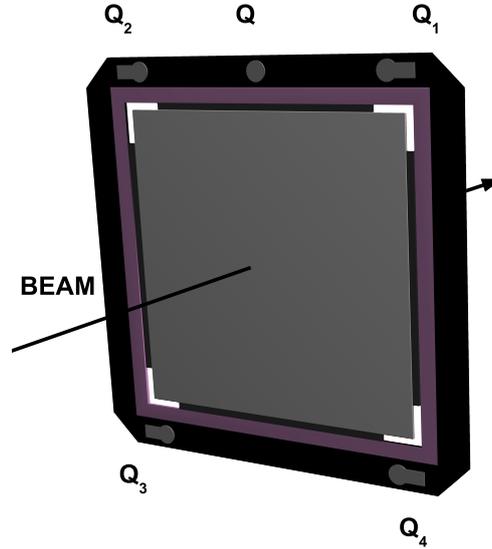
Figure 2.6: Schematic view of PSP detector. The detector has four anodes to reconstruct the position of the ions (Q_1, Q_2, Q_3 and Q_4), and one cathode (Q) which is used to identify the ions in charge.

the vacuum permitivity, $\beta = \frac{v}{c}$ and I, Z, A, M_u and ρ are the mean excitation potential, the atomic number, the mass number, the molar mass and the density of the target respectively. The energy resolution of the PSP is around 1%. The position is calibrated using a mask attached to the detector with 21x21 square pixels made of scintillator material that can be moved by remote control. For this experiment the pixel mask did not work, so the position information could not be used.

The flight time of the particle is measured between S8 and POS. This information is used together with the energy loss in the PSP detector for incoming particle identification.

2.3   Detectors surrounding the target

There was a $\sim 4\pi$ spherical calorimeter made of 159 NaI (Tl) crystals (~ 20 cm long) surrounding the target, used for detection of γ rays, protons and neutrons (energies, angular distributions and multiplicities). Inside a vacuum reaction chamber, there was eight Silicon Strip Detectors, four of them setting up a box around the target and dedicated to angular measurements. The other four are located in the beam axis in pairs, before and after the target. They are used to track the incoming beam and fragments and also for charge identification. Both detectors are defined in the following subsections.

2.3.1   Silicon Strip Detectors

The configuration of the SSDs used in this experiment is shown in Fig. 2.7. These detectors were developed for tracking in the X and Y direction, (transversal to the beam), for charged particles as protons and heavy ions. But they also deliver energy loss information allowing charge identification [40]. The detectors were originally designed with the purpose of tracking high-energy cosmic rays (protons up to Fe nuclei) at the Alpha Magnetic Spectrometer (AMS) to be mounted at the International Space Station (ISS).
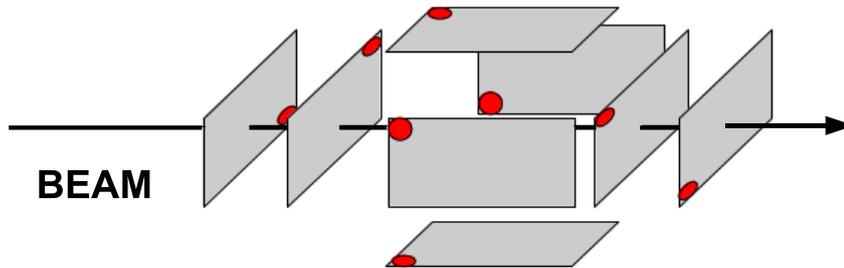
Figure 2.7: Silicon Strip Detectors configuration in the S393 experimental setup. The red dots mark the origin, i.e. where the first strip is located.

Each SSD (see figure 2.8) has an area of 72x40 mm^2 and a width of 300 μm. As the main purpose is to measure coordinates in the silicon plane, each detector has two sides (S and K), perpendicular to each other. The S-side (p-side, using the semiconductor nomenclature labelling the dopant content) has the largest dimension. It has an implantation pitch of 27.5 μm and a
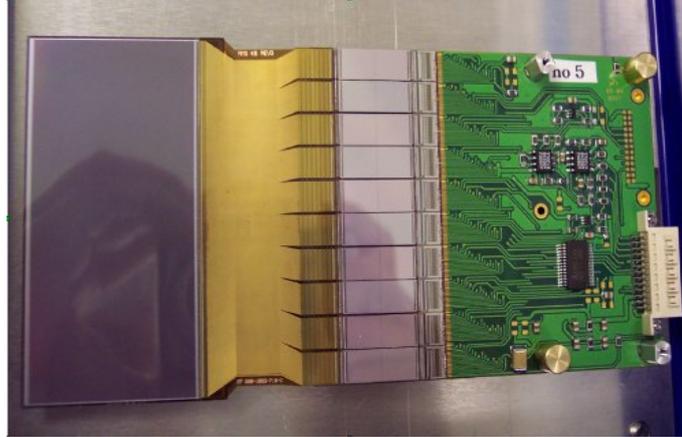
Figure 2.8: Picture of one of the SSDs detectors. From left is shown the sensor, the capton cable, the coupling capacitors, the read-out VA chips, the front-end electronics board, and the 26-pin S-side connector.

read-out pitch of 110 μm. The number of strips in this side is 2560, being every fourth strip connected to a read-out channel (640), while the others are left floating. The other side is called K (or n-side), corresponding to the shortest dimension (40 mm length). For this side the implantation pitch is 104 μm and all the strips are read-out (384). The number of strips being read-out in every SSD is 1024.

2.3.2 Crystal Ball (XB)

The target was surrounded by a $\sim 4\pi$ calorimeter called Crystal Ball [41]. The main aim of this detector is to study the γ's, protons and neutrons coming from excited nuclei (see figure 2.9). The total energy, the multiplicity and the angular distributions of the γ radiation emitted by the nucleus are used together with other observables to study the internal structure of the nuclei.

This detector is formed by 162 crystals of NaI (Tl) of 20 cm length, each inside an aluminum shell of 600 μm. Only 159 crystals were used, leaving space to let the beam pass through and to hold the full structure. The crystals have four different shapes: 12 regular pentagons and 150 irregular hexagons (with three different types divided into 60, 60 and 30). Every crystal is covering the same solid angle of approximately 77 msr. The whole detector is mounted on a structure which allows to move the two hemispheres of the detector individually using rails. Correction of the Doppler broadening is possible because of the relatively high granularity of the detector. The
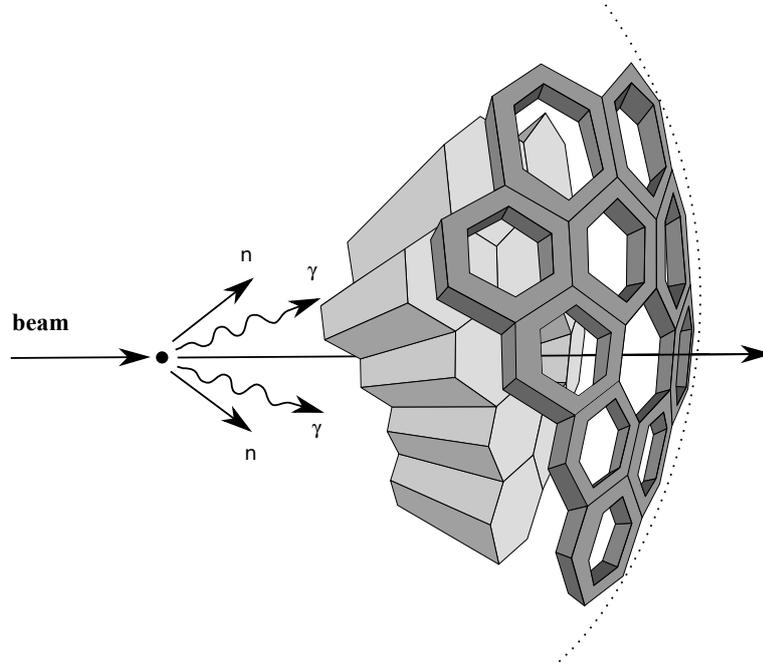
Figure 2.9: Nuclear reaction products travelling to the Crystal Ball detector. The beam entering left impinges on the target.

substantial length of the crystals provides a high detection efficiency. In figure 2.10 is shown a picture of the Crystall Ball detector taken during the S393 experiment.

New electronics for the Crystal Ball were used in this experiment for the first time. The signal from each photomultiplier is divided into two parts: one is for high energy particles, i.e. protons and neutrons, which is extracted in a previous stage of amplification and is delivered to a QDC; the other is for the γ rays. This signal is going to a Mesytec MSCF-16 (16-fold Spectroscopy Amplifier with CFD's and Multiplicity trigger) and after this to a VUPROM (VME Universal PROcesing Module) [42].

2.4   ALADIN

Downstream from the target area a dipole called ALADIN (A Large Acceptance DIpole magNet) deflects the charged fragments to their corresponding paths depending on their magnetic rigidities. These were separated into three different branches for neutrons, heavy fragments and protons. The angular acceptance of ALADIN is ± 60 mrad. The maximum current undertaken by the magnet is 2500 A, but above 1900 A, saturation effects become
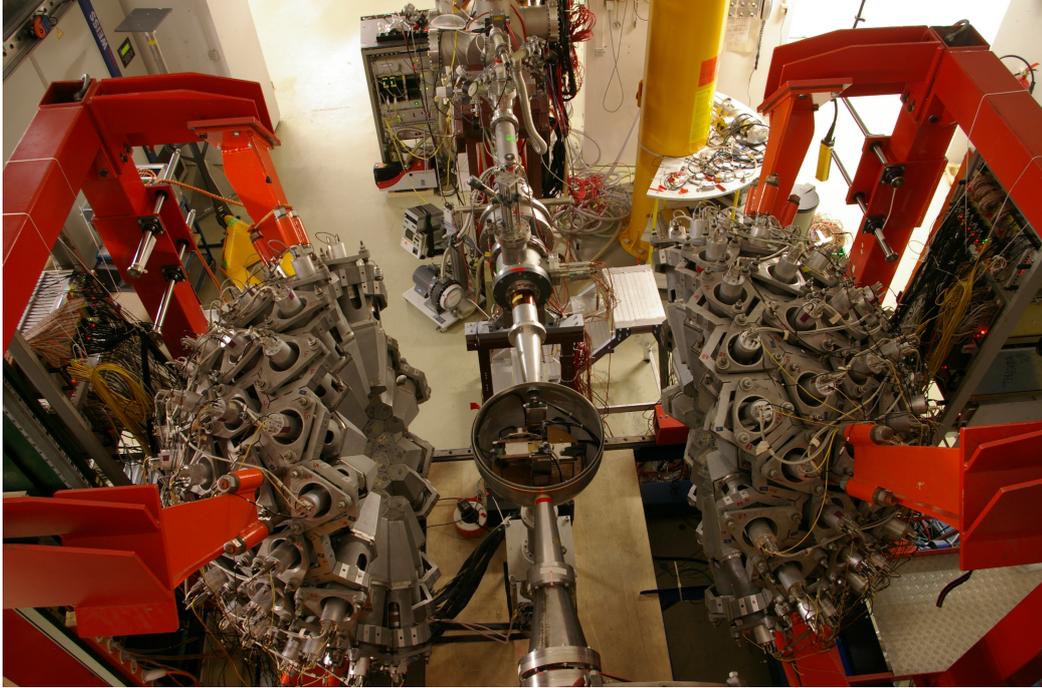
Figure 2.10: Photograph of the Crystal Ball detector opened at Cave C during the preparation of the S393 experiment in 2010. The reaction chamber and some of the incoming detectors are also visible.

not negligible, being the relation between magnetic field and current not linear.

2.5   Heavy ion branch detectors

Following the magnet, and covering a region centered at a deflection of approximately 15°, there is a region where the ions pass through, called the heavy ion branch, formed by three detectors selected for their capability of measuring position, energy loss and time-of-flight. These detectors are the two GFI's and the TFW.

2.5.1   GFIs

The GFI (Große FIber Detektor) detectors are used to reconstruct the trajectories of the heavy fragments. The position resolution of this detector is ∼1 mm with a geometrical efficiency of 89 % for Z≥3. For lower charges the detection efficiency becomes very low [43].

The GFI detectors have a large active area of 50 x 50 cm^2 with almost 500 parallel fibres of 1 x 1 x 500 mm^3. A schematic view of this detectors is shown in figure 2.11. Each fibre has an optical coat to guide the light and to avoid cross talk. One end of each fibre is coupled to a position-sensitive photomultiplier (PSPM) using a mask (see figure 2.11). The other end of the fibre is usually coupled to a common photomultiplier, not used in this experiment.
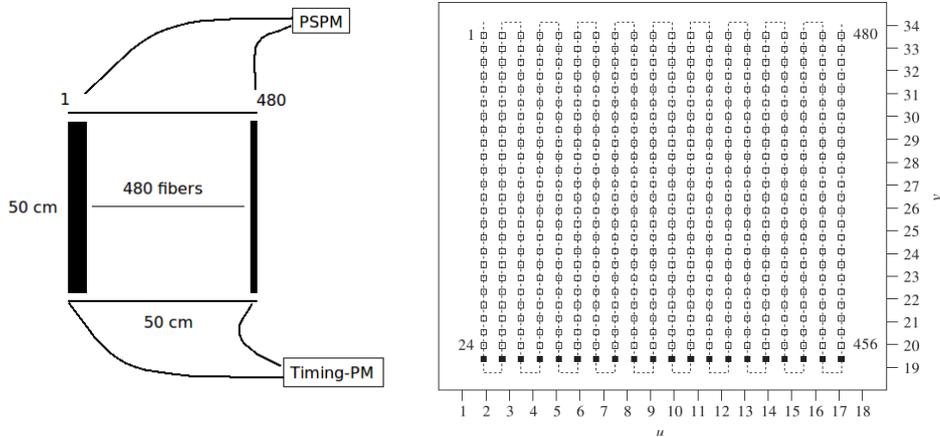
Figure 2.11: Left: schematic view of the GFI. Right: mask used to connect one end of the fibre to the PSPM photomultiplier for the position measurements. The dark squares indicate the non used holes. The dotted line indicates the ordering of the fibres.

The PSPM has a rectangular photocathode with an area of 64 x 58 mm^2, 16 mesh-type dynodes and a rectangular anode grid with 18 wires in the X (u) direction and 16 in the Y (v) direction. The distance between the anode wires is approximately 3.7 mm. The fibres are organized in a 20 x 25 matrix (see figure 2.11). The distance from row to row is 2.2 mm and the distance from column to column is 3 mm. In next chapter we will see that the charge distribution on the anode is related to the position of the light spot on the photocathode.

When the ions hit the GFIs, scintillation light proportional to their energy loss in the detector is produced. This light is guided on the mask producing energy signals in a few wires, which are read-out and used to reconstruct the (u,v) coordinates of the photocathode. Via a coordinate system transformation the horizontal position is obtained.

2.5.2   TFW (Time of Flight Wall)

The Time of Flight Wall (TFW) is used to determine the charge, via energy loss, and to reconstruct the β, via time-of-flight measurements, of the heavy fragments.

The TFW (see figure 2.12) is formed by 32 scintillator modules (paddles). The modules are arranged in two layers perpendicular to the beam direction. There are 18 paddles in the vertical direction, 147 cm long each, and 14 paddles in the horizontal direction, 189 cm long. The paddle thickness is 0.5 cm and the width is 10.4 cm. All the paddles are read-out by two photomultipliers, one on each side.
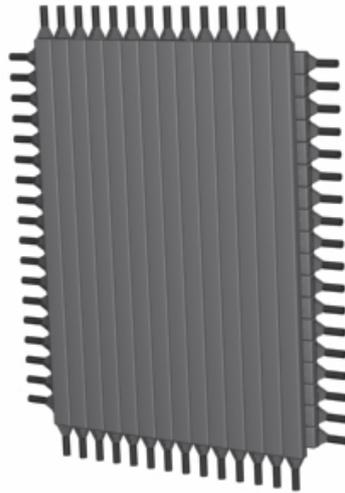
Figure 2.12: Schematic layout of the Time of Flight Wall used in the experiment.

2.6   Proton branch detectors

After the magnet and covering a region centred at a deflection of 30°, the proton branch detectors were placed, to measure the momenta of the protons coming from the reactions at the target via time-of-flight. The detectors used for this purpose are two Particle Drift CHambers (PDCs) for tracking and a Time of Flight Wall (DFT) to determine the velocity of the protons.

2.6.1 PDCs (Proton Drift chambers)

In order to track the protons coming from breakup reactions, two proton drift chambers (PDCs) were placed 2 and 3 m behind the magnet. They are counting gas detectors filled with a gas mixture (20% CO_2 and 80% Ar). The active area of these detectors is 100x80 cm^2. In the widest direction (X) there are 144 sense wires, while in the Y direction there are 112 sense wires. In total this detector has 256 read out channels. Each detector has two layers, each one formed by eight planes, six of field wires defining hexagonal drift cells with a diameter of 16 mm and two of sense wires (see Fig. 2.13). When a charged particle passes through the gas, it produces ionization. The resulting electrons induce a current in the sense wire, causing a localized cascade of ionization which is collected on the wire and results in an electric current proportional to the energy of the detected particle. This allows the determination of the proton trajectory.
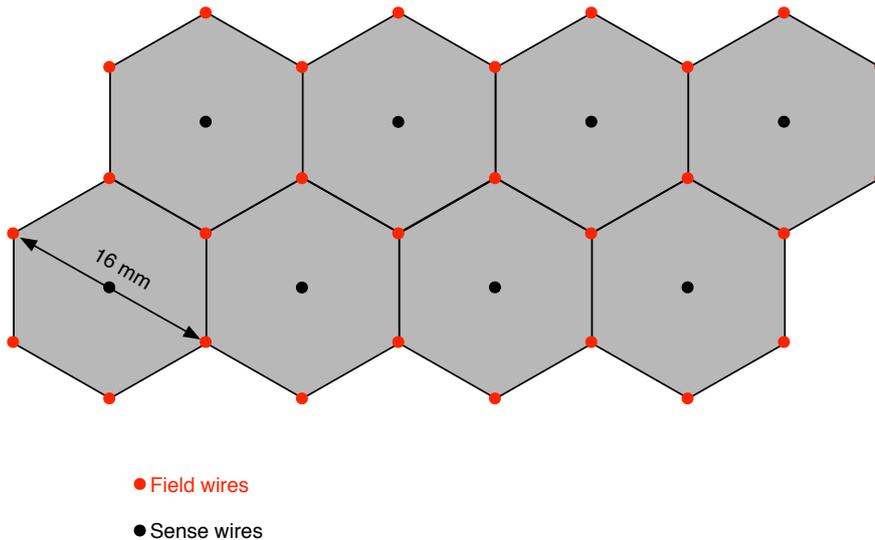
Figure 2.13: Detail of the hexagonal drift cells. The black circles represent the sense wires and the red ones the field wires.

2.6.2 DTF (Dicke ToFwand)

The DTF is a Time of Flight Wall formed by scintillator paddles used to measure the time-of-flight and the energy of the protons (see Fig. 2.14). It has 6 vertical paddles of 20 cm width, 120 cm length and 1.5 cm thickness and 3 horizontal paddles of 10.4 cm width, 140 cm length and 0.5 cm thickness,
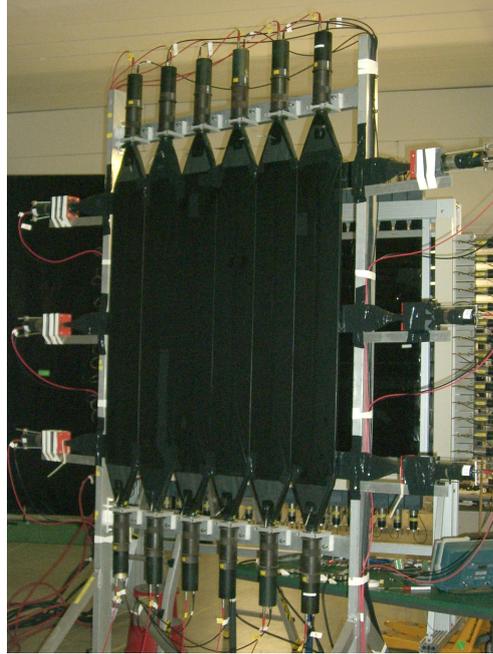
Figure 2.14: DTF detector front view.

which are separated around 44 cm. All the paddles are read-out by two photomultipliers, one at each end. The detection principles are the same as for the other detectors based on scintillator paddles.

2.7 Neutron branch detector (LAND)

The Large Area Neutron Detector (LAND) is used for the detection of neutrons produced in reactions at the target. It was designed to measure neutrons with energies from 100-1000 MeV [44]. The detector measures the ToF, the position and the energy loss of the neutrons, allowing the determination of the velocity and the position (in X,Y,Z) of the neutrons. The detector is placed at 0° and approximately 13 m behind the target. It consists of 10 planes, with 20 scintillator paddles each. In total it has 200 paddles. Each paddle covers an area of 200 x 10 cm and 10 cm depth and is formed by 11 iron sheets and 10 scintillator sheets. Two of the iron sheets are covering the outer parts of the detector and have a thickness of 2.5 mm, the inner ones are 5 mm thick. The 10 scintillator sheets are 5 mm thick. The paddles of each layer and the next are perpendicular to each other in order to measure the horizontal and vertical positions of the hits (see Fig. 2.15). When a neutron impinges in LAND interacts with the iron producing charged particles
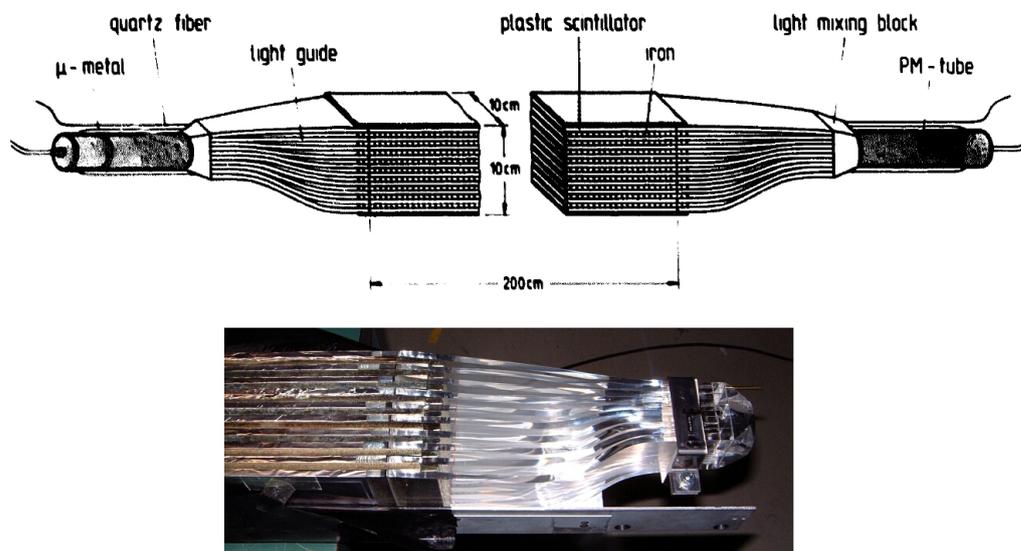
Figure 2.15: Top: Schematic view of the layer structure of a LAND paddle. Bottom: Picture of a LAND real paddle.

(mainly protons) which induce light in the plastic scintillators. Each LAND paddle is read-out by two photomultipliers, one at each end. Using some specific algorithms it is possible to reconstruct the hits in the paddles, and from them to obtain their time, energy and position.

Chapter 3

Detector calibrations

This chapter describes the procedures followed to calibrate the detectors used in the experiment, as well as some details needed for the study of specific reaction channels. The text will focus on the detector calibrations where the author of this thesis was more involved.

The first parts are focused on the incoming beam detectors which provide a good identification in mass-over-charge (A/Z) of the incident cocktail beam. Later on, we examine the detectors in the heavy fragment branch (GFIs, TFW) and finally the γ energy branch of the Crystal Ball detector and the SSD calibration.

The text will also describe very briefly some calibrations performed by other collaborators, e.g. the calibration of the high energy branch and time of the Crystal Ball detector.

3.1 Calibration levels

The data of all the detector channels used in the experiment are collected by the Data Adquisition Sysstem, and the event portions were collected together in an event builder and written into LMD-format files (List Mode Files) [45]. The information contained in the lmd files is extracted using the software package **land02**, originally written by H. Johansson [46]. This program converts the LMD files into rootfiles (via a process called unpacking) and also contains some calibration routines. The calibration procedure is performed in different steps unpacking the data into the following levels [46, 45]:

- RAW: conversion from the binary format to an analysis friendly format. The information is ordered by detector, module and channel. The

values of the different signals coming from the detectors are given in TDC, QDC or ADC channels.

- TCAL: TDC channels are converted to time units and the QDC pedestal is subtracted. The parameters applied to the RAW level data are calculated by routines included in land02, *tcal* and *clock*.

- SYNC: the detectors are not usually composed by one piece. In the case of the time-of-flight walls (LAND, TFW), these are formed by several paddles. In the previous levels, each paddle was treated individually. To combine the information from all the paddles and handle the detectors as a unit, the channels are synchronized with respect to each other. The calibration routine for this step is detector dependent. A routine called *phase1* calculates the parameters for the synchronization.

- DHIT: contains energy loss, position and time values in detector specific coordinates describing the interaction of the particle in the material (what is usually know as a hit).

- HIT: contains data in laboratory coordinates describing hits. The positions are given in cm, the times are given in ns and the energy in MeV.

- TRACK: the mass and the atomic number together with the velocity of the ions is calculated.

Sometimes the detector information suffers variations along the time. Taken this into account, a time validity function (LT_RANGE) allows to specify different calibration parameters for different ranges of the data set.

3.2   Triggers

A trigger is a system that uses simple criteria to select the signals from the detectors, when it is only possible to store a maximum set of events. In order to identify the reaction channels of interest, the signals from different detectors are combined to create triggers. In Table. 3.1 the triggers for the S393 experiment are listed. In the first column the trigger bit running from 1 to 16 is listed. Triggers 1 - 8 are the on-spill triggers, used for the analysis of the reaction channels and 9 - 15 the off-spill triggers used for calibration purposes. The second column indicates the trigger pattern (Tpat) which tells us which bits are set to 1. In the third column there is a short description about the physical meaning of each trigger. The final columns, with ones or

Trigger bit n	Tpat (2^{n-1})	Description	used by trloctrl tracer	Late trigger-kill	Early pile-up	Spill on	CB L+R	NTF1	pix	S81	CB sum delayed	CB sum	CB OR delayed1	CB OR1	proton wall delayed1	proton wall	fragment wall delayed	fragment wall	land cosm	land mult	POS1	POS.!ROLU
1	1	**Minimum bias**																				
		(Good beam (GB))				1																1
2	2	**Fragment**																				
		(GB + fragment at TFW)				1												1				1
3	4	**FRS S8**																				
		(plastic scintillator hit)				1				1												1
4	8	**CB SUM**	1	1																		
		(Crystal Ball energy threshold)				1						1						1				1
5	16	**Proton**			1																	
		(hit in the DTF)				1										1		1				1
6	32	**GB-pileup**			1																	
		(identification of pile-up)				1																1
7	64	**Pix**																				
		(hit in the pixel detector)				1			1													1
8	128	**Neutron**			1																	
		(hit in LAND)				1												1		1		1
9	256	**CB muon**				1																1
		(offspill trigger)										1										
10	512	**Land Cosm**				1																1
		(offspill trigger)																	1			
11	1024	**TFW Cosm**				1																1
		(offspill trigger)															1					
12	2048	**CB gamma**				1																1
		(offspill trigger)											1									
13	4096	**DTF Cosm**				1																1
		(offspill trigger)													1							
14	8192	**NTF Cosm**				1																1
		(offspill trigger)						1														
15	16384	**CB L+R-muon**				1																1
		(offspill trigger)					1															

Table 3.1: Trigger matrix used in the experiment. The first column indicates the trigger bit for a certain trigger. The second indicates the trigger pattern (2^{n-1}). The third column is a brief description of the trigger and the other columns are the coincidences or anticoincidences between certain detector signals.

blanks, indicate the active inputs. The first row per trigger bit represents an anticoincidence and the second one a coincidence. For example requesting the "Minimum bias" trigger, has nothing in the first row (no anticoincidence is requested). While the other row means POS and not ROLU, a signal in POS is required and nothing in ROLU is also required, i.e. an anticoincidence.

There are some triggers which fire very often during the experiment, but only a fraction of the events associated to them is saved. The ratio between the real number of events triggered and the ones stored is called downscale factor.

One of the frequent triggers for experimental running trigger is the 2, called "Fragment", meaning that there is an event with "Minimum bias" that also hits the last detector in the heavy fragment branch, the TFW. Another very common trigger is the number 4 "CB SUM" which indicates deposited energy above a certain threshold in the Crystal Ball detector, indicating a high energy event. The last on-spill trigger used is the neutron detection trigger with number 8 and called "Neutron" that selects a possible neutron hit in the LAND detector.

3.3   Pedestal subtraction

The QDC reads-out a small quantity of charge called pedestal, even when no input signal is present. Since the pedestal is always there, it has to be subtracted from the data in order to avoid the usage of signals compatible with noise. The pedestal calculation is done by the land02 routine *clock* and is subtracted on the TCAL calibration level.

3.4   Time calibration

The TDC modules have a nominal gain value, which can fluctuate throughout the experiment (e.g. temperature). In order to correct this effect and to achieve a good time resolution, a time calibrator module was used during the whole experiment to monitor the TDC gain. This module generates two pulses with known delay. One is sent to all electronic channels and the other to the DAQ as a trigger allowing the monitoring of the TDC gain for the entire experiment (explanation about the working principles in Ref. [47]). After this calibration, the time is represented in ns, but the time difference between detectors is not representing the actual time of flight between them, a synchronization between them is needed.

3.5   Incoming charge calibration

The charge identification of the incoming ions is performed with the PSP detector. It is obtained directly from the energy loss measured by the detector's cathode.

Using the Bethe-Bloch formula it is possible to relate the energy loss of the ions to the charge (equation 2.2). To obtain the calibration parameters, a run with A/Z=2 was used. ^{8}Be has a half life very short making its observation impossible. So, it does not appear in the identification matrix. This helps with the identification of the other nuclei (see Fig. 3.1).
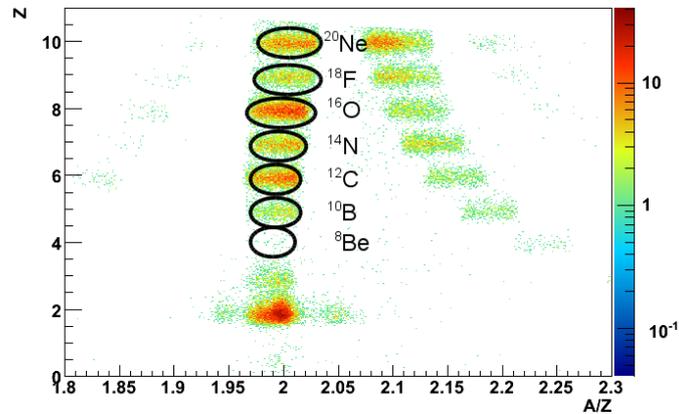
Figure 3.1: Identification plot for a run with A/Z=2. The ^{8}Be does not appear in the matrix making easier the identification of the other nuclei. The Tpat two (minimum bias + fragment at TFW) was selected in this plot.

For the selected nuclei, the signal in the PSP cathode is shown in figure 3.2. The charge assigments are possible because of the missing ^{8}Be. The peaks have the approximate shape of a Gaussian function. Every peak is fitted to a Gaussian function and the mean value is used for the charge calibration. The results of a linear fit of the representation of the mean value vs. the calculated energy loss for each species in the PSP, provides the slope and offset that relates the energy-loss measurement in the cathode with a certain charge (see figure 3.3).

3.6   Incoming velocity calibration

In order to identify the incoming ions in mass and charge, we need to know their velocities. With this purpose S8 and POS detectors are used to determine the *ToF* and the path of the ions. The velocity calibration is
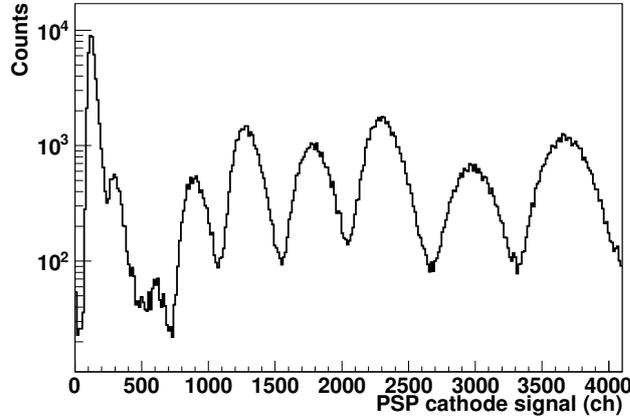
Figure 3.2: PSP energy loss measured in the cathode which is correlated to the charge. The mean value of a Gaussian function fit over the peaks relates the energy loss with a certain charge.
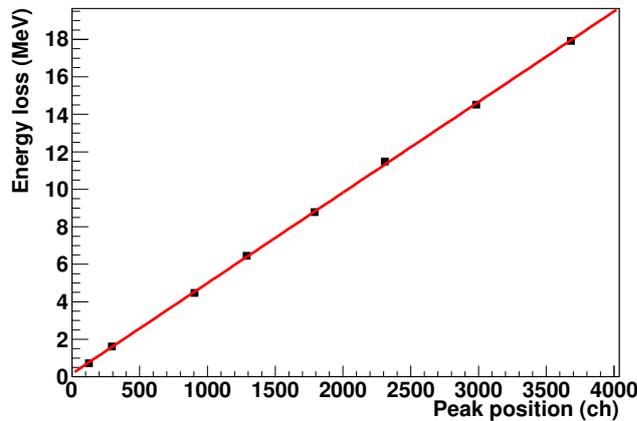
Figure 3.3: Energy loss in the PSP calculated by Bethe-Bloch equation vs. the mean value of the Gaussian fits to the signal in the PSP cathode.

usually performed using runs with primary beam data at different energies (see for instance reference [48]). This procedure could not be performed in this experiment because the TDC module for S2 and S8 was changed during the calibration runs. The dependence of the variables on the electronic setup do us to persist in the use of this calibration runs.

To perform this calibration, the same data set (A/Z=2) used for the velocity calibration are employed. The time signal from S8 and POS is also known. All this information can be used to calculate a time offset and a flight

path. The flight path will be included as an experiment-specific geometrical parameter and the time offset should be provided as a calibration parameter in the land02 programme.

The velocity of the ions β is related to their time-of-flight (ToF) and their flight path as follows

$$\beta = \frac{S}{ToF \cdot c} \tag{3.1}$$

where c is the speed of light, S is the flight path and β is the velocity of the ions.

The time difference δt between two detectors is

$$\delta t = ToF + T_{offset} \tag{3.2}$$

Combining equations 3.1 and 3.2 we get

$$\delta t \cdot \beta = T_{offset} \cdot \beta + \frac{S}{c} \tag{3.3}$$

A fit of this ToF for a few ions can be performed. Figure 3.4 shows the linear fit. The δt is distributed approximately according to a Gaussian distribution, being the mean value of the Gaussian the time of flight. As the magnetic rigidity Bρ (from FRS), the mass number and the charge are known, it is possible to calculate the energy and from that, the velocity of the ions.

A linear fit of $\delta t \cdot \beta$ vs. β allows to determine the flight path (from the offset) and the time offset (from the slope) (see figure 3.4).
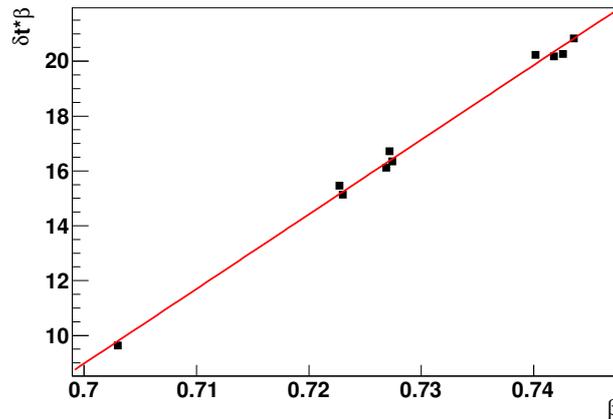
Figure 3.4: Linear fit of $\beta \cdot ToF$ versus β for ions with N = Z = 2.

3.7 Silicon Strip Detectors, SSDs

The Silicon Strip Detectors (SSDs) are used for charge identification and position measurement [49]. There were four in-beam SSDs used for tracking and charge identification of the heavy fragments, and other four surrounding the target to track and identify the quasi-free scattering nucleons. The surrounding four ultimately could not be used in this analysis because they did not work properly.

The RAW level contains one energy value for each of the 1024 strips. A pedestal calculation is performed using the *clock* program. The pedestal is characterized by a mean and a sigma value from their Gaussian function fit. A large pedestal sigma indicates a broken strip.

To find all the noisy/dead strips, the energy in TCAL level versus the strip number had to be studied. Once all the unusable strips have been identified, a negative pedestal value of -1 needs to be assigned in the *clock* output to the "dead" ones, disabling their later use [28]. TCAL contains the pedestal-subtracted energy values for all the strips present in the previous level. Up to SYNC level (included) the pedestals are subtracted, a common noise correction is performed, a gain-adjustment is done and also a zero-suppression.

When an ion passes through a SSD, the number of fired strips depends, among other things (e.g. angle of incidence), on the ion charge traversing the material. So, in order to get the energy loss of an ion, the energy of all the fired strips must be added up. The group of strips fired forms a cluster and every cluster has a center of gravity CoG (hit position) defined as:

$$CoG = \frac{\sum_{k=1}^{N} n_i q_i}{\sum_{k=1}^{N} q_i} \tag{3.4}$$

where i is the strip index and N is the number of strips in a cluster. A strip is added to a cluster if its energy is bigger than $1\sigma_{ped}$ of the pedestal. In order to have a cluster, at least one of the strips needs to have an energy above $4\sigma_{ped}$. At DHIT level, a cluster is characterized by its position (position of the hit in units of cm where the origin is at the first strip), energy (energy of the hit), area (sum of all energies of a cluster), basewidth (number of strips belonging to the cluster excluding dead strips) and η (measure for the exact location of the hit on strip level). The hit position in units of the strip number is shown in Eq. 3.5. The position in the S and K sides is caculated

by multiplying the CoG (center of gravity) by the strip pitch (104 μm for the K side and 110 μm for the S side),

$$position = CoG * pitch \tag{3.5}$$

The η distribution is charge dependent, that is, an individual calibration is needed for each charge [50]. In the HIT level the origin of coordinates is moved to the center of the detector. The figure 3.5 shows a comparison for the energy loss seen in two detectors before (left) and after (right) calibration. In this figure the calibration was performed for charge 7, which is the last blob on the plot.
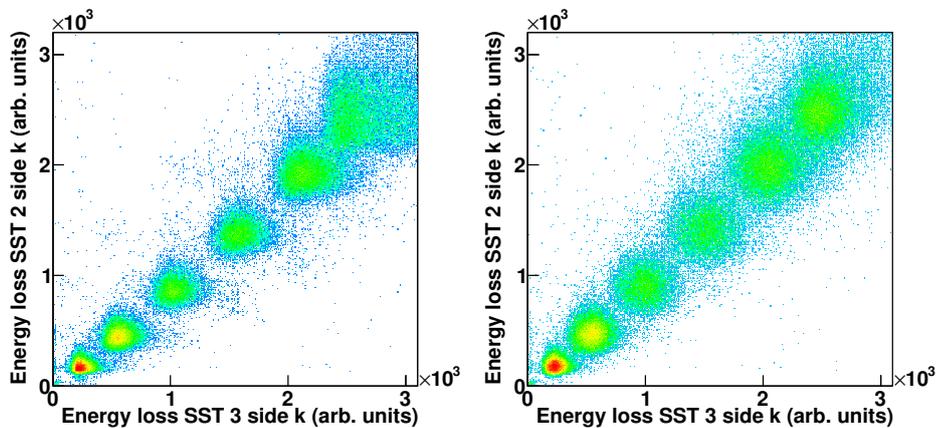
Figure 3.5: Energy loss in the second silicon vs. energy loss in the third silicon for the k-sides and for an empty target run. In the left figure the plot before the calibration parameters were applied is shown; in the right one all the calibration parameters have been applied. The *Fragment* trigger (Tpat 2) has been selected.

3.8 Crystal Ball: γ and proton readout

The Crystal Ball (XB) detector is used to measure the de-excitation γ ray energies and to measure and identify the nucleons coming from the quasi-free scattering reactions. Different procedure has been employed for the calibration of each detection mode.

3.8.1 γ energy calibration

The calibration of this branch consisted of subtracting the pedestals and converting the QDC channels into energy expressed in MeV (using the cal-

ibration parameters to go from RAW to SYNC level). In order to do that, different sources of known energies were used, allowing to correlate the channel number with the γ energy. In our experimental conditions, the γ energies are well below 10 MeV. The sources used were ^{22}Na (γ's with 511 keV and 1274.54 keV [51]) and ^{60}Co (γ's with 1173.23 keV and 1332.49 keV [51]). There were different calibration runs along the experiment, where the source was placed in the left or in the right side of the detector. Right and left side refers to standing upstream of the XB and looking downstream, towards AL-ADIN and LAND. The right side has crystals 1-81, and the left side crystals 82-162. When the XB is opened, the source is attached with tape to the centre of its respective hemispheres. The two XB halves/hemispheres are about 1 m apart from each other then, so only one half can be irradiated at a time.
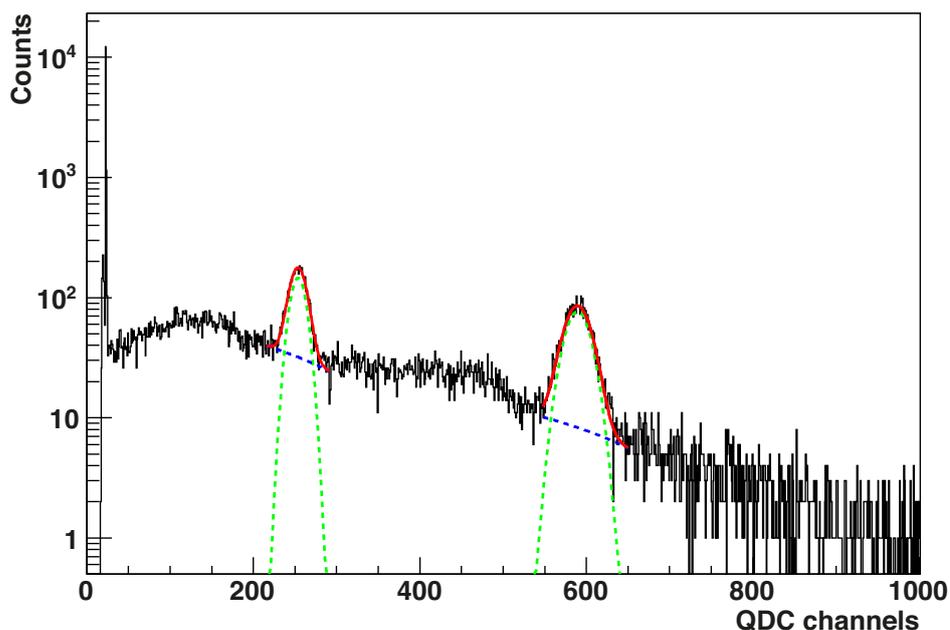
Figure 3.6: ^{22}Na energy spectrum fits for crystal 1. To perform the calibration, the photopeaks at 511 keV and 1275 keV are fitted as the superposition (red line) of a Gaussian distribution (green dashed line) and a linear function (blue dashed line).

RAW level data is fitted [52, 53, 54] with the superposition of a Gaussian function and a linear background in the vicinity of the peak. Figure 3.6 shows the performed fits for the ^{22}Na source. Then, the energy in MeV is

plotted vs. the energy in channels and fitted to a straight line. The slope of the linear fit is related to the gain of the whole electronic chain as follows:

$$E(MeV) = slope \times (E(channels) - offset) \quad\quad (3.6)$$

with the slope expressed in MeV/channel and the offset in channels.

In figure 3.7 the slope versus the crystal number is shown for the whole XB. The slopes have this distribution due to the ordering of the crystals. The gain is lower on the PMT's in the forward direction because of the Lorentz boost which affects the γ energies, increasing the energy of those travelling in a more forward direction. The crystal 1 is on the right hand side at 90 degrees from the beam direction and, then, the crystal number increases, going out from this crystal in a spiral until crystal 81. The other half has the crystal 162 in front of the crystal 1, left at 90 degrees from beam direction, and here the crystal number decreases to 82 in spirals also.
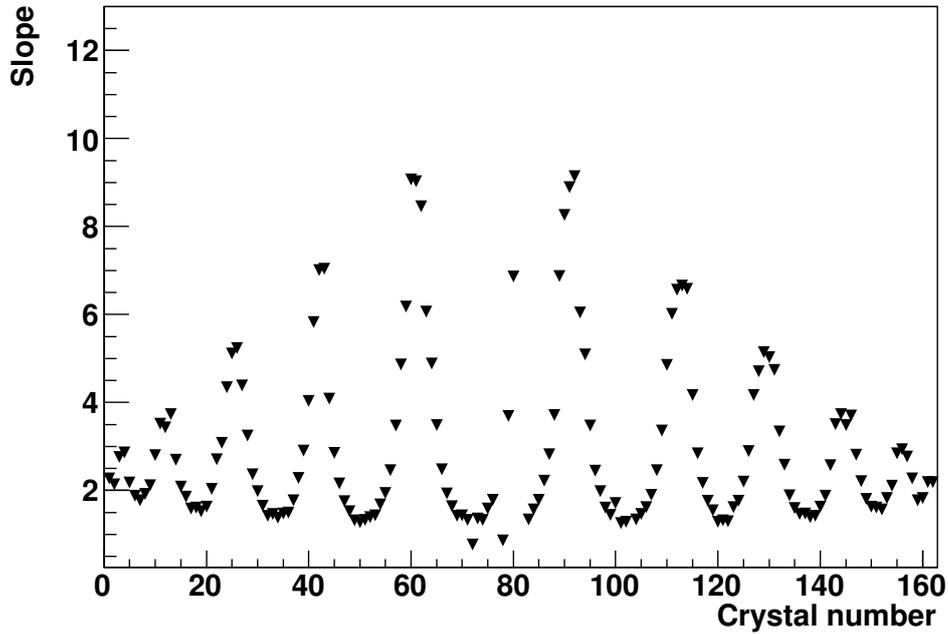
Figure 3.7: Slopes of the linear fit performed to the plot energy (MeV) vs. energy (channels) for the runs 336 (source in the right hemisphere) and 337 (source in the left hemisphere).

It has been observed along the experiment that the slopes and offsets are not constant. They vary depending on run number and crystal number,

meaning than the same calibration parameters can not be used over the entire experiment.

When a γ impinges in a scintillator crystal, usually the energy is not deposited in only one crystal. It is distributed over a certain area around the first interaction point. In order to reconstruct the total γ energy, the depositions in the neighbourhood are added to the main crystal energy. These set of crystals form a *cluster* (this will be explained in more detail in the next chapters). To get an accurate *cluster* energy, it is very important that every crystal has a good energy calibration throughout the whole experiment, i.e. the crystals must be aligned in energy.

In order to correct the drifts (variations of the peaks positions for the same crystal with the time) and to have a good energy alignment (variations in the peak positions for different crystals during the same run), the natural background (in combination with the available sources) has been used to monitor the energy peaks along the experiment. In figure 3.8 the background energy spectra for the crystals 1 and 9 is shown. The ^{40}K peak at 1.46 MeV it is clearly observed, but it is shifted, showing the misalignment between the different crystals in the same run.
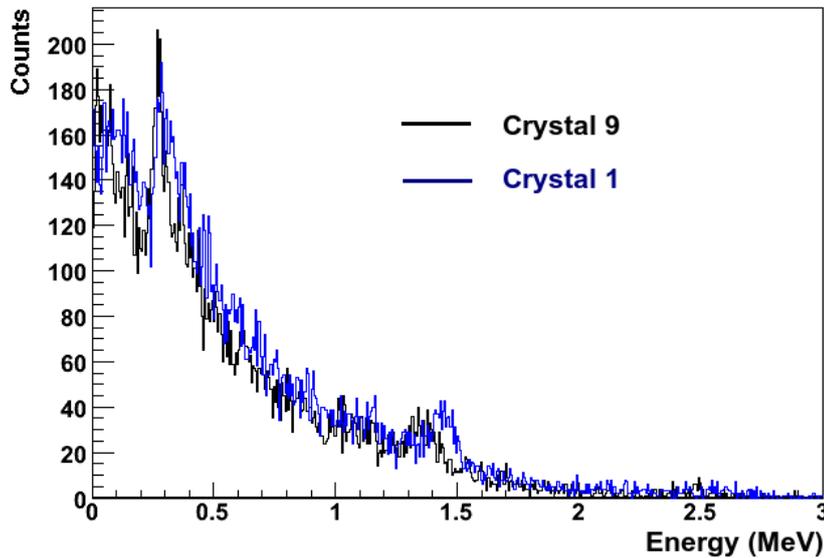
Figure 3.8: Example of the observed shift in the crystals 1 and 9 for the background peak of the ^{40}K.

In Fig. 3.9 the improvement of the peak resolution is clearly visible comparing the same run before and after correcting the drifts gain of the

crystals.
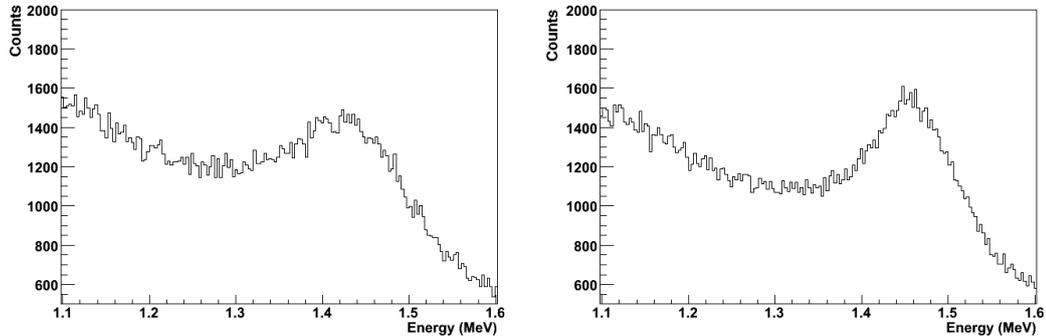
Figure 3.9: Comparison between the energy deposited in all the crystals for the same run: before the crystals alignment (left) and after the crystal alignment (right). The ^{40}K peak at 1460 keV is observed.

3.8.2   High energy branch calibration

The ideal way to calibrate the proton branch is with proton beams at different energies in the range where the quasi-free protons are expected (10 - 300 MeV) and also covering the expected angular range. Unfortunately for this experiment there were not available beams to calibrate the high energy branch. Instead, the proton branch was calibrated using cosmic muons. For that purpose the program *gamma2*, inside the land02 package, and a simulation (Geant3) were used. There are two procedures used by the collaboration to perform the calibration and can be outlined as follows:

- the muon energy is plotted for both branches (high-energy branch vs. low-energy branch). The resultant curve can be fitted to a straight line obtaining an offset and slope. This slope multiplied by the γ energy gain calculated in the previous section, corresponds to the proton gain.

- only muons that traverse the XB centrally are used (two opposite crystals are hit). The energy loss of the muons is displayed versus the crystal number. The energy loss for each crystal has a Gaussian shape. The mean value corresponds to the mean energy loss of a muon traversing the crystal and can be calculated from a simulation. From the comparison of the simulated value with the experimental, the gain factors are obtained.

More detailed information can be found in previous works [30, 55].

3.8.3   Time calibration and synchronization

The time signals from the Crystal Ball detector are used to clean-up the events from background contributions. The measured energies are requested to be inside a certain time window. The conversion from channels to time in ns is done in the same way as it was explained before for the POS detector, using the time calibrator. To synchronize the times the *gamma2* program was used. The algorithm uses a run where a source emitts two γ's in coincidence. The two expected γ's could deposit their full energies in two different crystals. If this condition is fullfilled, the time difference between those γ's is saved in a histogram. As the γ's are in coincidence, the peak mean value should be centered in zero. For each combination of two crystals it is possibe to define a histogram, which can be fitted to a Gaussian function. The final equation system can be solved to determine the time offsets.

3.9   GFIs

The GFIs detectors provide horizontal position measurements of the heavy fragments after the dipole. When an ion hits the GFIs produces light which is guided through the fibres creating a well-defined light spot on the photocathode of the PSPM. Depending on the position of the light spot in the photocathode, an electrical signal is generated in some anode wires. From the combination of these signals, the position of the light spot is reconstructed, making possible the identification of the hit fibre. To extract the X position, the internal coordinates of the detector (u,v) need to be transformed.

The first step of the GFIs calibration is the pedestal subtraction, that is performed as for other detectors using the *clock* routine. From RAW level data to TCAL data, the pedestals are subtracted.

The amplitude of the signals is not the same for all the wires. It depends on its position on the photocathode and on its amplification. So, a proper gainmatch of all the anode wires on the photocathode is needed before reconstruct the hit position. It has been observed that the charge distribution of a hit produces energy in about seven neighbouring wires in each (u,v) direction, and their amplitudes are expected in a Gaussian distribution. This fact is used to perform the gain matching of the wires, taking all the signals from neighbouring wires (cluster) into the distribution. The calibration is done in a run called "sweep run" using the *phase1_gfi* routine. The calibration parameters are then applied in the DHIT level. In this run the whole detector is illuminated by varying the magnetic field of the dipole. In figure 3.10 an example of the charge distribution before (top) and after the gain

matching (bottom) is shown. After gain matching the clusters, their positions become more regular and well defined. The divided clusters also merge and the extension of the clusters is reduced. Also the distortion observed at the edges decreases. The dots in between the clusters are ions that hit in the non scintillating part of the fibre, depositing low energy.

In order to finalize the calibration, the positions of the clusters must be determined. This is done by projecting all the hits onto a two dimensional histogram (u,v). For each cluster the mean positions ($\bar{u}$,$\bar{v}$) and the standard deviations (σ_u,σ_v) are obtained by fitting the clusters to Gaussians. The cluster neighbours are determined by using the lengths and angles of the vectors connecting them. In figure 3.11 positions of all the clusters and the vectors that connect neighbours for one of the fibres are shown.

An index pair (k,l) can be assigned to each cluster, where k and l are the indices for the columns and rows of the matrix k x l. Every (k,l) has a corresponding internal mean position ($\bar{u}$,$\bar{v}$) on the PSPM, which is also associated to the horizontal position in the detector (x).

To convert the internal coordinates (u,v) to the corresponding x positions a transformation has to be applied. If the position of a hit is inside a cluster (within its width), the fibre assignment is straightforward. Instead, if the hit is between two clusters, there is more than one candidate fibre to assign the hit. In this case, a weighted average of the candidate fibres is used [56].

The reconstructed position is given in cm in the HIT level. The horizontal position for two different fibre detectors, which are approximately 150 cm apart, is shown in Fig. 3.11 for the "sweep run" used for the calibration. The good correlation shown between the position measured by the two detectors proves the good position resolution after calibration.
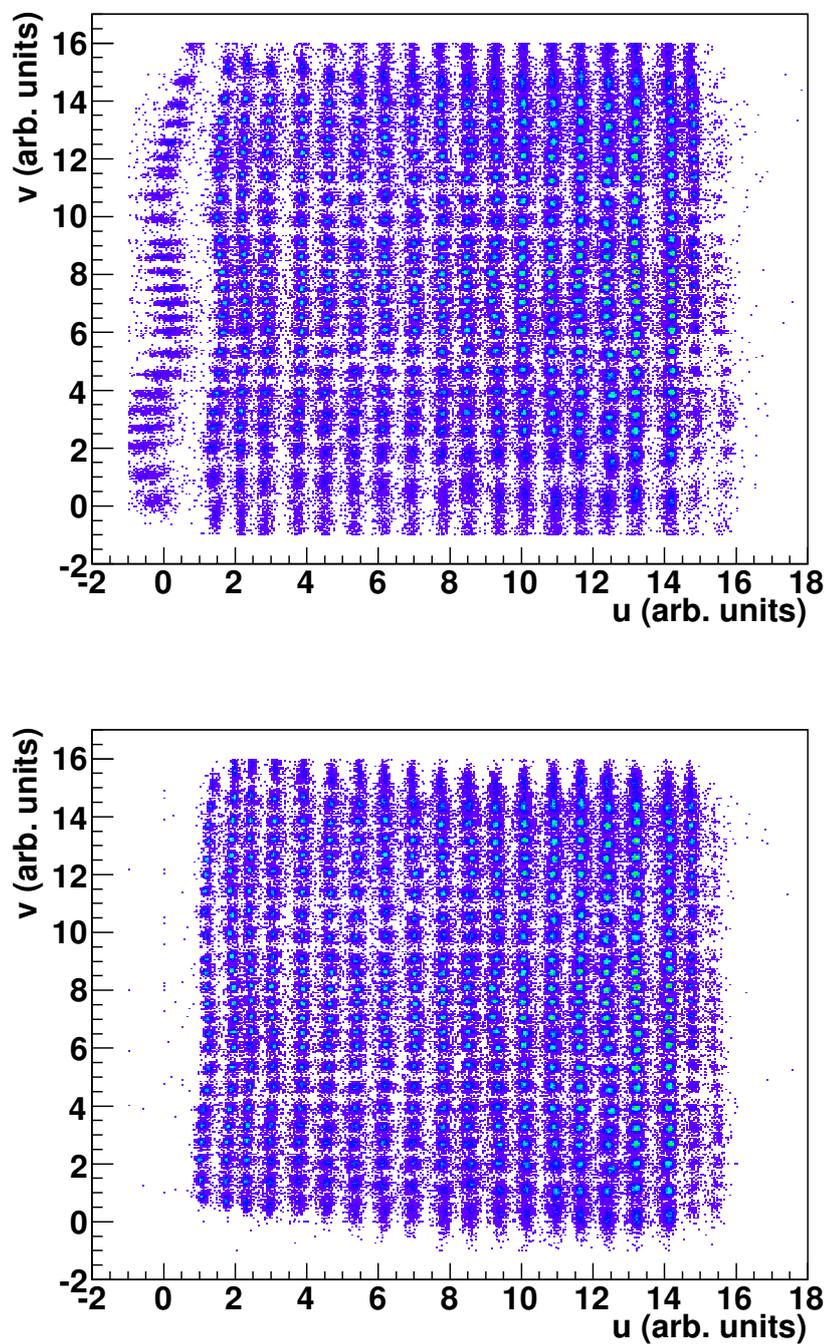
Figure 3.10: Reconstructed image of the fibre mask before (top) and after (bottom) gain matching. The clusters have a better-defined shape and the large distortion observed at the edges of the photocathode (upper plot) is improved after the gainmatching procedure (bottom plot).
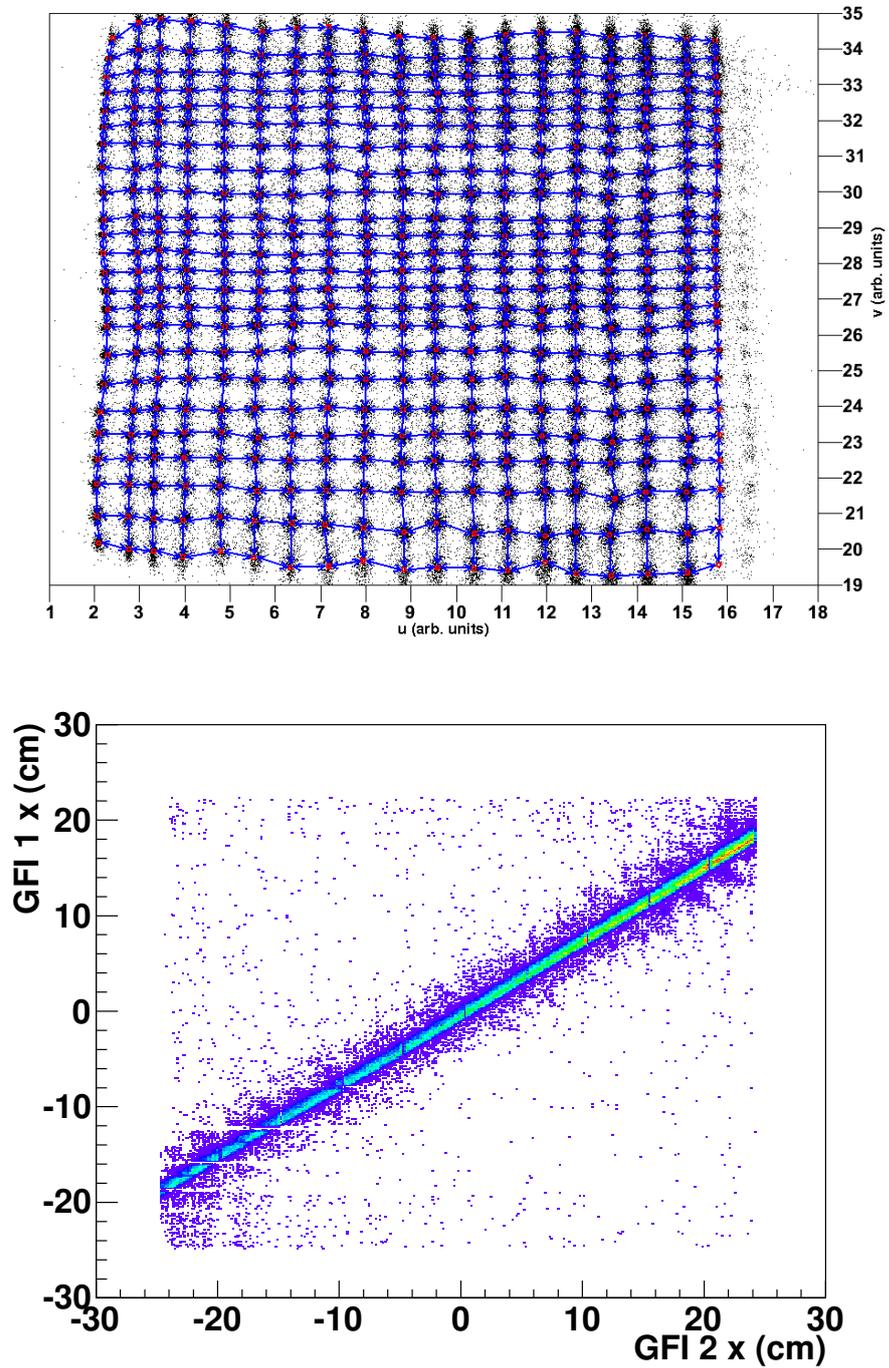
Figure 3.11: Top: Mean position of the clusters. Neighbours are indicated by arrows. Bottom: Correlation between the reconstructed position between two fibre detectors 150 cm apart.

3.10   Time of Flight Wall (TFW)
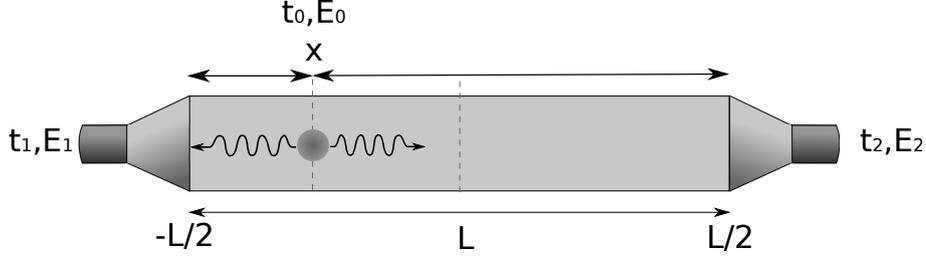
Figure 3.12: Position of a hit in a scintillator paddle (x). The time (t_1, t_2) and energy (E_1, E_2) signals measured by each PMT are used to calculate the position of the hit (x), its energy (E_0) and its time (t_0).

The TFW is a detector made of plastic scintillator paddles. Each paddle is read-out by two photomultipliers, one at each end, which provide time and energy signals (see Fig. 3.12). The position information [47] can be obtained by time differences or energy ratios between the measured times and energies, repectively.

- Calculation of position and time of a hit using the time signals:

  The measured times are:

$$t_1 = t_0 + \frac{x + L/2}{v_{scint}} \tag{3.7}$$

$$t_2 = t_0 + \frac{L/2 - x}{v_{scint}} \tag{3.8}$$

where t_1 and t_2 are the times measured by the two photomultipliers, t_0 is the interaction time, v_{scint} is the effective light velocity in the scintillator, L is the paddle length and x is the position of the hit in the paddle. The position of a hit in a paddle is calculated as a time difference between the two photomultipliers times.

$$t_1 - t_2 = t_0 + \frac{x + L/2}{v_{scint}} - t_0 - \frac{L/2 - x}{v_{scint}} \tag{3.9}$$

$$x = \frac{v_{scint}\,(t_1 - t_2)}{2} \tag{3.10}$$

The interaction time is calculated by adding up both photomultiplier times.

$$t_1 + t_2 = t_0 + \frac{x + L/2}{v_{scint}} + t_0 + \frac{L/2 - x}{v_{scint}} \tag{3.11}$$

$$t_0 = \frac{t_1 + t_2}{2} - \frac{L}{2v_{scint}} \tag{3.12}$$

- Calculation of energy and position of a hit by using the energies provided by the photomultipliers:

  The distance from the hit position to the photomultipliers is bigger than the paddle width. So, the measured energies can be approximated as it follows:

$$E_1 = E_0 \cdot exp\left[-\frac{(x + L/2)}{\lambda}\right] \tag{3.13}$$

$$E_2 = E_0 \cdot exp\left[-\frac{(L/2 - x)}{\lambda}\right] \tag{3.14}$$

$$\tag{3.15}$$

being λ the attenuation length in a paddle. The interaction energy is calculated by multiplying both photomultiplier energies,

$$E_1 \cdot E_2 = E_0^2 \cdot exp\left[-\frac{L}{\lambda}\right] \tag{3.16}$$

$$E_0 = \sqrt{E_1 \cdot E_2} \cdot exp\left[\frac{L}{2\lambda}\right] \tag{3.17}$$

The interaction position is the ratio between the photomultipliers energies,

$$\frac{E_1}{E_2} = exp\left[-\frac{(x + L/2)}{\lambda}\right] \cdot exp\left[-\frac{(L/2 - x)}{\lambda}\right] \tag{3.18}$$

$$x = -\frac{\lambda}{2}ln\frac{E_1}{E_2} \tag{3.19}$$

In all these equations the cable lengths, signal losses and proccesing times were not taking into account, but they are included in the calibration procedure.

In the first *land02* level (RAW), an energy and a time for each paddle and for each PMT is available. In the TCAL level the same variables are present but the pedestal is subtracted and the time is converted in ns. The

calibration parameters are calculated with the routines *clock* and *tcal*. In the SYNC level, the data structure is the same as in TCAL level (energy from paddles with two PMT tubes), but the four parameters calculated using *phase1* are applied. The first one provides the gain needed to synchronize the paddles to each other; the second one performs gain-matching over the two energy signals; the third one is the relative offset in time between a pair of horizontal and vertical paddles which synchronizes the mean time calculated by the two paddles; the last one makes the differences between the times provided from Y paddles and X paddles to be zero. In the DHIT level the information about the photomultipliers is lost; all the observables are described in the internal coordinates of the detector. The final level is the HIT: at this stage of the calibration the information about the whole detector is in cm and the energy in arbitrary units.

The last step, is the detector synchronization between runs [57]. When a channel is studied, several runs are joined and a synchronization between their energies and times is needed. For this purpose the energy loss vs. event number will be studied by fitting to Gaussian distributions different groups of events. The ATIMA code [58] was used to calculate the energy loss in the TFW after the beam went through all the previous detectors, and also the time of flight between the target and the TFW. These values were used to match the mean value from the previous fits. In the top plot of figure 3.13 the energy loss vs. the event number is presented, showing that the energy is not well synchronized between event groups. In the bottom plot of the same figure, the result after applying the corresponding corrections to synchronize the runs is shown. At the end of the calibration procedure, the energy is in MeV and the *ToF* in ns.
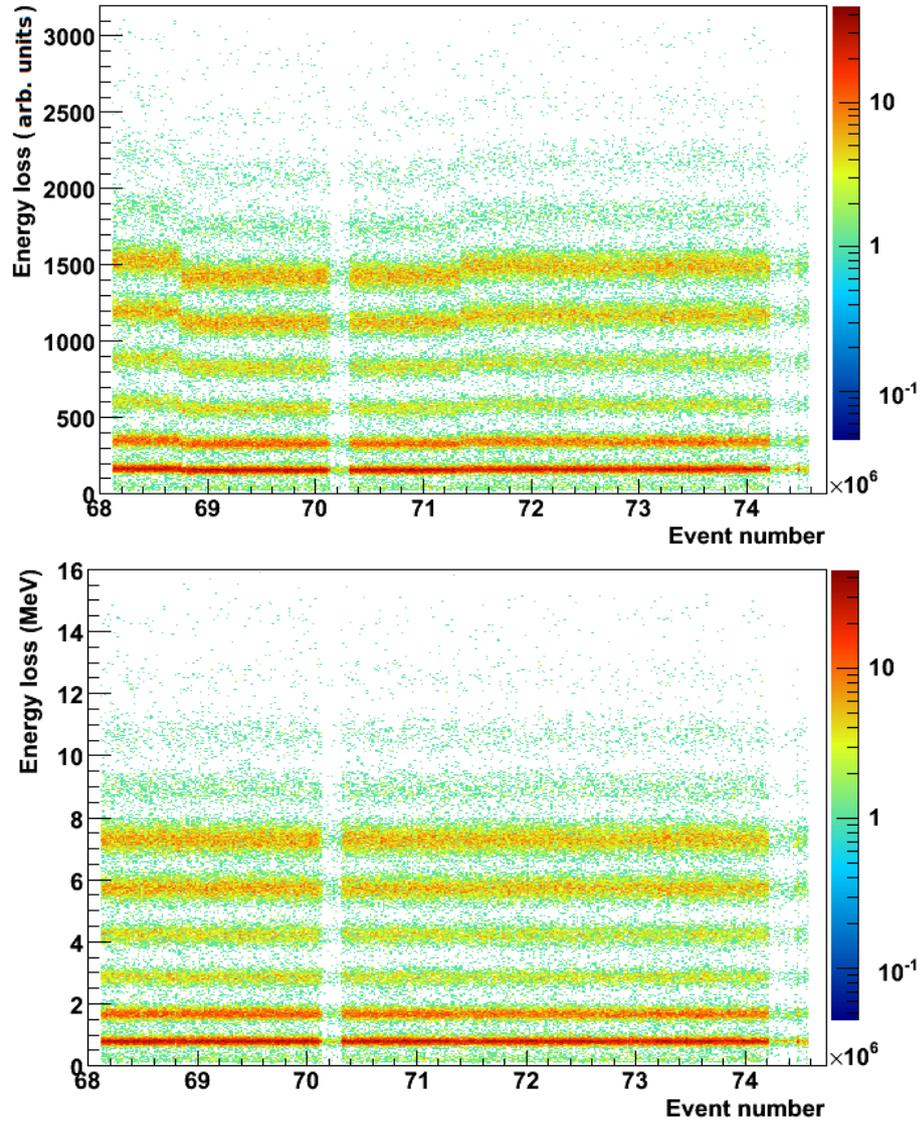
Figure 3.13: Top: Energy loss in the TFW before synchronization. Bottom: Energy loss in the TFW after synchronization and energy calibration using ATIMA [58]. In both plots the "Fragment" trigger was selected.

Chapter 4

Analysis procedures

In this chapter the procedures that have been used to identify the reaction channels and to calculate the physical quantities of interest will be described.

First, the incoming projectile needs to be unambiguously identified. Then, the products of the reaction are identified helped by their deflection in AL-ADIN using the two SSDs after the target, the two GFIs and the TFW. Once the incoming and the outgoing species are identified, the text will focus on the calculation of two physical observables: cross sections and momentum distributions. The calculation of the angular distributions of the two emerging nucleons from the quasi-free scattering reactions will be described as well. The last part of the chapter will focus on the de-excitation γ rays measured with the Crystal Ball detector.

The analysis procedures herein described will be followed for all the different studied channels. In order to avoid repetitions, all the figures and exemplifications will be shown for one incoming projectile, the ^{21}N.

4.1 Identification of the outgoing fragments

The reaction channels were selected via unambiguous identification of the nuclei of interest both before and after the target. The pre-target nuclei identification, as explained in Chapter 3, was achieved via separating charge and mass values of the nuclei derived from energy loss and ToF measurements. This enabled the tagging of each incoming nucleus to observe the corresponding reaction fragments post-target. The selection of the incoming was performed via a two dimensional elliptical cut. The contamination from neighbouring isotopes in Z and A/Q was evaluated to be negligible, so the incoming beam can be considered as free of contamination. Figure 4.1 shows an identification plot, representing Z vs. A/Z for setting 6, centred on ^{24}O.
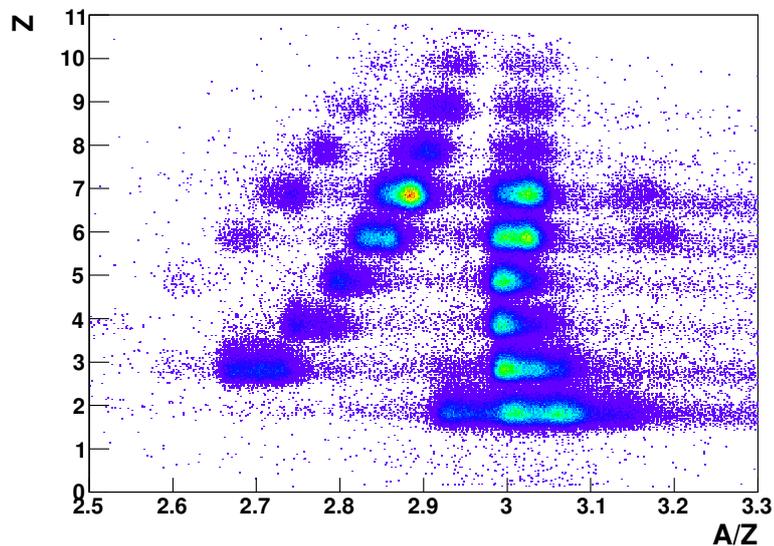
Figure 4.1: Incoming identification plot for the setting 6 centered in ^{24}O. Nuclei from Z=2 to Z=10 were produced in the experiment.
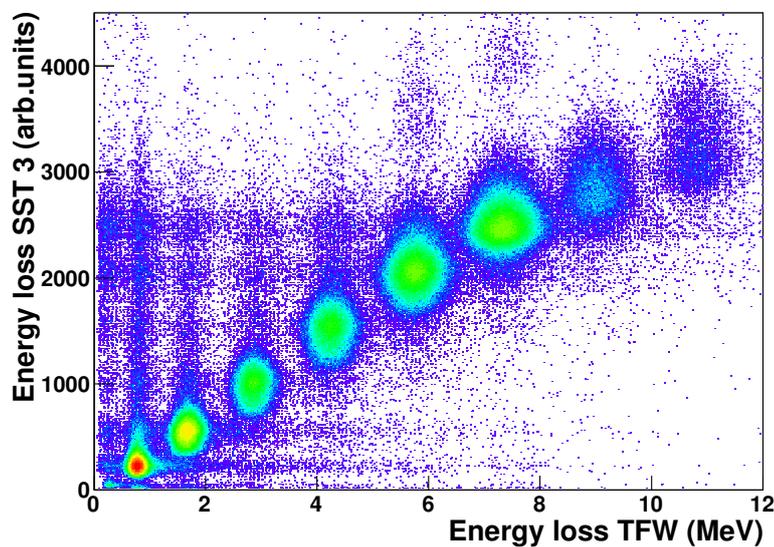
Figure 4.2: Energy loss in the first SSD after the target vs. energy loss in the TFW. Charges from 2 to 9 are shown from left to right. The calibration of this plot was performed for charge Z = 6.

Once the incoming cocktail beam is completely identified, the outgoing fragments after the reaction target must be also identified. For the outgoing charge, the first SSD after the target and the TFW are used. Figure 4.2 shows the distribution of the charge measured in the third SSD (first after the target) vs. the charge in the TFW. The charges go from 2 (first blob in the left) to 9 (last blob in the right). This information is given to the tracker to make possible the charge identification. As previously explained in Chapter 3, the calibration of the SSDs is charge dependent. In figure 4.2, it was performed for charge Z = 6.

The mass of the outgoing particles is determined using a tracking program[1]. This program reconstructs the trajectories through the magnetic field for the outgoing fragments and protons (not used in this work) using as an input the laboratory positions of the detectors, the charge of the fragment being tracked and the ALADIN current determining the magnetic field that was applied to the tracked events. The detectors involved in the trajectory determination for the fragments are the two SSDs after the target, the two GFIs, and the TFW.

The mass-over-charge ratio is determined using the equation 4.1

$$B\rho = \frac{A}{Z}\frac{m_0 c}{e}\beta\gamma \tag{4.1}$$

Depending on its $\frac{A}{Z}$, β and B, the particles will follow a different trajectory through the magnet. The dipole field $\vec{B}(\vec{r}, I)$ had been measured and parametrized into a map, making possible the determination of $B\rho$ for a given trajectory and current. The β is given by the flight path of the particle and its time-of-flight between the target and the TFW. The track after the magnet is determined by the two GFIs and the TFW; the main contribution comes from the GFIs because of its good position resolution. The tracking program is calibrated by varying the positions of the detectors for a suitable track sample until the reconstructed track minimize the distance between the positions of the fragments in the detectors given by the tracker and the real positions measured by the detectors. The tracking can run using three different modes: forward, backward and mixed. In the first one the tracks go exactly through the SSDs measured positions. The laboratory positions of the detectors after the magnet are slightly varied until finding the best calibration. The second mode fixes the track through the positions measured by the detectors downstream from the magnet (GFIs, TFW), then the SSDs laboratory coordinates are varied until the best minimization is determined. The third mode is a combination of the other two. In this work the forward

---

[1]developed by Ralf Plag for the R3B collaboration [59]
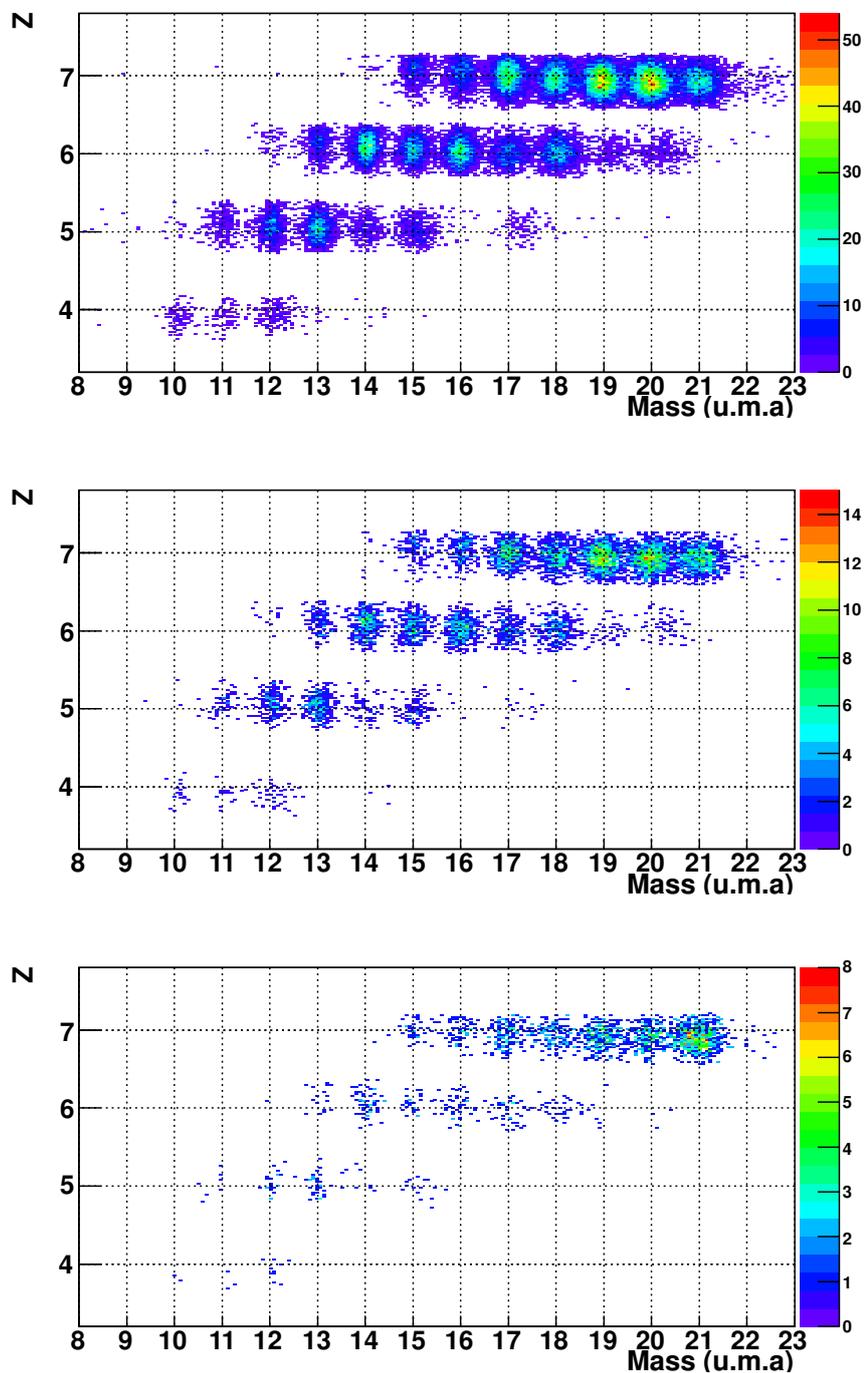
Figure 4.3: Atomic number versus isotope mass of the outgoing fragments in coincidence with the Crystal Ball trigger for the three different targets. From top to bottom: plastic, carbon and empty target. The tracker needs a two dimensional cut on the SSDs and TFW charge in order to identify the charges. For this reason there is no background events between charges in the plots.

mode was chosen because the four silicons in the beam line were aligned for angular measurements of the fragments (see Section 4.5). The tracker starts with a track candidate before the magnet which is given by the positions of the particles in the SSDs. An assumed mass and β are used to calculate the track throughout and after the magnet. Then, the mass is varied until the trajectory matches the GFI measured hit positions and the β is corrected according to the difference in *ToF*.

Figure 4.3 shows the identification plot in reconstructed mass and charge of the reaction products in coincidence with the Crystal Ball trigger for the projectile ^{21}N, obtained after running the tracking program for the three available targets. The charge was obtained using the Bethe-Bloch formula from the energy loss of the particles in the TFW, and is only used for the events selection. For physical calculations as, for example, the momentum, the nominal values for A and Z are always used.

The runs corresponding to different targets were not measured the same amount of time. Every mass distribution for each target needs to be normalized by the number of incoming projectiles (right plot in figure 4.4). The left plot of the figure 4.4 shows a comparison between the outgoing fragments masses produced for all the targets. Figure 4.5 shows the same information with a gate in the outgoing charge 7 (nitrogen).
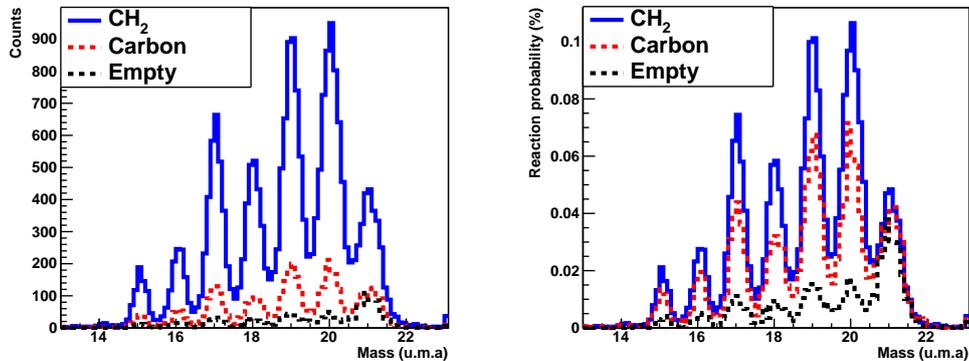
Figure 4.4: Mass spectrum (left) and normalized mass spectrum (right) for the outgoing fragments measured in coincidence with the Crystal Ball trigger for the three different targets.

The mass resolution is defined as the ability to distinguish between two different masses in the mass spectrum. It is calculated as the percentage of the full width at half maximum (FWHM), divided by the mean position of the peak. A study of the mass resolution was performed fitting the whole distribution with a multi-Gaussian (table 4.1). In figure 4.6 the Gaussian
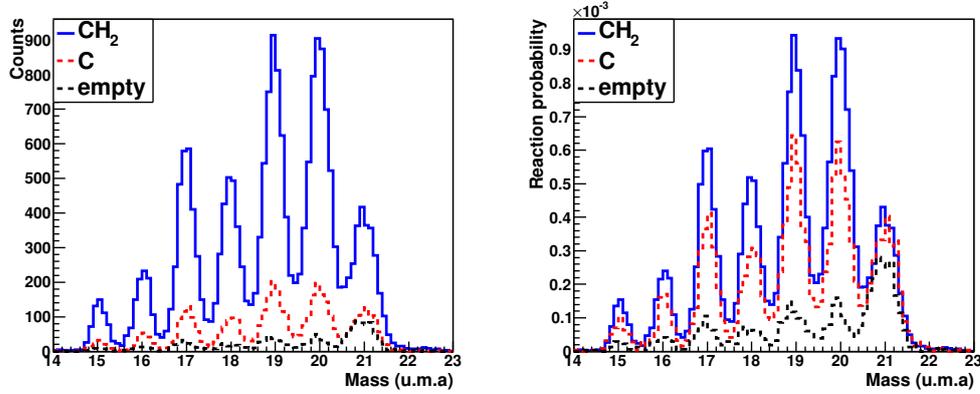
Figure 4.5: Left: Mass spectrum of all the outgoing fragments measured in coincidence with the Crystal Ball trigger for the three different targets and for the charge 7. Same as before, normalized.

fits performed to obtain the mass resolution are shown. In the left plot are shown the fits for the nitrogen isotopes. Their resolution varies between 3.27 % and 2.59 % for the highest and lowest masses respectively. In the right plot are shown the carbon isotopes; in this case the resolution varies between 3.33 % and 2.57 % for the highest and lowest masses respectively.
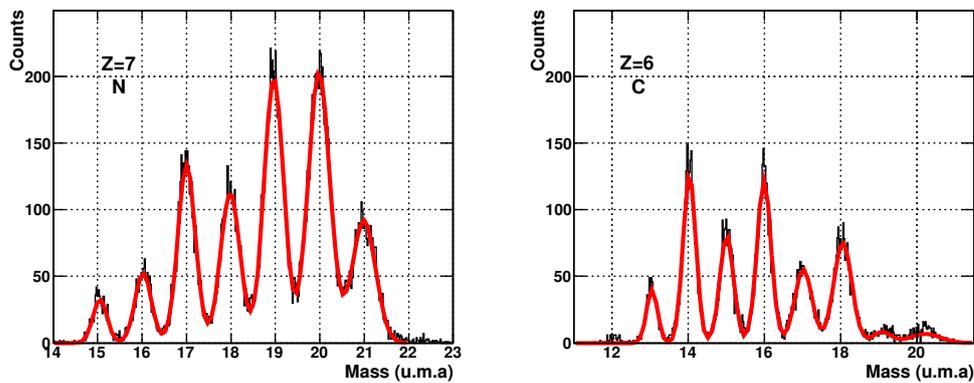
Figure 4.6: Mass spectrum of the outgoing fragments with charges 7 (left plot) and 6 (right plot). The fit parameters are shown in table 4.1.

The left and right neighbours of each peak produce a contribution in the central one. To evaluate the contamination, the number of events in the left and right gaussian neighbours that contribute to the central gaussian is calculated. The ^{21}N produces a contamination in the ^{20}N peak estimated to

Charge 7							
Mean (u.m.a.)	20.98	19.98	18.97	18.00	17.01	16.03	15.06
Sigma (u.m.a.)	0.29	0.26	0.23	0.23	0.20	0.19	0.17
Charge 6							
Mean (u.m.a.)	20.20	19.16	18.05	17.02	15.99	15.01	14.03
Sigma (u.m.a.)	0.29	0.29	0.24	0.24	0.19	0.18	0.17

Table 4.1: Mean and sigma values obtained from the combined gaussian fits in the mass spectra of figure 4.6 for charges 6 and 7.

2.74 %. The contamination of the ^{19}N over the ^{20}N was also evaluated to be 1.07 %.

4.2 Identifying the quasi-free scattering channels

The quasi-free scattering channels are selected by measuring the energies and angular distributions of the two outgoing nucleons from the reaction in the Crystal Ball detector.

To aid the identification an addback algorithm is used. The addback algorithm searches for the maximum energy deposition in a crystal per event. Following this, any energy above threshold in the nearest neighbours is added to the main crystal energy to form a cluster. The central angle of the crystal with highest energy is used to determine the angle of the nucleon emerging from the reaction. To reproduce a more realistic angular distribution, the angles of the central crystals are randomized within the solid angle of the crystal, taking into account the non-uniform crystal shape by the use of a randomization algorithm[2]. As commented previously, the SSDs which are surrounding the target did not work properly. Their sides were either half or completely broken; the angular resolution of the emitted nucleons was determined by the Crystal Ball angular resolution. Another consequence of the malfunctioning of the SSDs is the impossibility to distinguish between neutron and proton in the (p,pn) reactions.

In the simulations chapter, it will be shown the angular signature of the quasi-free scattering: the opening angle of the two nucleons emerging from

---

[2]created by F. Wamers (more detailed information in the reference [30])

the collision it is expected at around $\sim 80^o$. They are travelling back to back in azimuthal angle, being the difference between their azimuthal angles $\sim 180^o$.

In order to remove contributions due to non-physical signals, the energy deposited in a crystal has to be above a certain energy threshold. Studies for energy thresholds between 10 - 25 MeV were performed. For the lowest thresholds has been observed contributions at opening angles below 60°, which do not correspond with the quasi-free scattering angular signature. In order to have a cleaner data distribution and avoid contributions at lower opening angles, the threshold required within this work will be 20 MeV. To consider an event to arise from quasi-free scattering it is also required that the events have cluster multiplicity two (only two clusters per event).

4.3 Cross section calculation and background subtraction

The cross section is a physical observable that reflects the probability that a nuclear reaction will occur. It is defined by the equation 4.2,

$$\sigma = \frac{1}{\alpha} \cdot P_{reac} \qquad (4.2)$$

where α is a factor that depends on the target:

$$\alpha = \frac{\rho_m}{M} \qquad (4.3)$$

with ρ_m the target's mass thickness and M the molar mass. The features of the targets used in the experiment are shown in Table. 4.2.

	ρ_m (g/cm^2)	M (g/mol)	α (1/barn)
CH$_2$	0.922	14.026	0.0397
C	0.935	12.011	0.0469

Table 4.2: Characteristics of the reaction targets used in the S393 experiment.

P_{reac} is the reaction probability defined as follows:

$$P_{reac} = \frac{N_r}{N_a} \qquad (4.4)$$

where N_r stands for the number of reactions that happen for a certain target and N_a stands for the number of attempts (incoming nuclei). The number of attempts will be approximated by the number of survivals after the reaction target and they will be counted at the end of the fragment arm in the TFW detector. This approximation is valid because the target is thin enough and the speed of the particles is very high, so the probability to react in the target is low (10^{-2}-10^{-3}). The number of reactions and the number of incoming will be counted at the last detector. In this way, the efficiencies of the different detectors, the acceptance and other effects are cancelled out because the same detectors and similar conditions are used to perform the counting.

We are interested in the calculation of the cross section with a proton target. The polyethylene (CH$_2$) is formed by carbon and hydrogen atoms. So, we must subtract the carbon contribution using runs with a carbon target. The contribution of other elements in the setup that could cause additional reactions are taken into account by using the so-called empty runs (without target), both of them properly normalized.

The cross section with the hydrogen target is defined as follows:

$$\sigma_H = \frac{1}{2}\sigma_{H_2} \tag{4.5}$$

being σ_{H_2}

$$\sigma_{H_2} = \frac{1}{\alpha_{CH_2}} \cdot (P_{CH_2} - P_{empty}) - \frac{1}{\alpha_C} \cdot (P_C - P_{empty}) =$$
$$= \frac{1}{\alpha_{CH_2}} \cdot P_{CH_2} - \frac{1}{\alpha_C} \cdot P_C + \left(\frac{1}{\alpha_C} - \frac{1}{\alpha_{CH_2}}\right) \cdot P_{empty} \tag{4.6}$$

where α_{CH_2} and α_C are the target factors and P_{CH_2}, P_C and P_{empty} the reaction probabilities for CH$_2$, C and the empty targets, respectively.

4.4 Angular correlations

The quasi-free scattering events have a very strong angular correlation as has also been shown in previous works [23]. The opening angle between the two outgoing nucleons is given by the *dot product* of the unit vectors which describe the particle direction, $\vec{n_1} = \vec{n_1}(\theta_1, \phi_1)$ and $\vec{n_2} = \vec{n_2}(\theta_2, \phi_2)$ (spherical coordinates). This unit vectors are expressed as follows:

$$\vec{n_1} = (sin\theta_1 cos\phi_1, sin\theta_1 sin\phi_1, cos\theta_1) \tag{4.7}$$
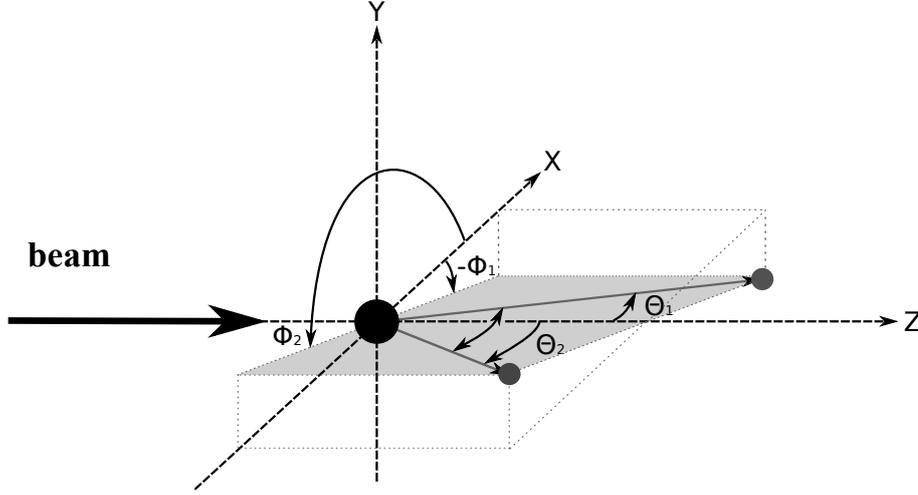
Figure 4.7: Schematic view of a quasi-free event. The laboratory angles of the two outgoing nucleons emerging from a quasi-free reaction are shown in spherical coordinates. The beam comes from the left and impinges in the target.

$$\vec{n_2} = (sin\theta_2 cos\phi_2, sin\theta_2 sin\phi_2, cos\theta_2) \tag{4.8}$$

The opening angle of the nucleons will be

$$\Theta = sin\theta_1 sin\theta_2 cos(\phi_2 - \phi_1) + cos\theta_1 cos\theta_2 \tag{4.9}$$

The difference between the azimuthal angles of the two particles is given by

$$\begin{aligned} \Delta\phi &= \phi_2 - \phi_1 \ , & \phi_2 - \phi_1 \in (0, 180) \\ \Delta\phi &= 360 - (\phi_2 - \phi_1) \ , & \phi_2 - \phi_1 \in (180, 360) \end{aligned} \tag{4.10}$$

4.5 Transverse and longitudinal momentum distributions

One of the physical observables obtained in this experiment is the momentum distribution of the fragment produced in a quasi-free scattering reaction. The momentum distributions contain information about the orbital angular momentum of the removed nucleon in the reaction, i.e. its wavefunction. The total momentum distributions of the fragments are obtained from the tracking procedure and can be divided in two components: the longitudinal

component, that goes in the same direction as the beam and the transversal component perpendicular to it.

$$\vec{p} = \vec{p_{\parallel}} + \vec{p_{\perp}} \tag{4.11}$$

The tracker provides the momentum module (from the fragment mass and β). To determine the momentum module, the tracker approximates the measured mass to an integer and then assign the corresponding nuclear mass.

The longitudinal momentum (from now on it will be called P_Z) will be determined in the laboratory frame and in the rest frame of the projectile. In the rest frame of the projectile it is expressed as follows

$$P_Z = \gamma_{in} \cdot (P_{out} - \beta_{in} E_{out}) \tag{4.12}$$

where γ_{in} and β_{in} are the Lorentz factor and the velocity for the incoming fragment, respectively. P_{out} and E_{out} are the longitudinal momentum in the laboratory frame and the total energy of the outgoing fragment, respectively.

The transverse component can be as well calculated along the X and Y axes as follows:

$$P_X = P \cdot sin(\alpha_{X,out} - \alpha_{X,in}) \tag{4.13}$$

$$P_Y = P \cdot sin(\alpha_{Y,out} - \alpha_{Y,in}) \tag{4.14}$$

where P is the momentum module, $\alpha_{X,out}$ ($\alpha_{Y,out}$) and $\alpha_{X,in}$ ($\alpha_{Y,in}$) are the angles relative to the Z axis in the XZ (YZ) plane for the outgoing and incoming fragments, respectively.

The angular distributions of the fragments after the reactions are reconstructed from the positions obtained with the four in-beam Silicon Strip Detectors (SSDs). In addition to having a good calibration for these detectors, a fine relative alignment between them is needed. A way of testing if the alignment is good lies in calculating the difference between the outgoing and the incoming angle for an empty run. As there is no target, this difference should be around zero. Figure 4.8 shows the angles reconstructed with the different detectors for an empty run when the nominal positions of the detectors were used in the reconstruction. A clear misalignment is observed between the detectors. In order to obtain a reliable transversal momentum distributions a better relative alignment is required. To find the right positions of the detectors, a linear least squares fit has been performed.

The linear least squares fitting technique provides a solution to the problem of finding the best straight line through a set of points. Assuming that the trajectories of our particles are straight lines, the method to find the best-fitting curve to a given set of points consists in minimizing the sum of the squares of the residuals in each detector, defining the residuals as the
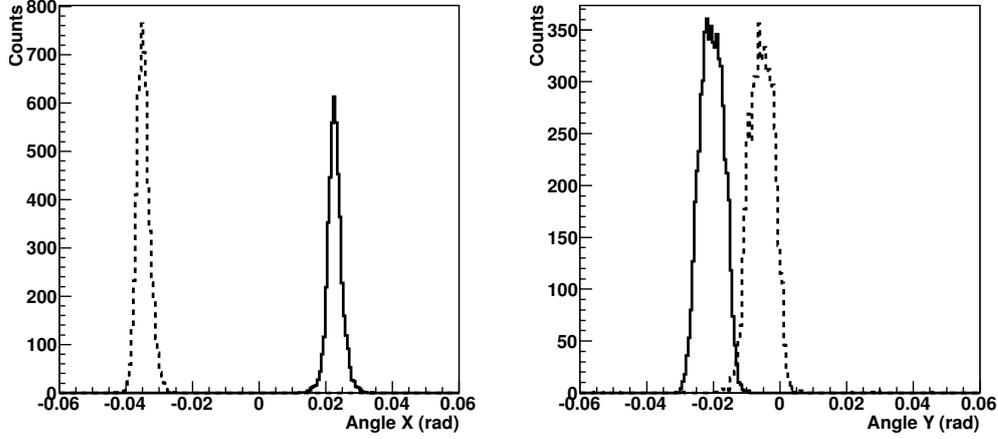
Figure 4.8: Reconstructed angles for the measured hits in the SSDs detectors before and after the target for an empty target run, in the X direction (left) and Y direction (right) for the SSDs. The black dashed lines indicate the angles before the target reconstructed using the first and second SSDs, the solid black lines represent the angles after the target measured by the SSD 3 and 4.

difference between the position of the hits in the detector and the position given by the straight line in the detector plane. The functional to minimize will be

$$f = \sum_{i=x,y;j=1,2,3,4} \left[\left((p_{i_j} + \delta_{i_j}) - (m_i \times (p_{z_j} + \delta_{z_j}) + n_i) \right) \right]^2 \tag{4.15}$$

where p_{i_j} (i = x, y, z and j = 1, 2, 3, 4) stand for the positions of the particles in the detectors and δ_{i_j} are the offsets, which are varied until the minimization of the functional converges. m_i and n_i, are the slope and the offset of the straight line.

The minimization was performed fixing one of the detectors (the third SSD) and obtaining the relative alignment of the others for unreacted beam in a run without target. To perform a complete study of the convergence and correlations between the parameters, two and three dimensional plots for all the variations have been built. The plots for every combination of each two parameters are shown in the appendix A for the X and Y coordinates. The offsets needed in order to align the SSDs are shown in table 4.3. In the Z direction the corrections are negligible.

Figure 4.9 shows the difference in angle in the X and Y components for the ^{21}N after the relative alignment. The distributions are fitted to

	offset X (cm)	offset Y (cm)
SSD 1	0.0522	0.0018
SSD 2	-0.0357	0.0045
SSD 3	0.0	0.0
SSD 4	0.071	0.044

Table 4.3: Obtained offsets for the X and Y coordinates for the SDDs by the minimization.

Gaussians and characterized by its σ, $\sigma_X = (1.373 \pm 0.013)$mrad and $\sigma_Y = (1.126 \pm 0.010)$mrad. The resolution is slightly better in the Y direction. The obtained values are perfectly compatible with previous results using the same detectors [30].
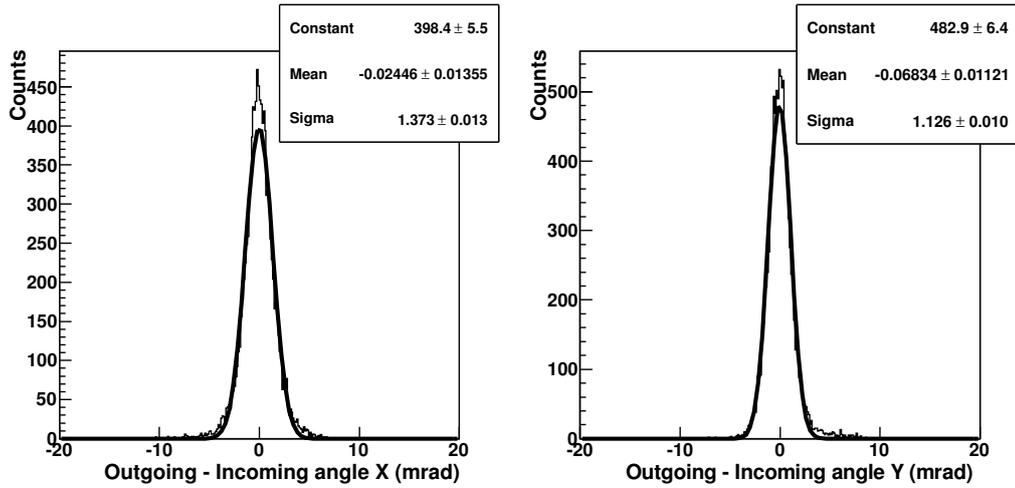
Figure 4.9: Left: distribution of the outgoing angle minus the incoming angle in the X direction. Right: outgoing angle minus incoming angle in the Y direction. The results of a Gaussian fit (thick line) are shown in the inset.

4.5.1 Angular straggling

The charged particles do not follow exactly straight lines. When they traverse matter, they suffer small deviations in their trajectories known as angular straggling. The straggling caused in the different targets is calculated by subtracting quadratically the standard deviations from the Gaussian fits

of the angular differences (outgoing angle minus incoming angle) with and without target.

$$\sigma^2_{straggling} = \sigma^2_{target} - \sigma^2_{empty} \tag{4.16}$$

The standard deviation for the unreacted beam in a run without target gives the intrinsic angular resolution of the setup for a given nucleus at a given energy. In figure 4.10 are shown the $\sigma_{straggling}$ for different targets and
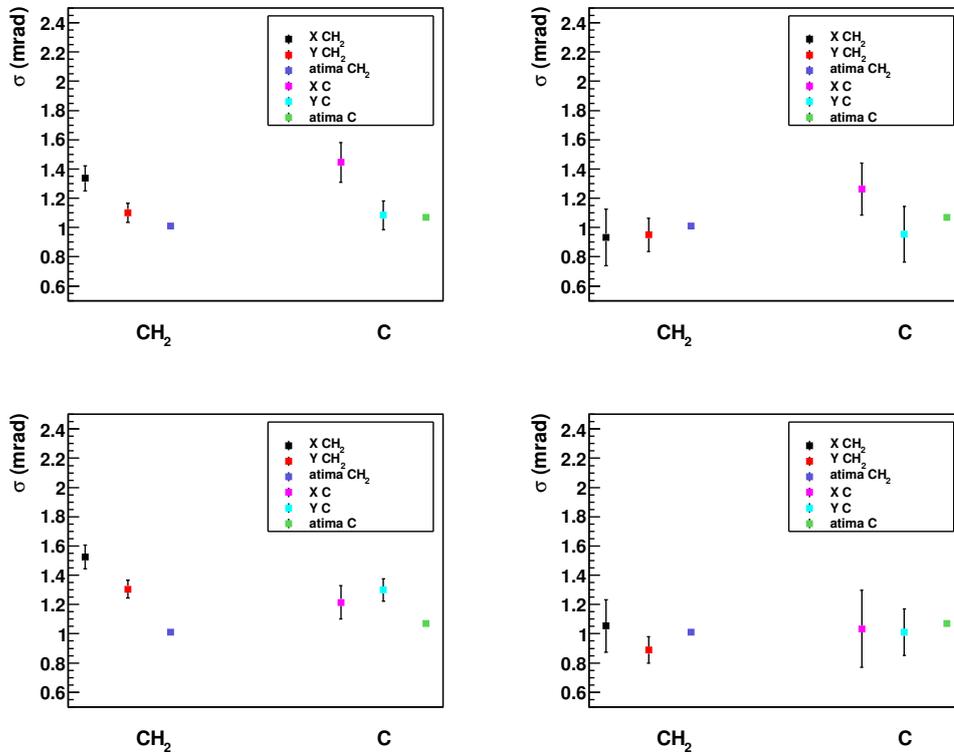
Figure 4.10: Top: results for the σ from a Gaussian fit to the angular differences in X and Y direction and the ATIMA simulation, for the nucleus ^{21}N and for two different kind of fitting. Left: the whole distribution is fitted to a gaussian; right: only the central part is fitted to a gaussian. Bottom: the same information but for the nucleus ^{18}C.

different nuclei. In the top plots the calculations for ^{21}N are shown, on the right when the whole distribution is fitted to a gaussian and on the left when only the central part of the distribution is assumed to be be a Gaussian. These two fits are done because the distributions are not perfectly gaussian. Their tails modify the fit parameters. From these plots it is observed that

the σ values are different in X and Y. If the Gaussian fit is made only the central part, they agree within the error bars and they are also consistent with the calculations performed using the ATIMA [58] code. Big deviations in the results are observed when the whole distribution is fitted to a Gaussian, because of the tails present in the distributions. The biggest deviation is in the sigma of the X component, which is $\sim$18 % larger than the sigma for the Y component. In the bottom figure the same is shown for a different nucleus, in this case ^{18}C, where the same behaviour is observed.

4.6   The addback algorithms for γ's

The energy that a γ deposits in the Crystal Ball detector might not be completely deposited in one crystal, as it was mentioned in Chapter 5. To recover the total energy of the γ emitted by the nucleus, an addback routine is used. In this section different algorithms used to study the γ ray spectra will be explained and discussed.

A difference between γ's emitted by calibration sources and those emitted by reacting nuclei is that, when a particle moves with relativistic energy and emits γ's, these suffer the Doppler effect. In order to calculate the energy of the γ in the rest frame of the particle, the velocity of the excited fragment and the γ emission angle must be known. The correction applied to the energy is shown in equation 4.17, where E_d is the corrected energy, E_{lab} is the energy of the γ measured in the laboratory, γ is the Lorentz constant, β is the velocity of the projectile and θ is the emission angle of the γ with respect to the outgoing fragment direction (which is going to be taken as the angle of the first interaction crystal).

$$E_d = E_{lab} \cdot \gamma \cdot (1 - \beta \cdot cos\theta) \tag{4.17}$$

For all the algorithms used and in order to eliminate noise events, the energy deposited in any crystal has to be above an energy threshold, which has been tested in the range between 100 and 400 keV. Next, a description of the algorithms is presented:

- Method 1 (*spectroscopic*): looks for the crystal with the maximum energy deposited and adds up the neighbour's energies. This set of crystals is defined as a cluster. The cluster energy corresponds to the sum of the component crystal energies and the angle to that of the crystal with the maximum energy. Once a cluster is built, looks for the next maximum energy and adds up the energy of the neighbours until

all the hits in each event are evaluated. The crystals belonging to a cluster are not used in next searchs.

- Method 2 (*maximum energy cluster*): looks for the crystal with the maximum energy deposited and adds up the neighbour's energies. In this method only one cluster per event is built.

- Method 3 (*maximum energy crystal*): in each event only the maximum energy crystal is used, all the others are ignored.

- Method 4 (*calorimetric*): sums the energy of all the clusters found in the first method in one event.
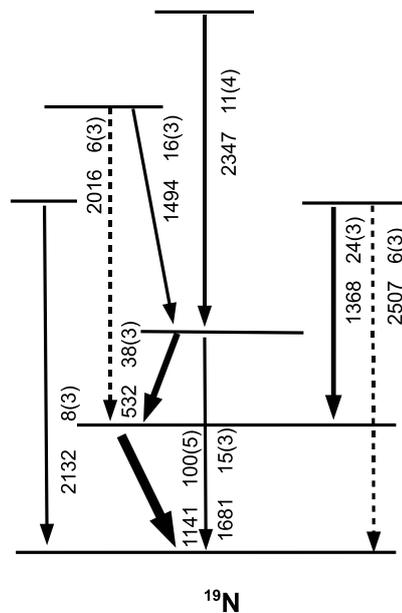
Figure 4.11: Level scheme of ^{19}N proposed in [18]. The vertical numbers indicate the energies and branching ratios calculated by D. Sholer et al. The uncertanties are indicated inside the parenthesis.

Each algorithm has its own purpose. The first one, *spectroscopic*, is suitable to study γ ray spectra where the nuclei decay by any via, is useful to make coincidences. The second one, *maximum energy cluster*, is very useful in situations when only a γ ray is expected to be emitted per event. The third one, *maximum energy crystal*, is very similar to the second, but it is
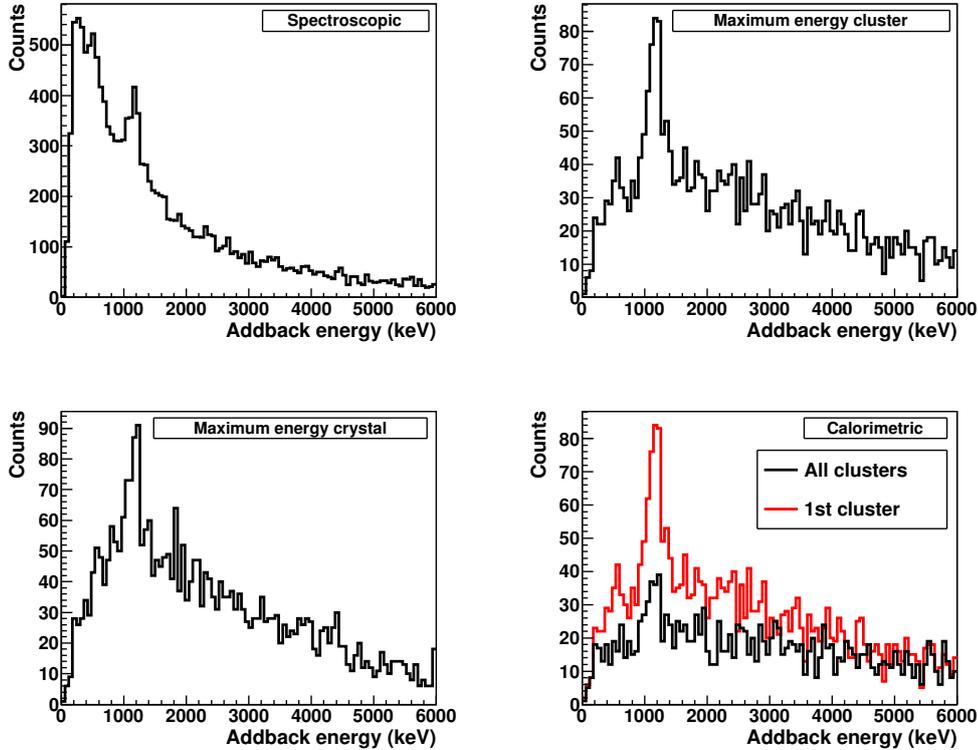
Figure 4.12: γ ray spectra for the four addback algorithm methods described. Top Left: *spectroscopic*. Top right: *maximum energy cluster*. Bottom left: *maximum energy crystal*. Bottom right: *calorimetric*.

more appropriate for low energy γ rays which deposit their full energy in a single crystal. The fourth method, *calorimetric*, could be used in nucleus decaying via a cascade, where we would like to study the sum peak of the γ rays.

The nucleus ^{19}N was chosen to perform this study because it has a simple level scheme very suitable for the comparison of the different methods. The most intense transitions are at 532 keV and 1141 keV according to [18], which are in coincidence. It also has many γ rays weaker which in principle are impossible to identify because of their low intensity.

In figure 4.12 are shown the four γ ray spectra obtained for each algorithm. The top left plot, which presents the result for the *spectroscopic* method, shows a clear peak at about 1141 keV and an increment of the statistics around 532 keV, being this last one mixed with the 511 keV that comes from annihilation, both within the detector resolution at low energies. In

the top right plot is shown the γ ray spectra for the *maximum energy cluster* method. This spectrum is much cleaner at lower energies and the peaks at 532 keV and at 1141 keV are clearly seen. The fact that only uses the maximum energy per event removes background contributions at lower energies in particular, reducing the 522 keV γ. For γ energies below 1000 keV, the most probable effect is the photoelectric, where the energy is mainly deposited in the first crystal hit. When the energy increases the Compton effect begins to become more probable and with some probability energy escapes from the first interaction crystal to its neighbours. Some γ's of 1141 keV or higher will not deposit their full energy in one crystal. This explains why in the bottom left plot, *maximum energy crystal* method, the peak above 1000 keV has more background events than in the second method making impossible to distinguish the 532 keV peak. The bottom right plot shows in black the result for the *calorimetric* method. The red line gives the same result than the second method, showing only the first cluster for comparison. The 532 keV energy peak appears with very low statistics because in most of the cases it will be accompanied by other γ's, showing in the spectra the sum peak. As the more intense transitions are at around 1141 keV and 532 keV, the coincidence peak will be at around 1673 keV.

The figure 4.13 shows the γ energy of one cluster against the γ energy of others, where it is observed the coincidence between the region around 1141 keV and 532 keV. Other coincidence assigments were not possible because of the detector resolution ($\sim$ 20 % at 1 MeV).
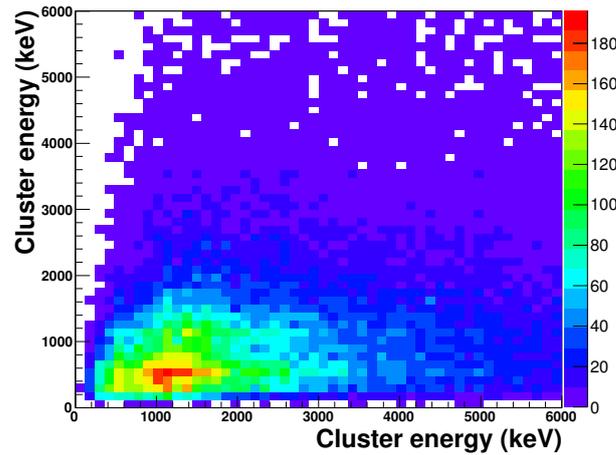
Figure 4.13: Energy of one cluster is represented against the energy of the other clusters.

4.7   The invariant mass

When a nucleon is removed from a projectile via (p,pn) or (p,2p), the excitation energy of the hole could be above the separation energy of a particle (neutron, proton, alpha ...). In this case the system will decay emitting particles and, in some cases, also γ's. In order to reconstruct the excitation energy of the hole left by the nucleon, the invariant mass is used [60, 61].

The invariant mass is a Lorentz invariant and can be expressed in terms of the energy and momentum of the particles

$$M_{inv}^2 = \mathbf{P}^2 = \left(\sum_{i=1}^{N} E_i \right)^2 - \left(\sum_{i=1}^{N} \overrightarrow{p}_i \right)^2 \tag{4.18}$$

where $\mathbf{P}$ is the total four-momentum, E_i and $\overrightarrow{p}_i$ denote the total energy and momenta of all the fragments and the index i sums over all the fragments (N). The invariant masses of the excited nucleus after the reaction (noted with the subscript ε) and the outgoing (noted with the subscript O) are given by

$$(M_{inv})_\varepsilon = m_{proj} + E^* \tag{4.19}$$

$$(M_{inv})_O = \sqrt{\left(\sum_{i=1}^{N} E_i \right)^2 - \left(\sum_{i=1}^{N} \overrightarrow{p}_i \right)^2} \tag{4.20}$$

where m_{proj} is the mass of the excited fragment and E^* is the excitation energy of the hole.

As a first approximation one can assume that the outgoing fragments are produced in their ground states. Using the expressions $E_i = \gamma_i m_i$ and $p_i = \gamma_i \beta_i m_i$, the energy and momentum can be expressed as follows

$$\left(\sum_{i=1}^{N} E_i \right)^2 = \sum_{i=1}^{N} (\gamma_i m_i)^2 + \sum_{i \neq j}^{N} (\gamma_i \gamma_j m_i m_j)^2 \tag{4.21}$$

$$\left(\sum_{i=1}^{N} \overrightarrow{p}_i \right)^2 = \sum_{i=1}^{N} (\gamma_i \beta_i m_i)^2 + \sum_{i \neq j}^{N} (\gamma_i \gamma_j \beta_i \beta_j m_i m_j cos\theta_{ij})^2 \tag{4.22}$$

Using that $\gamma^2 (1 - \beta^2)$ the formula for the outgoing fragments invariant mass is

$$(M_{inv})_O = \sqrt{\sum_{i=1}^{N} m_i^2 + \sum_{i \neq j}^{N} \gamma_i \gamma_j m_i m_j \left(1 - \beta_i \beta_j cos\theta_{ij}\right)} \qquad (4.23)$$

In case that the outgoing fragments are produced in an excited state, the γ energies need to be taken into account and the invariant mass for the outgoing fragments will be

$$(M_{inv})_O = \sqrt{\sum_{i=1}^{N} m_i^2 + \sum_{i \neq j}^{N} \gamma_i \gamma_j m_i m_j \left(1 - \beta_i \beta_j cos\theta_{ij}\right) + E_\gamma} \qquad (4.24)$$

Using the fact that the invariant mass has to be the same before and after the decay, the excitation energy is

$$E^* = \sqrt{\sum_{i}^{N} m_i^2 + \sum_{i \neq j}^{N} \gamma_i \gamma_j m_i m_j \left(1 - \beta_i \beta_j cos\theta_{ij}\right)} - M_o \qquad (4.25)$$

if γ's are considered

$$E^* = \sqrt{\sum_{i}^{N} m_i^2 + \sum_{i \neq j}^{N} \gamma_i \gamma_j m_i m_j \left(1 - \beta_i \beta_j cos\theta_{ij}\right)} - M_o + E_\gamma \qquad (4.26)$$

It is required a complete identification and tracking of all the outgoing particles (fragments, neutrons, protons and γ's) in an event by event basis for the reconstruction of the excitation energy, according to the equation 4.26.

Chapter 5

Crystal Ball simulations

To obtain the physical quantities of interest at a final stage of the analysis, the response of the detectors to different particle interactions needs to be known. In this chapter the Crystal Ball detector simulation results obtained using R3BRoot[1] will be presented.

In the first section, the main features of the simulation program will be outlined. The next ones will be dedicated to the Crystal Ball detector response to γ rays. In these sections the number of particles registered by the detector with their full-energy deposited (photopeak efficiency) will be studied for the individual crystals and for the whole detector. Also the effect of performing an add back will be discussed in terms of total photopeak efficiency. The intrinsic efficiency, which relates the number of counts in a crystal to the number of particles that hit that crystal will also be studied within these sections. The last one will be devoted to the investigation of the detector response to protons and neutrons.

5.1   R3BRoot

R3BRoot [62] is an analysis and simulation framework, specifically iniciated for the future R^3B setup at FAIR [31] by H. Alvarez Pol and D. Bertini (originally), based on a previous simulation code called R3BSim. The program receives most of its features from the FairRoot framework [63], which is based on ROOT [64]. The framework allows the users to implement their detectors or to modify the existent ones, in order to perform simulation and analysis tasks in a simple way. It also contains some general functionality like track visualization, event structure, etc. The analysis is performed in an event-by-event basis, that goes from the unpacking of the data and the

---

[1]http://fairroot.gsi.de/

detector calibrations until the final stage of the analysis, where the different detectors signals are combined in order to obtain the physical quantities of interest. Geant3 and Geant4 transport engines are supported by R3BRoot [65, 66]. The R3B/LAND setup detectors are included in R3BRoot. All the detectors contain a realistic response to particle interaction. Event generators to simulate quasi-free scattering reactions, γ-ray deexcitation, etc. have already been implemented. The program is being used in the design phase of FAIR to optimize the detectors, like for example CALIFA and NeuLAND detectors [67].

5.2 Crystal Ball γ response

One of the purposes of the Crystal Ball detector is to measure the energy deposited by the γ rays detected in coincidence with the outgoing fragment. When the projectile impinges into the target, the outgoing fragments could be produced in an excited state depending on their excitation energy. Information about the structure of the projectile is obtained by studying the populated states. In this section the efficiency for the individual crystals and the whole detector will be calculated in simulation, and compared with experimental data from sources.

5.2.1 Description of the simulation

The detector consists of 159 NaI crystals distributed in a 25 cm radius and 20 cm thickness sphere. There are four different types of crystals. Their shapes are regular pentagons (12 crystals) and three kinds of irregular hexagons (divided in 60 + 60 + 30) (see Chapter 2). Each crystal is inside an aluminum shell of 600 μm, which was also included in the simulation [68].

The particles were generated according to realistic decay schemes implemented for the ^{22}Na and ^{60}Co sources. The simulated sources used, are considered as point sources because the real radiating substance is a little drop of about 0.5 mm in diameter, enclosed in a small rectangular plastic slab of about 2 x 1 x 0.1 cm. The sources were placed in the center of the detector, in the target position. The ^{22}Na source decays via β^+, in 90.326 % of cases emitting a positron. A γ of 1275 keV is emitted because of the ^{22}Ne de-excitation to the ground state. The positron annihilation with one electron of the media produces two γ rays of 511 keV in opposite directions. In 9.615 % of the cases, an electron capture is produced and only a 1275 kev γ ray is emitted. This source was implemented by emitting a γ ray with 1275 keV and two γ rays of 511 keV with opposite directions, all isotropically emitted

Source	γ energies (keV)	decay mechanism
^{22}Na	511, 1275	β^+ (90.326%), EC (9.615%)
^{60}Co	1173, 1332	β^- (100%)

Table 5.1: Calibration sources used in the S393 experiment.

and with the corresponding probabilities. A ^{60}Co source was simulated as well. The ^{60}Co decays to an excited state (2505 keV) of ^{60}Ni via β^-, this de-excites through the 1.332 MeV state. Since the lifetime of this state is very short, the γ ray of 1.173 MeV is emitted in coincidence. In table 5.1 are summarized the sources used.

The crystal resolution has been included assuming a square root dependence with the energy. For each crystal, the fit $\sigma(E) = p_1 * \sqrt{E} + p_0$ was performed and the resulting energy resolution was introduced in the simulation. The figure 5.1 represents the σ from the Gaussian fits to the ^{22}Na peaks vs. the crystal number. It is observed from this plot that depends on the crystal number and also deteriorates when the energy is increased.
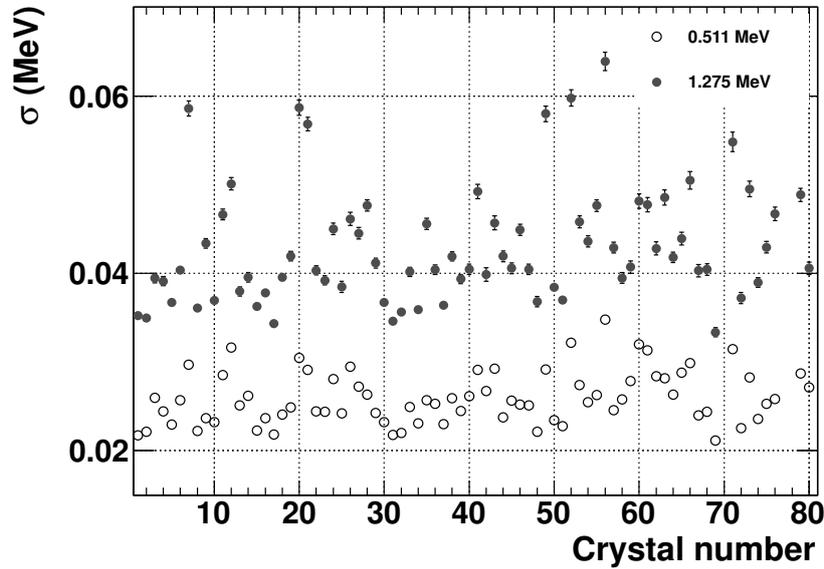
Figure 5.1: Distribution of σ from the Gaussian fits to the individual ^{22}Na peaks vs. the crystal number. The figure show the dependence both on the crystal and energy.

Figure 5.2 shows the simulated energy of the primary γ rays from ^{22}Na impinging upon the crystals (left), and their deposited energy in all the crystals (right). The total amount of primary simulated events was $1 \cdot 10^6$.
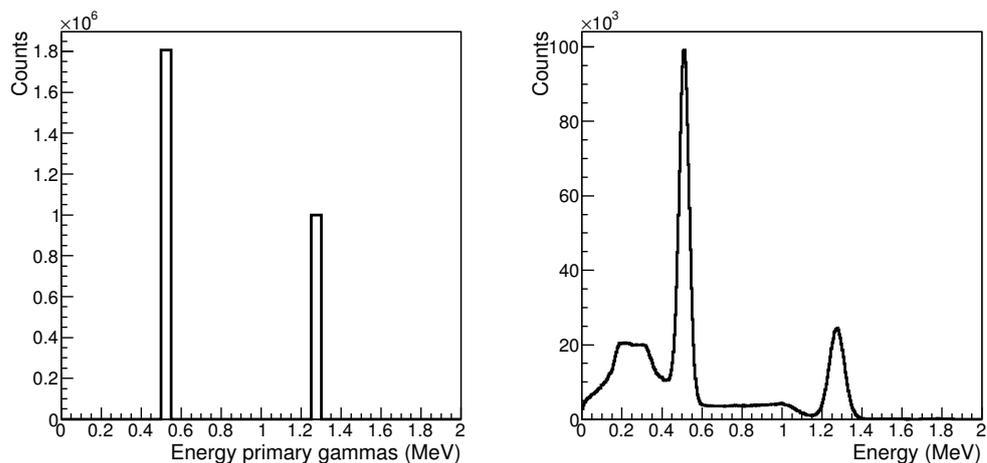
Figure 5.2: Left: energy of the primary γ rays. Right: simulated energy deposition in all the crystals, taking into account the detector response.

5.2.2 Photopeak efficiency for the individual crystals

When a γ ray hits a scintillator crystal, the energy is deposited via three processes: photoelectric, Compton scattering and pair production. The occurrence of any of these processes depends on the energy of the incident γ ray and on the atomic number of the crystal. In figure 5.3 is shown the total absorption coefficient for NaI, together with the contributions of the different processes, as a function of the γ-ray energy. The figure illustrates the importance of each process over a range of γ-ray energy. The photoelectric process dominates in the region up to a few hundred keV. If the photoelectric effect occurs, practically all the photon energy is absorbed in one step. As the energy of the γ rays increases so does the Compton effect probability and if the energy is well above 1.02 MeV pair production rises in significance. At higher γ-ray energies multiple interactions will occur, rendering highly probable that the energy is not deposited only in a single crystal [69].

The photopeak efficiency of the individual crystals is defined as the number of particles registered by the detector with their full-energy deposited, divided by the number of particles emitted by the source. This observable is calculated by counting the number of events within two σ of a Gaussian fit
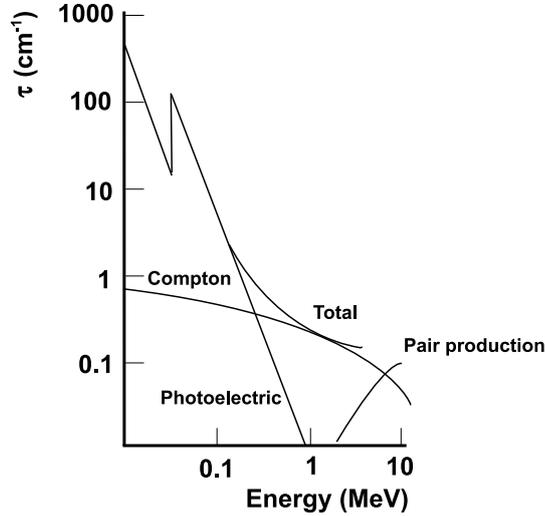
Figure 5.3: Total absorption coefficient of NaI and the contribution of the photoelectric, Compton and pair processes is shown as a function of the γ energy. The figure indicates the importance of each process dependent on the γ energy.

and background (as it was done in figure 3.6) around the centroid of the peak and dividing them by the total number of emitted γ rays. The photopeak efficiency depends on the detector geometry and on the probability of interaction of the particle in the detector. Figure 5.4 shows the photopeak efficiency fitting at two σ for the two γ-ray energies of the ^{22}Na respectively. For the 511 keV γ, the crystal photopeak efficiency mean value is and 0.474±0.097 % while for the 1275 keV γ is 0.297±0.005 % . As it is expected, the more energetic γ, the lower the efficiency. The 511 γ deposits its energy mainly via the photoelectric effect. The Compton scattering probability increases for the most energetic γ, which means that more energy can escape from the crystal without being detected (see more details in [69]).

The total photopeak efficiency, i.e., the photopeak efficiency of the whole detector, can be calculated as the sum of the efficiencies of the individual crystals. The obtained results are shown in table 5.2.
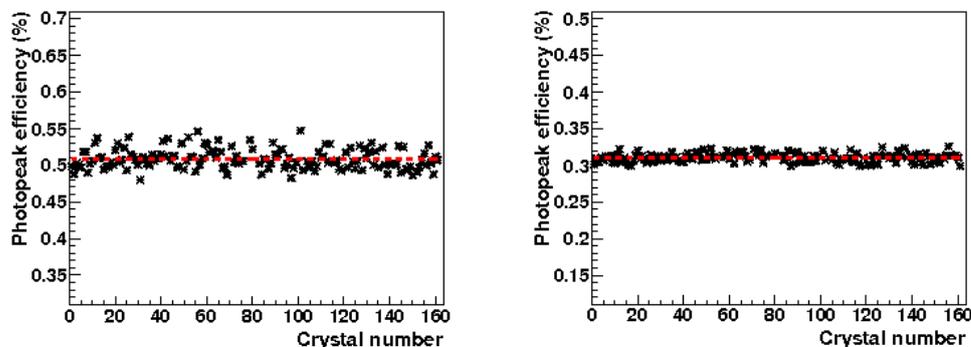
Figure 5.4: Left: photopeak efficiency for each crystal and for the photopeak of 511 keV, integrating the peak at 2 σ's. Right: the same but for the 1275 keV peak. The red dashed lines are the mean values of the photopeak efficiency for each plot.

Peak (keV)	Effiency at 2 σ (%)
511	72.03±0.06
1275	45.17±0.07

Table 5.2: Total photopeak efficiency for the calorimeter at 2 σ's for both energies of the γ source.

5.2.3 Photopeak efficiency for the addback routine

The γ rays will deposit their energy in one or more crystals depending on their initial energy and the interaction process occurred. In order to recover the energy deposited in other crystals in the vicinity of the crystal where the first interaction happened, a routine called addback is applied.

The addback procedure is performed in the same way as for the experimental data: the algorithm searches for the crystal with the maximum energy deposition above an energy threshold and add up the energy of the next neighbors fired. The crystals used are marked as non usable for other clusters in the same event. This is done until all the energies above an energy threshold are employed.

Figure 5.5 shows the fits performed in order to calculate the photopeak efficiency after the addback procedure. Each peak is fitted with a superposition of a gaussian function and a linear function representing the background. The resultant function is used to calculate the integral of the peaks, needed
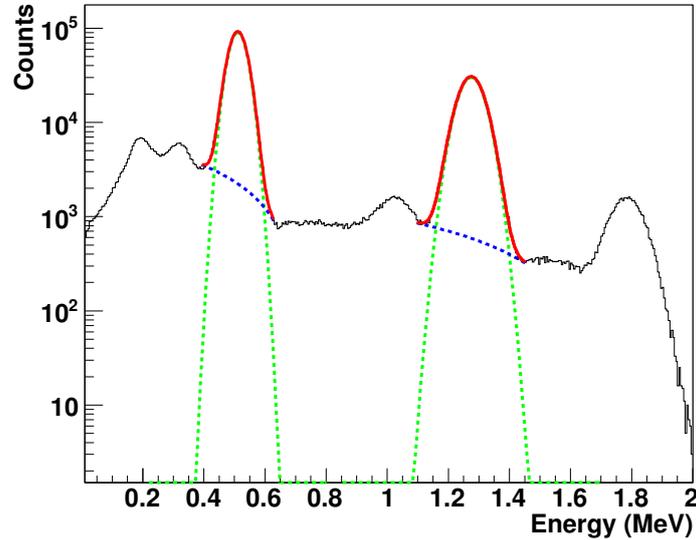
Figure 5.5: Fits performed over the energy deposited in the whole detector after running an addback routine for the total photopeak efficiency calculation.

Peak (keV)	Effiency at 2 σ (%)
511	73.23±0.08
1275	63.64±0.10

Table 5.3: Total photopeak efficiency for the addback calculated for 2 σ's for both energies of the γ source.

for the efficiency determination. Table 5.3 shows the efficiency calculated as the number of counts in the photopeak divided by the number of initial γ's with that energy. The photopeak efficiency at 2σ after addback increases about a 1% for the lowest energetic peak. The increment is bigger for the highest energetic peak where the efficiency increases an 18%. As it was expected, for lower energies the dominant effect is the photoelectric, so the addback routine do not produce a huge improvement. The result of adding the neighbours energies is more notorious for the highest energy γ because of the Compton and the pair production effects.

5.2.4   Intrinsic efficiency using the "Coincidence method"

The intrinsic efficiency relates the number of counts in a crystal to the number of particles that hit that crystal. It is obtained by dividing the total efficiency (number of counts registered by a crystal divided by the number of particles emitted by the source) by its solid angle, for isotropic emission.

In order to compare the results for simulated data with those for real data, the same method must be applied under the same conditions. With this purpose, data with radioactive sources was simulated and taken with the Crystal Ball detector. In this experiment, all the available runs with radioactive sources where measured with the detector separated in two hemispheres. Sources were located at the center of each Crystal Ball hemisphere. The method presented for calculating the intrinsic efficiency is the "coincidence method", which requires a γ source emitting two γ's in cascade and consists in [30, 55]:

- For each event, search for a γ with full-energy deposited E_1 (E_2) in any crystal. The total number of events with one γ (E_1, E_2) is counted. If more than one E_1 or E_2 are found in the same event, this is discarded in order to avoid random coincidences

- If a γ E_1 (or E_2) with the full-energy deposited was found in the previous step, the coincident γ E_2 (or E_1) of the cascade is searched for. The number of γ's which deposited their full energy found in coincidence is counted

- The number of γ's found in coincidence is divided by the total initial γ 1 (or 2) and is corrected by the geometrical efficiency $\epsilon_g = \frac{4\pi/162}{4\pi}$

- In real data, a time condition for the coincidences was also required, the detection time difference between the γ's being less than 15 ns to be considered a real coincidence

It is considered that a γ deposits its full-energy if it is inside the energy window defined by mean $\pm 2\sigma$, with σ being the width of the peak for the crystal.

In the simulations performed the first source tested was the ^{60}Co which has two γ's in coincidence with energies of 1.173 and 1.333 MeV. The results for the intrinsic efficiency of each crystal are shown in figure 5.6. The two γ's have a similar efficiency because their energies are very close. The mean value for the efficiency of the 1.173 MeV peak is 52.24 % with a standard deviation of 8.01% and the one for the 1.333 MeV is 44.17% with a standard deviation of 6.25%.
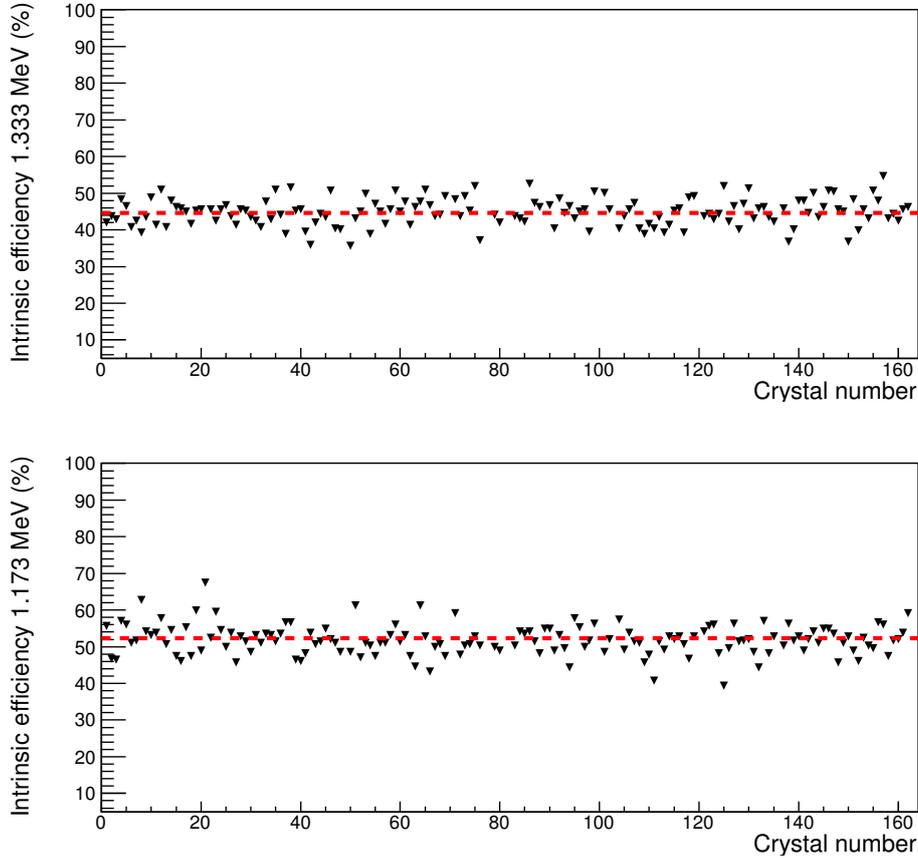
Figure 5.6: Intrinsic efficiency calculation for the γ energies of the ^{60}Co in simulation using the coincidence method. The red dashed lines are the mean values for each plot.

Figure 5.7 shows the efficiency for a ^{60}Co source placed in the left hemisphere of the Crystal Ball detector. The mean value of the efficiency for the 1.173 MeV photon the mean value obtained is 39.31 % with a standard deviation of 8.61 %, while for the 1.333 MeV γ is 26.86 % with a standard deviation of 6.10 %.

The photo peak efficiencies for the two peaks can be compared. In both cases the simulation overestimates the experimental result. There is a clear systematic behaviour in the data, that can be attributed to geometrical factors (positioning of the source inside the detector). A non symmetrical positioning of the source will be reflected in the observed pattern due to the number scheme of the crystals, increasing in spiral.

As in the S393 experiment all radioactive sources data were taken with
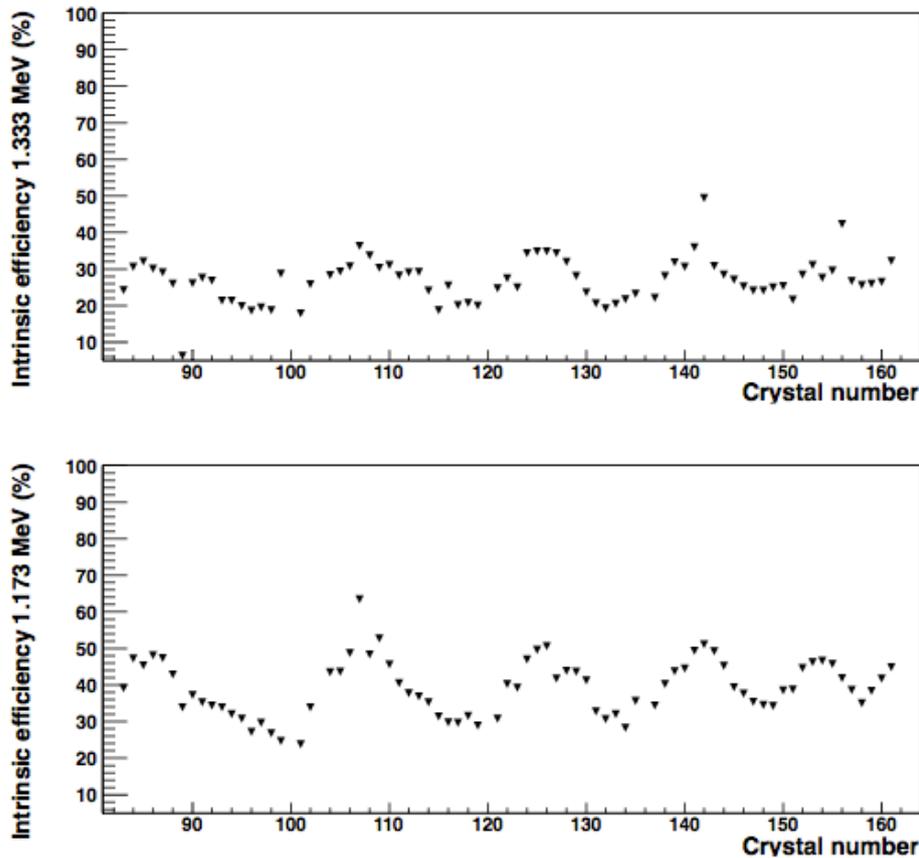
Figure 5.7: Intrinsic efficiency calculation for the γ energies of the ^{60}Co using experimental data. In the top plot is shown the intrinsic efficiency for the most energetic γ (1.333 keV) and in the bottom plot the efficiency for the γ with the lowest energy (1.173 MeV).

the Crystal Ball opened and the source placed in the middle of one of the hemispheres, it would be interesting to have a measurement with the detector closed, together with all the materials inside that are supposed to be there when an experiment is running. After the S393 experiment, and with the same setup, the S389[2] experiment was performed. In that experiment, there were also calibration runs for the "closed" Crystal Ball for comparison. Figure 5.8 shows the comparison between the simulation and the experimental data from S389. In order to well replicate the experimental conditions, the target wheel, its holder, the SSDs and some other materials present in the

---

[2]http://www-w2k.gsi.de/frs/experiments/new/S389.asp

experiment were also included in the simulation. A mean value for each efficiency has been calculated, yielding for the experimental data a mean value of 18.84 % with a standard deviation of 8.05 % for the highest energy peak while in simulation those values are 41.81 % and 7.14 % for the same peak. For the lowest energy peak the mean value is 28.90 % with standard deviation of 18.86 % in real data, and a 44.40 % with standard deviation of 8.92 % for simulation. For both peaks there are some crystals which present large values for the efficiency, due too large values of their resolution taking more events in $\pm 2\sigma$. In the reference [30] it is also shown a comparison between the simulation and the experimental data for the ^{88}Y; it is observed as well a discrepancy between the experimental and the simulated data.
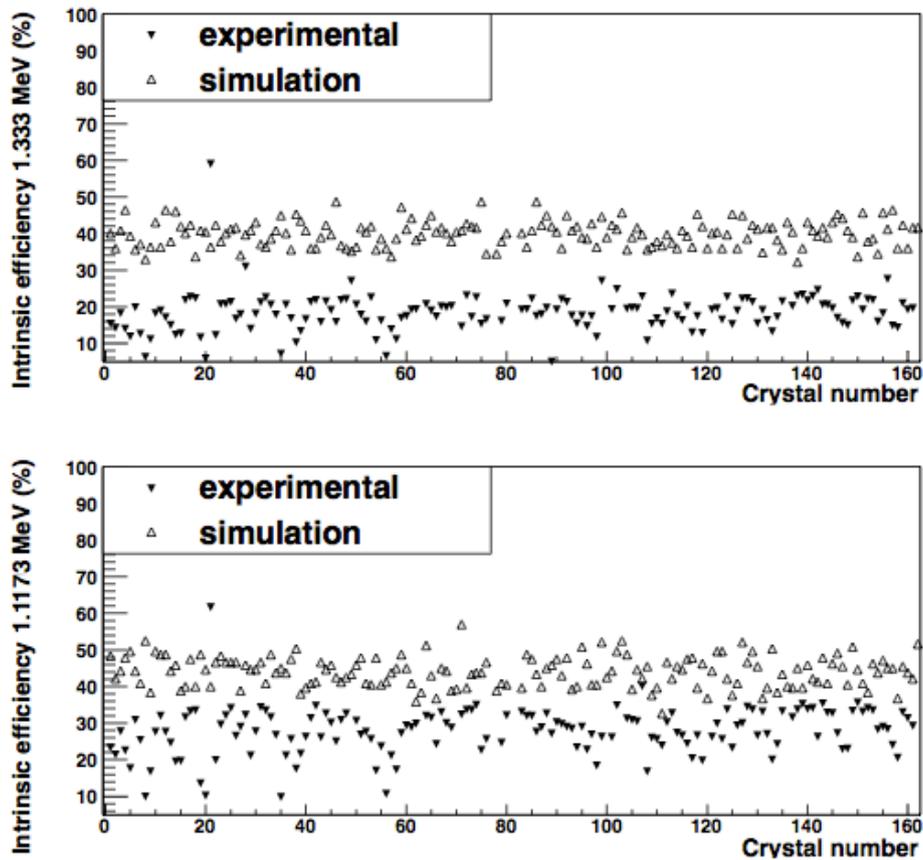
Figure 5.8: Comparison simulation/experiment for the whole detector and for the ^{60}Co source.

A comparison for all the available runs with ^{60}Co source for the S393 and S389 is shown in figure 5.9. In runs 710 and 644 (S389) the source was placed

in the centre and the detector was closed. In the runs 506 and 488 from the S393 the source was placed in the left and right hemisphere respectively.
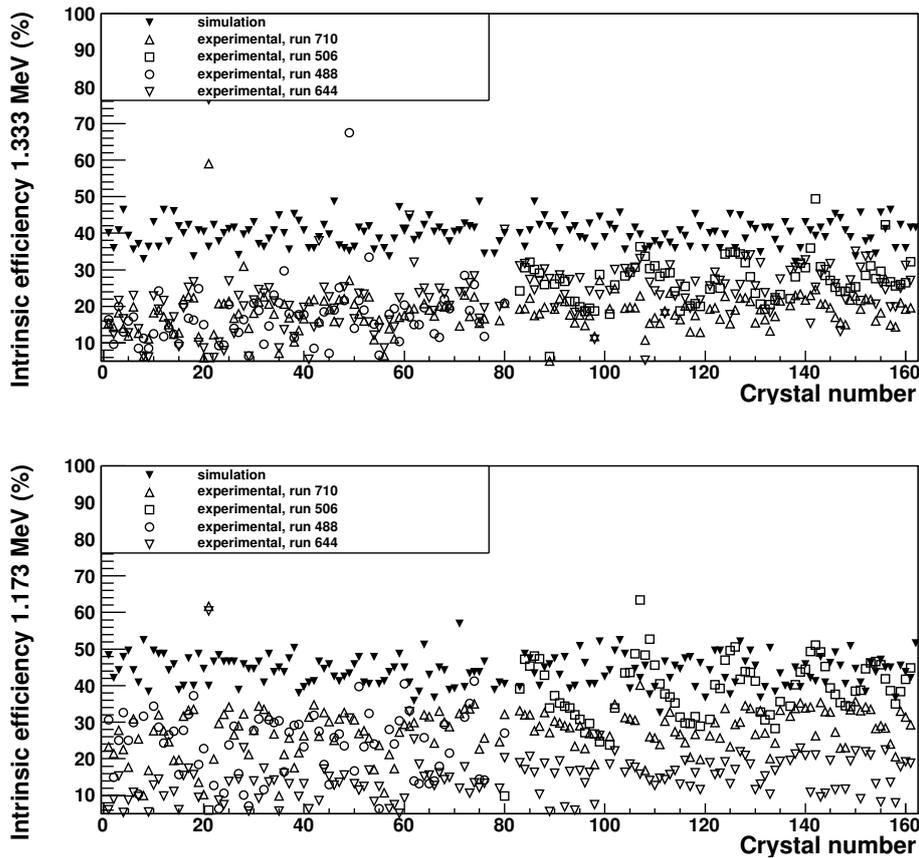
Figure 5.9: Comparison simulation/experiment for all the available runs with the ^{60}Co source (S389).

A comparison between all the available runs with ^{22}Na sources for the S393, including also one run from the experiment S389 is shown in figure 5.10. There are runs where the source was placed only in one half of the detector, for example the 336, the 483 and the 487 covering the right part, the 337, 481, 482 for the left part, while the 730 belonging to the other experiment was recorded with the detector closed. A bigger discrepancy between the simulated and real data is observed for the highest energy peak, while for the lowest energy peak almost all the runs with real data seem to agree better with the simulation. Except the run 730, which belongs to the S389 the others are within three times the standard deviation (6.76 %).

It was observed that in general for all crystals, the simulated response is
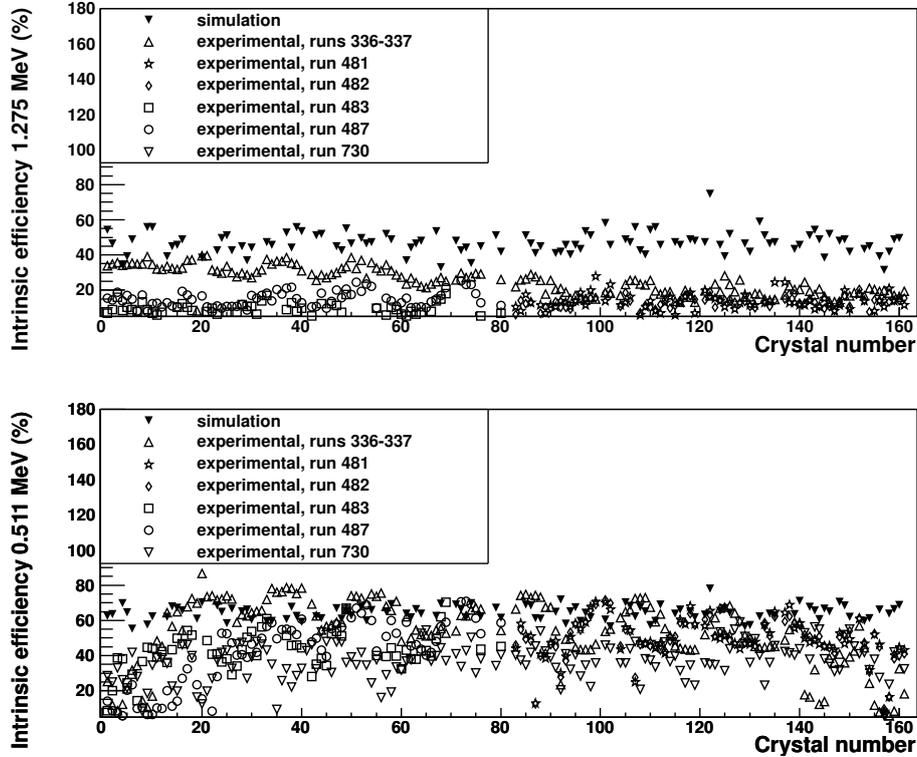
Figure 5.10: Comparison between simulation and experiment for all the available runs with the ^{22}Na source.

larger that the experimental one. In other works [30] they claimed that this could be explained by the fact that there are some materials that are still not included in the simulation. Our results indicate that the experimental source was not placed at the centre of the detector in some of the cases as it was in the simulation. We have performed a set of additional simulations consisting in moving the source a few cm, they revealed a high dependency of the efficiency on the distance from the source to the crystals. One cm cause big deviations in the geometrical acceptance of the detector. The figures 5.9 and 5.10 shown that we can not conclude anything from the experimental intrinsic efficiency, because the same crystal in different runs with different sources presents a very different efficiency, being the simulated values an upper limit for the efficiency distributions.

5.3   Pure kinematical simulations for protons

Quasi-free scattering is used in this work to study the nuclear structure of the projectile. As it was mentioned in previous chapters, when the projectile impinges into the plastic target, among other possible reactions, one proton from the target scatters with one nucleon from the projectile as if both particles were free. In order to simulate the kinematics of the (p,pn) and (p,2p) processes, a code written by L.Chulkov [70] based on the Goldhaber model has been used. From now the code will be referred as "quasi-free event generator". The program was written only for experiment planning, but it is very useful to have information about the angular correlations that we will see in the experimental data. The Goldhaber model [71, 72] is used to calculate the momentum width σ of the fragments.

5.3.1   Description of the code

The program simulates the kinematics of quasi elastic scattering of high-energy protons (or neutrons) on a cluster inside a nucleus. The width of the momentum distributions is calculated as follows,

$$\sigma = \sigma_0 \sqrt{\frac{A_f \cdot (A_p - A_f)}{A_p - 1}} \tag{5.1}$$

where A_p is the projectile, A_f is the spectator and σ_0 is a constant related with the binding energy of a nucleon in the nucleus. The inputs of the program are the kinetic energy of the projectile and the masses of the projectile, the spectator and the two outgoing nucleons.

In the code some approximations are used. It assumes isotropic p-p scattering cross sections, as the beam energy is below 500 AMeV. This approximation is acceptable for pp in our energy range. The term $A_p - 1$ can be approximated by A_p, because $A_p \gg 1$. Finally, a simple model relates the widths of the momentum distributions with the separation energies $\sigma_0 = \sqrt{2 \cdot S_p}$ [73].

As an example, the results obtained for one of the reactions of interest ^{21}N(p,pn)^{20}N are shown in figure 5.11. The opening angle between the two nucleons appears at $\sim 82^o$ and the azimuthal angle shows that the neutron and the proton are emitted back to back. There are a few factors that affect the angular distributions of the scattered nucleons. One of them is the separation energy of the nucleon in the incoming nucleus. The increasing of the separation energy makes the opening angle and $\Delta\phi$ distributions become wider (see [28]). Another factor is the shell where the removed nucleon

is coming from, because the distance travelled by the particles inside the nucleus depends on the shell from which it was removed, which could affect the angular distributions.
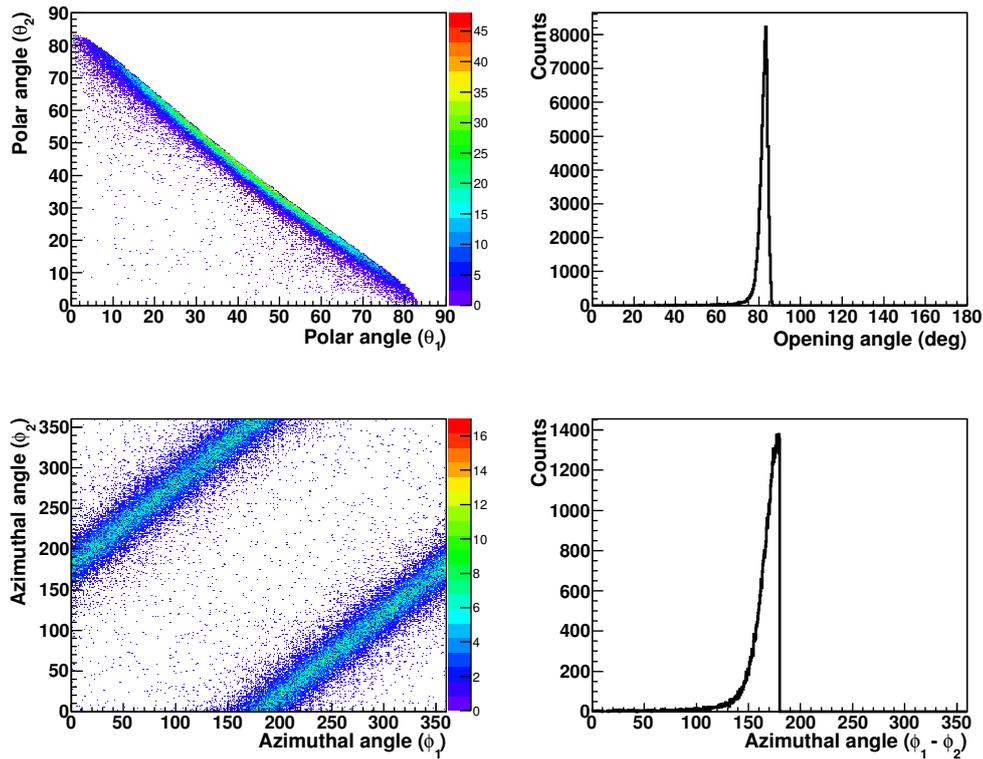
Figure 5.11: Kinematical simulation for the angular correlations of the neutron and the proton emerging from the reaction ^{21}N(p,pn)^{20}N. Top left: shows the polar angle of one of the nucleons versus the polar angle of the other. Top right: shows the opening angle for the neutron and the proton. Bottom left: shows the azimuthal angle of one nucleon versus the azimuthal angle of the other. Bottom right: shows the difference between the azimuthal angles of both nucleons.

5.4 Crystal Ball proton and neutron response

In order to count the number of quasi-free scattering reactions produced, the condition of the detection of two high energy particles in the Crystal Ball is used. To correct the number of reactions counted by the detector efficiency, a simulation was performed. The output from the "quasi-free event

generator" (see Section 5.3) has been used as a realistic event generator, and the corresponding input was given to the simulation framework. The output of the simulation has been analyzed with the same algorithms as those used in the analysis of the experimental data.

5.4.1 Geometrical acceptance of the detector

An investigation about the angular coverage of our detector due to acceptance and losses due to the matter between the target and the detectors, as well the crystals wrappings has been undertaken. For this purpose, the polar angle distribution of the protons emitted by a source measured in Crystal Ball after a randomization[3] is studied. In order to obtain a more realistic angular distribution, a randomized angle within the solid angle of the crystal is used, taken into account the different crystal shapes. As it was commented previously the SSDs "in the box" did not work properly, so the angular resolution of the nucleons is given by the Crystal Ball detector. This detector does not have a high granularity and consequently the angular resolution is poor.

The black line on figure 5.12 shows the polar angle θ of the crystal hit by the nucleon after randomization, while the red dashed line shows the reconstucted distribution obtained via simulation. Polar angles below 9° are empty because the crystal along the beam axis is missing. At angles above 72°, it is observed that the statistics decreases sustantially; this can be attributed to the fact that some high polar angle protons are not able to reach the detector as they have very low energies. Thus, one can establish that the polar angle acceptance for protons is in a range from 9° to 72°.

5.4.2 Efficiency calculations

The main goal of these simulations is to calculate the efficiency of detecting two protons above a certain energy threshold for each crystal in the (p,2p) reactions for different targets, and the neutron and the proton in the same event in the (p,pn) reactions above an energy threshold. The efficiency is defined as the number of events with two detections above the given energy threshold divided by the total number of events.

Table 5.4 shows the efficiencies obtained for both reactions using different targets. As it is expected the efficiency for the empty target is larger because there are no losses produced by the materials. In order to evalu-

---

[3]using a randomization algorithm created by F. Wamers (for a more detailed information [44])
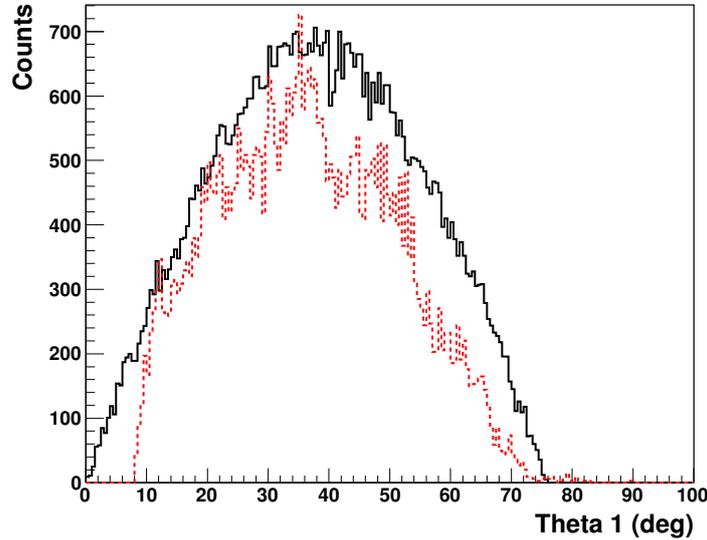
Figure 5.12: Black solid line: Polar angle distribution obtained using the "quasi-free event generator". Red dashed line: polar angle distribution measured by the Crystal Ball in simulation. At lower and higher angles there are acceptance losses, due to the detector geometry and to the energy range of the quasi-free scattered nucleons.

ate the uncertainty for the efficiency, different physics list have been tested[4] (LHEP, QGSP_BERT, QGSP_BERT_HP, QGSP_BERT_BIC, etc.), as well as variations in the target thickness and other interposed matter within the expected tolerances. As a value for the efficiency, the mean value between the largest and the smallest efficiency have been taken, being the estimated uncertainty the deviation of the mean to the largest value. These values are very similar to those obtained by other previous works [74].

	CH_2	C	empty
efficiency p, 2p (%)	63.6 ± 1.5	64.0 ± 1.4	67.3 ± 1.5
efficiency p, pn (%)	17.1 ± 1.8	17.3 ± 1.9	17.4 ± 2.0

Table 5.4: Efficiency calculated for the different targets.

---

[4]See physics lists in
http://geant4.cern.ch/support/proc_mod_catalog/physics_lists/referencePL.shtml

Chapter 6

Results

Based on the reconstruction and analysis methods described in the previous chapter, here we present the results. The complete procedure to extract the physical quantities of interest will be shown in detail only for one of the projectiles, the ^{21}N. In order to reduce innecessary repetitions, the results for other projectiles analyzed using the same methods will be presented in the following chapter with their corresponding plots included in the Appendix C.

6.1 The reaction channel ^{21}N(p,pn)^{20}N

Figure 6.1 shows a schematic layout of the different reactions that could be observed for the ^{21}N. The sketch includes the corresponding energy thresholds for the proton and neutron removal. Starting with the incoming projectile ^{21}N, first the bound channels from ^{21}N(p,pn)^{20}N and ^{21}N(p,2p)^{20}C will be studied via their inclusive cross sections, angular correlations and momentum distributions. Then, the unbound states of ^{20}N will be investigated via the reaction ^{21}N(p,pn)^{20}N*$\rightarrow$^{19}N+n, the inclusive cross sections and excitation energy spectra for this channel will be presented. The lack of statistics for the proton breakup channel channel ^{21}N(p,2p)^{20}C*$\rightarrow$^{19}B+p made the analysis for this reaction impossible.

The ^{21}N projectile was selected from the incoming cocktail beam in the analysis by applying a gate in the charge vs. mass-over-charge ratio (A/Z) plot. The outgoing fragments produced by the ^{21}N in the CH$_2$, carbon and empty targets, were identified by the tracking after the target. The quasi-free scattering channel ^{21}N(p,pn)^{20}N was selected first, by choosing ^{20}N in the outgoing fragments and second, by requiring the events that fullfill the quasi-free scattering condition. This condition requires the detection of a

$S_p = 28.51$ MeV
^{19}B

$S_p = 18.35$ MeV $S_n = 3.34$ MeV
^{19}C

$S_p = 19.60$ MeV
^{20}C

$S_n = 2.16$ MeV
^{19}N

$S_n = 4.59$ MeV
^{20}N

^{21}N
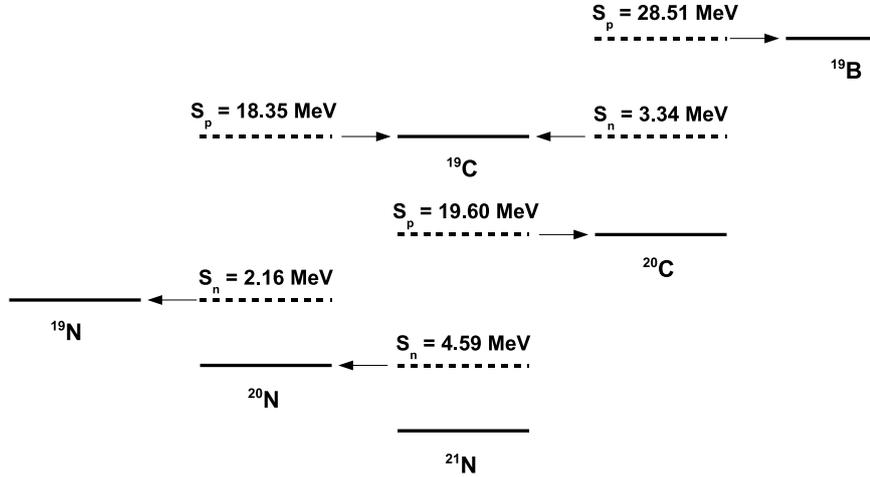
Figure 6.1: Layout of the different decay channels for the incoming projectile ^{21}N, including the proton and neutron separation energies for some of the possible reaction channels.

proton in coincidence with a neutron in the Crystal Ball detector with a given energy threshold, selected to be 20 MeV.

6.1.1   Inclusive cross sections

In this section the results for the inclusive cross sections are presented. *Inclusive* indicates that the final states of the fragments were not distinguished.

Inclusive cross sections were calculated for the channel ^{21}N(p,pn)^{20}N using two different methods. As shown in equations 4.5 and 4.6, the cross section depends on the number of incoming particles, the number of reactions and the target characteristics. The first two quantities can be estimated by selecting the entries inside a two-dimensional elliptical cut in the identification plot charge vs. mass, or can be obtained from one dimensional mass identification plots, via a multi-Gaussian fit (calculating the area of Gaussian distributions).

In the first method, the two-dimensional cut, the number of attempts (projectiles), which is approximated by the number of unreacted nuclei (see 4.3), is obtained from the number of events inside the geometrical cut in the

outgoing identification plot, charge vs. mass (see figure 6.2). This number is corrected by the corresponding downscale factor for the trigger. The contamination from other nuclei in the unreacted is negligible. The number of reacted nuclei is counted in two steps. First, a two-dimensional elliptical cut selects the ^{20}N, in the same manner as for the incoming. Then the quasi-free scattering events are selected. In order to identify them, the addback algorithm is used and the number of reactions is corrected for the efficiency of detecting a proton, in coincidence with a neutron above the threshold in the Crystal Ball.
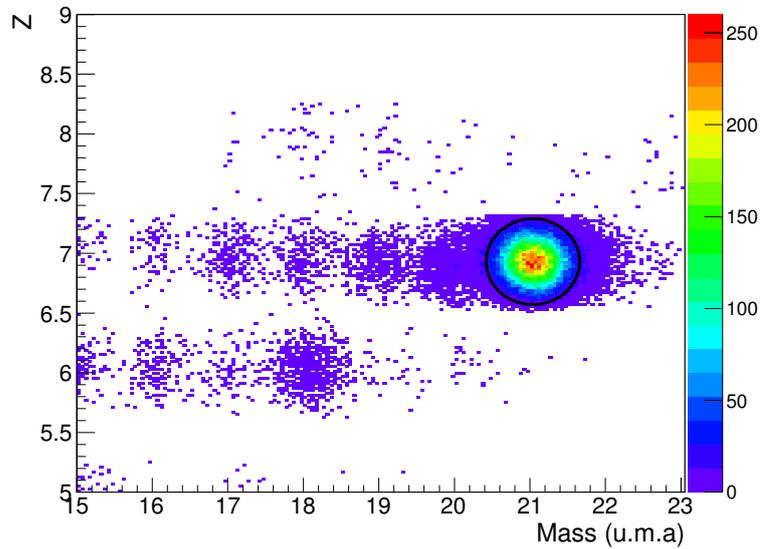
Figure 6.2: Selection cut in the outgoing identification plot atomic number vs. mass. Inside the ellipse the selected events representing the unreacted ^{21}N.

In the second method, the so-called one-dimensional, the number of attempts is determined as the integral of a Gaussian fit to the unreacted ^{21}N tracked mass distribution, as shown in figure 6.3. A selection of fragments with charge 7 and the good beam trigger, was also taken. The number of attempts was corrected by the corresponding downscale factor. The number of reactions was measured by fitting the whole mass distribution to various Gaussians (multi-Gaussian fit). Then, the area of the Gaussian curve corresponding to the ^{20}N peak in the mass identification plot was calculated (figure 6.4). In order to do this, only the outgoing fragments with charge 7 and which fulfill the quasi-free scattering conditions were included. The reacted events are corrected by the corresponding Crystal Ball detection ef-
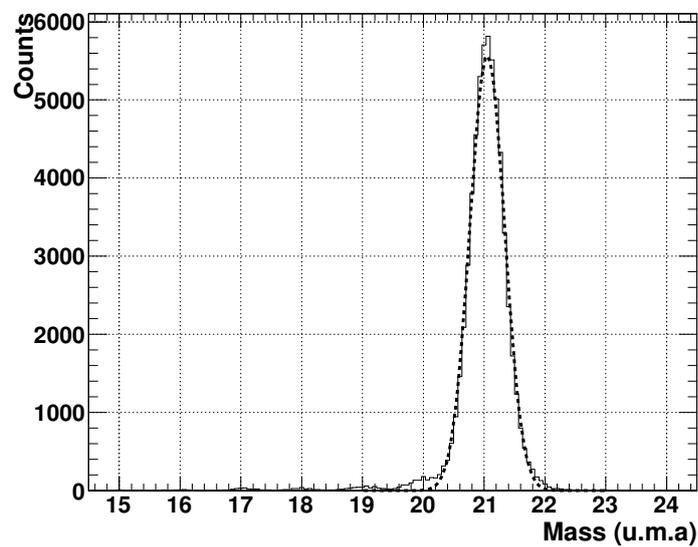
Figure 6.3: Mass identification plot for the non-reacted nuclei with charge 7. The Gaussian fit used o the counting of the number of attempts is also shown.
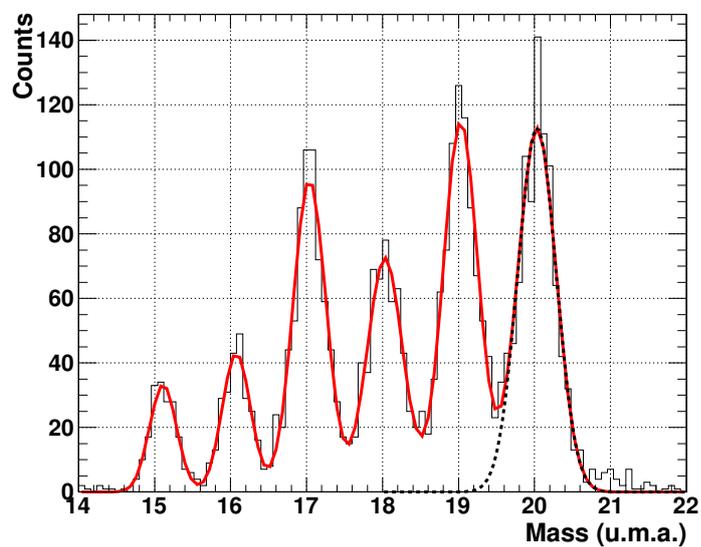
Figure 6.4: Mass identification plot for the quasi free scattering outgoing nuclei with charge 7. A Gaussian fit on the isotope of interest is shown.

ficiency.

	2-dimensional σ(mb)	1-dimensional σ(mb)
CH$_2$	129±16	130±15
C	43.8±8.0	43.8±7.8
H	42.4±8.9	43.7±8.6

Table 6.1: Inclusive ^{21}N(p,pn)^{20}N channel cross sections for the CH$_2$, C and reconstructed H for the 1- and 2-dimensional methods, corrected by the Crystal Ball efficiency for the detection of a proton and a neutron above an energy threshold of 20 MeV in the Crystal Ball detector.

The number of attempts and the number of reactions is measured using both methods for the CH$_2$, carbon and empty targets. Table 6.1 shows the results for the inclusive cross sections using the two explained methods, according to equations 4.5 and 4.6. The uncertainties in the table include statistical and systematical terms (efficiency of Crystal Ball detecting two nucleons in coincidence with the outgoing fragment). Both results are in good agreement within the error bars, proving that the results are robust.

In order to have a unique value for the inclusive cross section on the reconstructed H target, a weighted average $\overline{x}$ with its corresponding uncertainty $\delta\overline{x}$ will be calculated as follows:

$$\overline{x} \pm \delta\overline{x} = \frac{\sum\limits_{i}^{N} w_i x_i}{\sum\limits_{i}^{N} w_i} \pm \left(\sum\limits_{i}^{N} w_i\right)^{-1/2} \tag{6.1}$$

where the weights are given by $w_i = 1/(\delta x_i)^2$, x_i and δx_i being the value and the error calculated via each method [75].

The uncertainty obtained from the weighted average reduces the individual uncertainties of each method, based on the independency of both analysis approaches. But, in this case, the data used for the new two analysis methods is not independent. The procedure has threw light on the evaluation of the systematic uncertainty associated with the methods. Therefore, the statistical uncertainty is incremented by adding an additional evaluation of the dispersion of the results, the variance of the results distribution. The result obtained for the reconstructed proton target using the weighted average is: (43.1 ± 9.0) mb.

6.1.2   Angular correlations
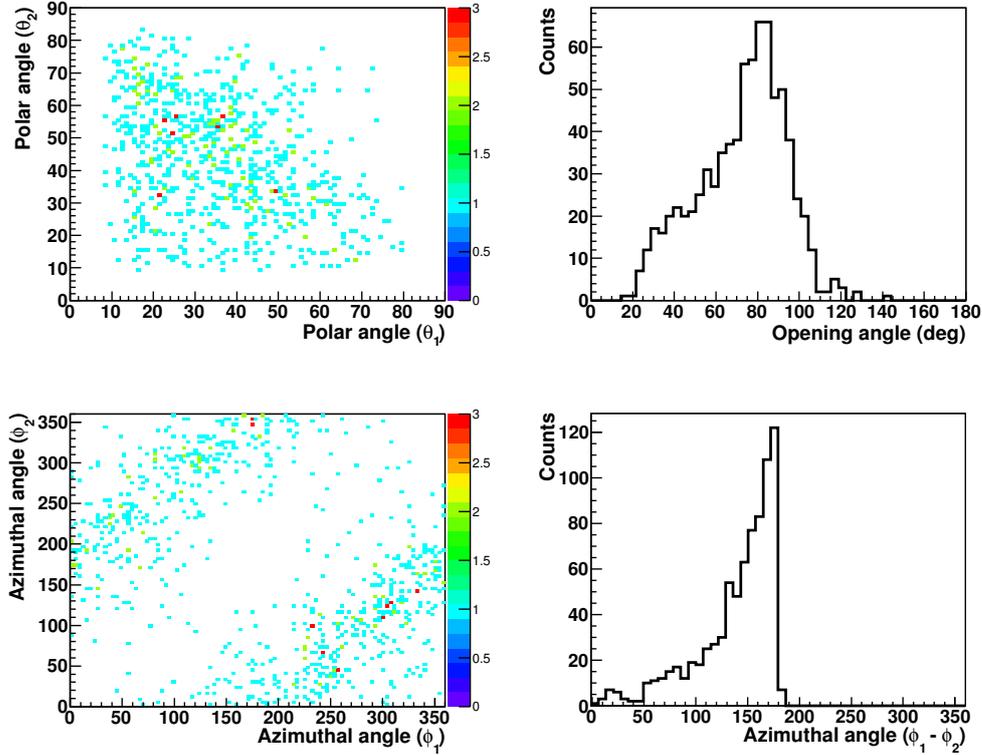
Figure 6.5: Angular correlations of the neutron and the proton emerging from the reaction $^{21}N(p,pn)^{20}N$ observed in the Crystal Ball detector for a CH_2 target. Top left: shows the polar angle of one of the nucleons vs. the polar angle of the other. Top right: shows the opening angle for the neutron and the proton, the peak at $\sim 80^o$ originating from the hydrogen present in the CH_2. Bottom left: shows the azimuthal angle of one nucleon vs. the azimuthal angle of the other. Bottom right: shows the difference between the azimuthal angles of both nucleons, the anticorrelation in azimuthal angle being clearly apparent.

The two outgoing nucleons in a quasi-free reaction, in this case a neutron and a proton, share an opening angle of about $\sim 80^o$ and they are emitted back to back in azimuthal angle.

In figures 6.5, 6.6, 6.7 are shown the angular correlations for the three different targets, CH_2, carbon and empty respectively, used to analyze the reaction of interest. A clear correlation is observed for the CH_2. The peak at around $\sim 80^o$ shown for the opening angle distribution in figure 6.5 is
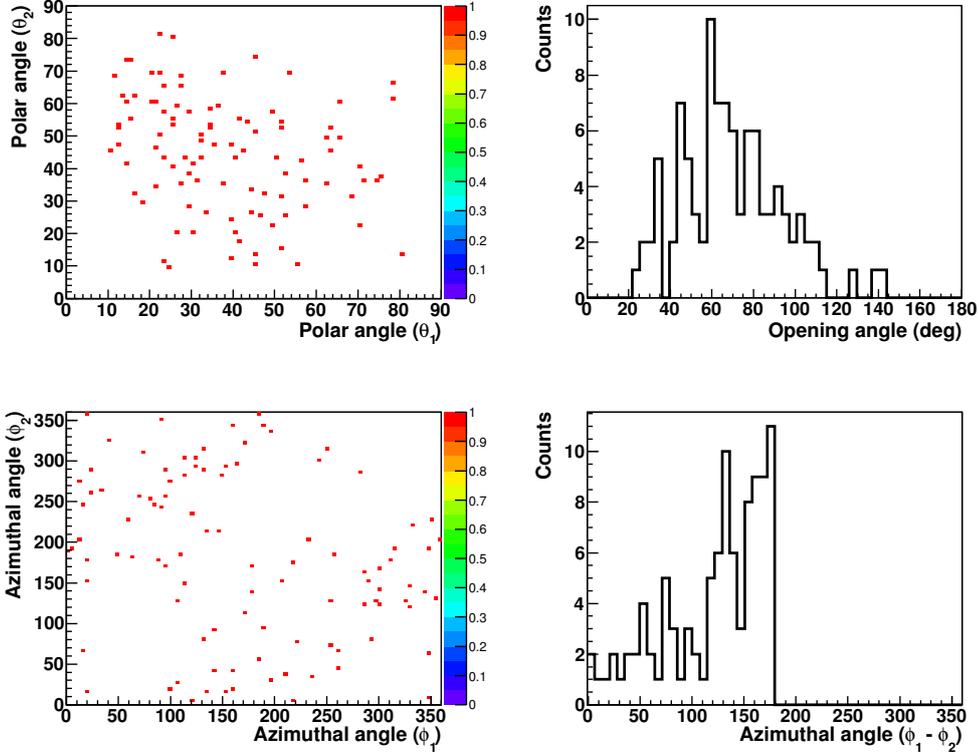
Figure 6.6: Angular correlations of the neutron and the proton emerging from the reaction $^{21}N(p,pn)^{20}N$ observed in Crystal Ball for a C target.

produced by the reactions in the hydrogen present in the CH_2 target, which corresponds with quasi-free scattering events.

The opening angle distribution for the hydrogen target is reconstructed performing the background subtraction (explained in the Section 4.3). The results for the opening angle and the difference between the azimuthal angles is shown in figure 6.8.

The experimental distributions can be compared with the results from a kinematical simulation (described in the Section 5.3). The opening angle distribution in the simulation has a mean value of $82^o \pm 4^o$ (the uncertainty corresponds to the RMS), while the experimental mean value for a Gaussian fit performed at the quasi-free scattering peak is 82° and the width 12°. The two values are in good agreement. In the case of the azimuthal difference, the distributions can be characterized by their mean values and their RMS, obtaining 165° and 18° for the mean and width in the simulation and a mean value of 149° and a width of 27° for the experimental data, respectively. The
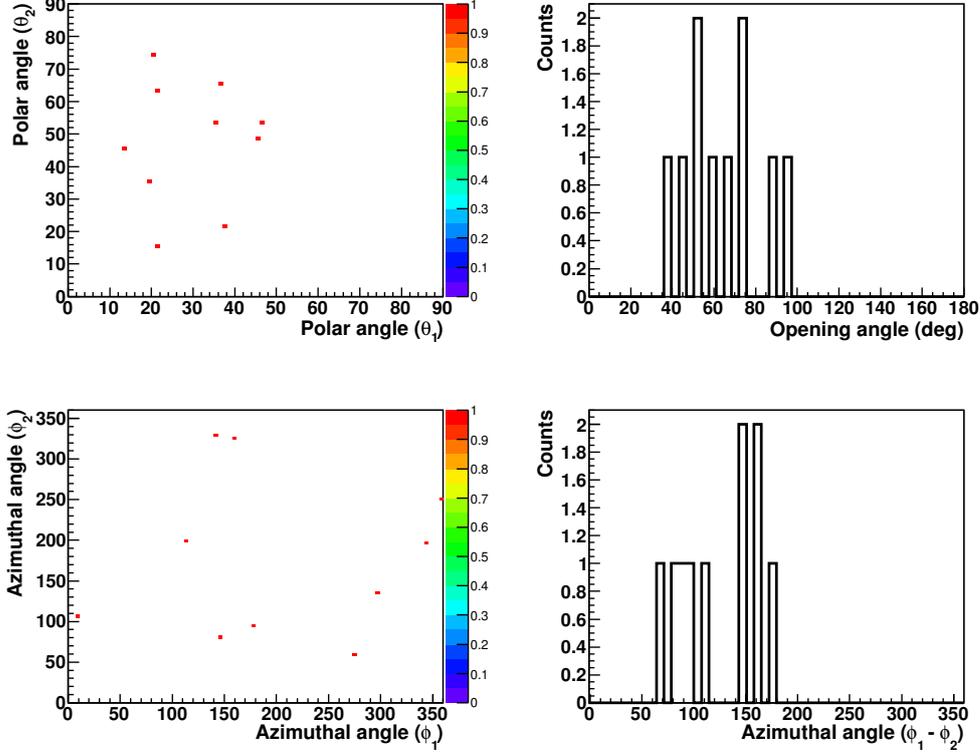
Figure 6.7: Angular correlations of the neutron and the proton emerging from the reaction ^{21}N(p,pn)^{20}N observed in Crystal Ball for an empty target.

two results agree within the distributions mean uncertainties. The deviation from 180° is a consequence of the width of the distribution for the real data, which is highly dependent on the detector resolution and also because of the angle definition itself.

6.1.3   Momentum distributions

The momentum distribution widths and shape contains information about the nuclear structure of the projectiles. In order to study the momentum width, the contribution from the setup must be subtracted. The intrinsic resolution of the setup is contained in the momentum distribution of the un-reacted beam (^{21}N$\rightarrow$^{21}N) when there is no target present. The full width at half maximum (FWHM) of the unreacted distribution will be used to obtain the real FWHM of the momentum distribution for the nucleus of interest. In order to obtain the FWHM corrected, $FWHM_{corr}$ the next formula will be
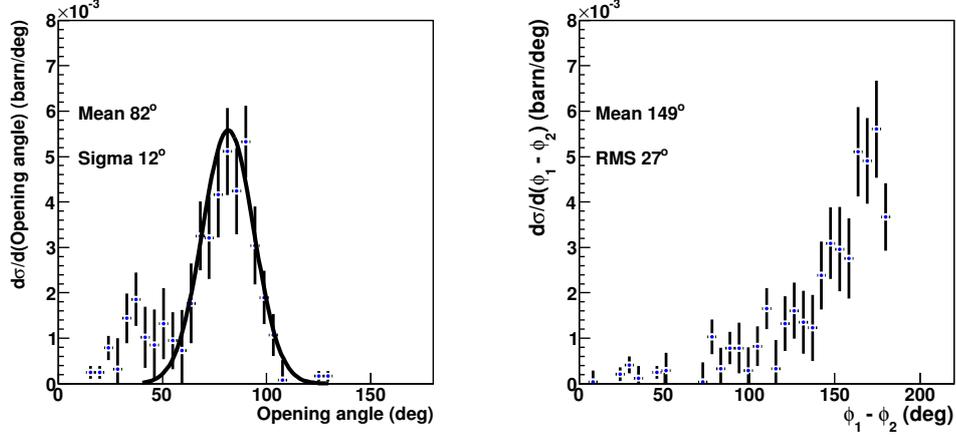
Figure 6.8: Opening angle (left) and difference between the ϕ angles (right) of the neutron and the proton emerging from the reaction ^{21}N(p,pn)^{20}N observed in Crystal Ball for the reconstructed proton target.

used:

$$FWHM_{corr} = \sqrt{FWHM_{tot}^2 - FWHM_u^2} \qquad (6.2)$$

where $FWHM_{tot}$ is the total measured FWHM and $FWHM_u$ is the non-reacted projectile FWHM.

Figure 6.9 shows the unreacted longitudinal momentum distributions for the incoming ^{21}N in the laboratory frame for the different targets. The influence of each target is observed in these distributions. Gaussian fits were performed to extract the mean values for the different distributions, which are very similar, being the differences derived from the energy loss in the inserted targets. The Gaussian widths (σ's) are also very similar. As expected, the empty target run has the highest momentum.

The longitudinal (also transversal) momentum contains the signature of the orbital angular momentum of the shell(s) from which the nucleon was removed [76]. In order to obtain the longitudinal momentum distribution corresponding to the reaction mechanism, we have to subtract the contribution from the incoming nuclei, calculated in the rest frame of the projectile. In figure 6.10 are shown the longitudinal momentum distributions for the different targets in the rest frame of the projectile for the unreacted beam ^{21}N. Each distribution was fitted to a Gaussian and are centred around zero (having mean values of: -2.20±0.38, 1.75±0.68 and -2.63±0.73 MeV/c, for CH$_2$, carbon and empty, respectively). The σ's of the distributions are smaller
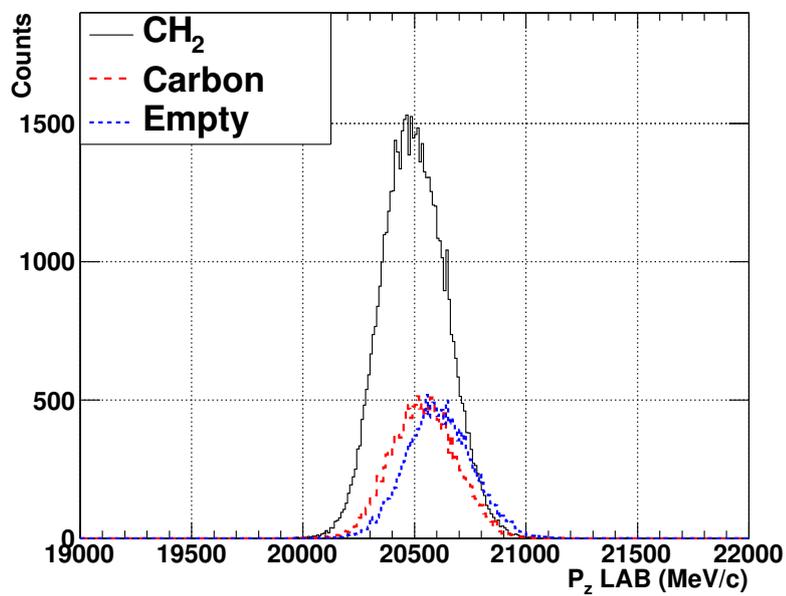
Figure 6.9: Unreacted longitudinal momentum distributions for the incoming ^{21}N in the laboratory frame for the different targets.
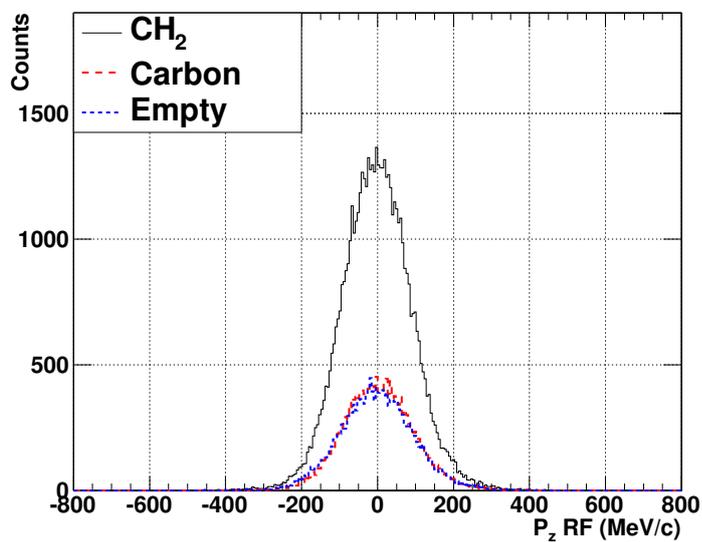
Figure 6.10: Unreacted longitudinal momentum distributions for the incoming ^{21}N in the rest frame of the projectile for the different targets.

than in the laboratory frame because the contribution of the incoming beam is removed when the momentum is expressed in the rest frame of the projectile. The values for the σ's are: 88.92±0.30, 91.23±0.53 and 95.93±0.57 MeV/c for CH_2, carbon and empty, respectively.

The transversal component of the momentum distributions will be studied through the analysis of the Y component of the momentum, due to the malfunctioning of the first SSD, preventing to obtain the X coordinates (see Section 3.7). Figure 6.11 presents the transversal momentum distributions of the unreacted ^{21}N for the CH_2, carbon and empty targets. A Gaussian fit was used to obtain the mean and sigma values. It was found that all the distributions are well centred around zero (mean values -0.66±0.15, -0.65±0.26 and -1.35±0.21 MeV/c). Regarding the momentum widths, the empty distribution is the one with the smallest sigma 23.50±0.19 MeV/c. The other two targets have a very similar width: 30.31±0.13 MeV/c for the CH_2 and 30.45±0.23 MeV/c for the carbon.
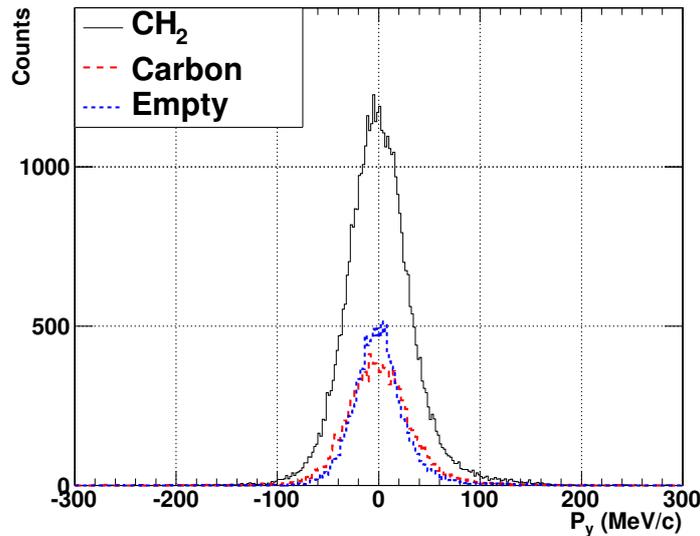
Figure 6.11: Unreacted transversal momentum distribution in Y for the incoming ^{21}N for the different targets.

The longitudinal momentum distributions in the laboratory frame for the outgoing fragment ^{20}N coming from the reaction $^{21}N(p,pn)^{20}N$ are shown in figure 6.12. In the left plot are presented the distributions for the different targets and in the right plot the result after subtracting from CH_2 target the carbon and empty contributions according to equation 4.5. The RMS of the distribution for the reconstructed proton target is 223.6 MeV/c and is

centred at 19380 MeV/c.
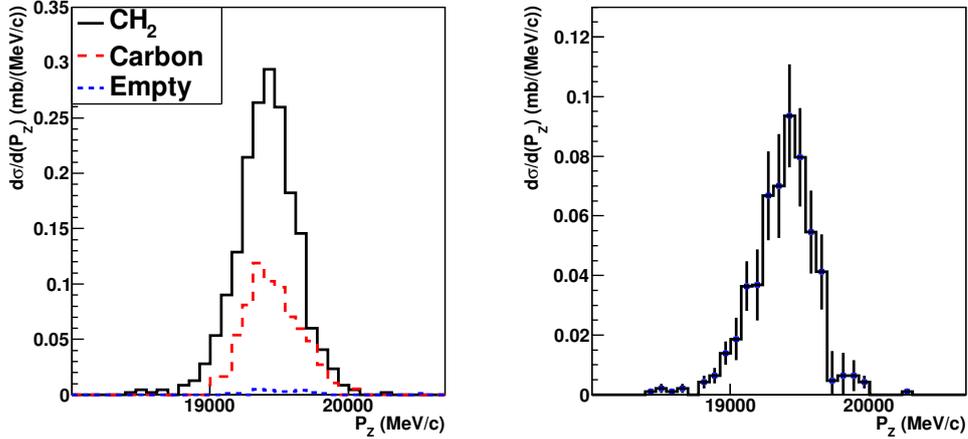
Figure 6.12: In the left plot are shown the longitudinal momentum distributions in the laboratory frame for the CH_2, carbon and empty targets for the reacted ^{20}N. In the right plot is shown the longitudinal momentum distribution in the laboratory frame for the reconstructed proton target.

The longitudinal momentum distributions for the ^{20}N in the rest frame are shown in figure 6.13. The left plot shows the distribution for each target, while in the right plot is the distribution for the CH_2 target after subtracting the C contribution (reconstructed hydrogen target). This has a negative mean value of -98.01 MeV/c and an RMS of 149.6 MeV/c. The mean and RMS values can be compared with the ones obtained for the unreacted beam, where the RMS was around 90 MeV/c and the distribution was well centred around zero, probing that our transformation into the rest frame is correct. The widening in the width of the quasi-free scattering distribution and the observed deviation from zero, are both caused by the reaction mechanism.

Figure 6.14 shows the transversal momentum distribution for all the targets in the left plot and for the reconstructed proton target in the right plot. The RMS is 122.753 MeV/c and the mean value of the distribution is -11.02 MeV/c.

6.2 The reaction channel $^{21}N(p,2p)^{20}C$

In this section the results for the angular distributions, inclusive cross sections and momentum distributions will be shown and discussed for the reaction $^{21}N(p,2p)^{20}C$.
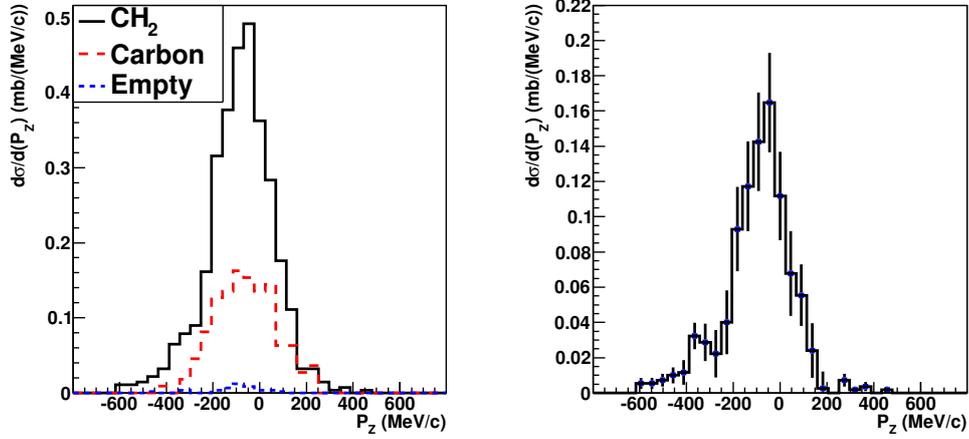
Figure 6.13: In the left plot are shown the longitudinal momentum distributions in the rest frame of the projectile for the CH_2, carbon and empty targets for the reacted ^{20}N. In the right plot is shown the longitudinal momentum distribution in the rest frame of the projectile for the reconstructed proton target.
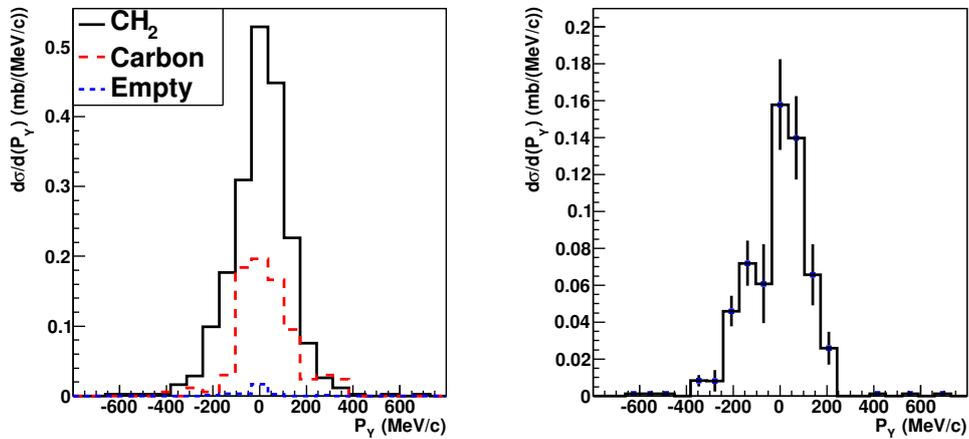
Figure 6.14: In the left plot are shown the transversal momentum distributions in the laboratory frame for the CH_2, carbon and empty targets for the ^{20}N fragment. In the right plot is shown the transversal momentum distribution in the laboratory frame for the reconstructed proton target.

The reaction was selected identifying the ^{20}C after the reaction target in coincidence with two high energy protons in the Crystal Ball detector.

6.2.1 Inclusive cross sections

The inclusive cross sections were calculated via the two analysis methods explained for the (p,pn) channel in Section 6.1.1 and exemplified for the (p,pn) channel. The results obtained are shown in table 6.2. Both methods agree within the error bars. The total inclusive cross section using the weighted average and considering the different uncertainty contribution is: (2.08±0.49) mb.

	2-dimensional σ(mb)	1-dimensional σ(mb)
CH_2	5.70±0.56	5.76±0.55
C	1.69±0.49	1.46±0.45
H	2.00±0.37	2.15±0.35

Table 6.2: Inclusive ^{21}N(p,2p)^{20}C channel cross sections for the 1- and 2-dimensional methods, corrected by the Crystal Ball efficiency.

6.2.2 Angular correlations

The opening angle and the difference in the azimuthal for the two protons are presented in figure 6.15 for the reconstructed proton target. The opening angle distribution was fitted to a Gaussian, yielding a mean value 79° and a sigma of 9°. A simulation was performed in the same way as it was done for the (p,pn) channel, obtaining a mean value of 72° and an RMS of 10°. Both results are in reasonable agreement. The difference between the azimuthal angles was found to have a mean value of 157° with an RMS of 20° being in reasonable agreement to 146° and 33° obtained for the mean and RMS values in simulation.

6.2.3 Momentum distributions

The longitudinal momentum distribution in the laboratory frame was found to be centred at 19300 MeV/c with an RMS of 146.1 MeV/c (see figure 6.16). Figure 6.17 shows the longitudinal momentum in the rest frame of the projectile. The distribution is centred around -122.4 MeV/c and has an RMS value of 103.3 MeV/c. It exist a considerable deviation from zero, which is caused by the reaction. The transversal momentum distribution is shown in figure 6.18, and is centred at -13.83 MeV/c with an RMS of 108 MeV/c.
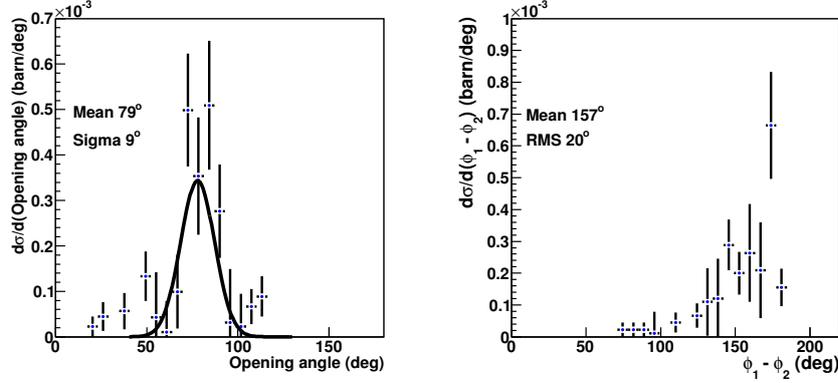
Figure 6.15: Opening angle (left) and difference between the azimuthal angles (right) for the two protons emerging from the reaction ^{21}N(p,2p)^{20}C observed in Crystal Ball for the reconstructed proton target.
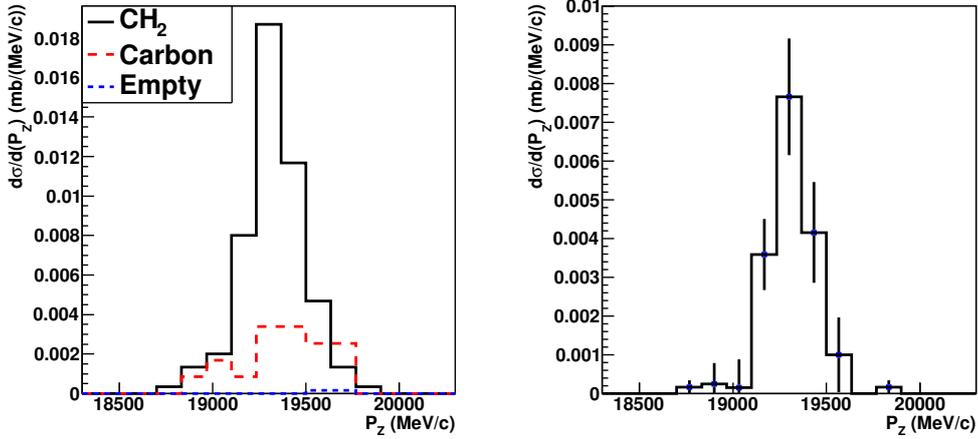
Figure 6.16: In the left plot are shown the longitudinal momentum distributions in the laboratory frame for the CH$_2$, carbon and empty targets for the reacted ^{20}C. In the right plot is shown the longitudinal momentum distribution in the laboratory frame for the reconstructed proton target.

6.3 The breakup channel ^{21}N(p,pn)^{20}N* $\rightarrow$^{19}N+n

After the knockout of a neutron from the ^{21}N nucleus, a hole is created in a given neutron shell and, depending on the excitation energy of this residual hole state in the ^{20}N, a particle could be emitted. In this case, the reactions with enough excitation energy to evaporate a neutron (2.161 keV) will be
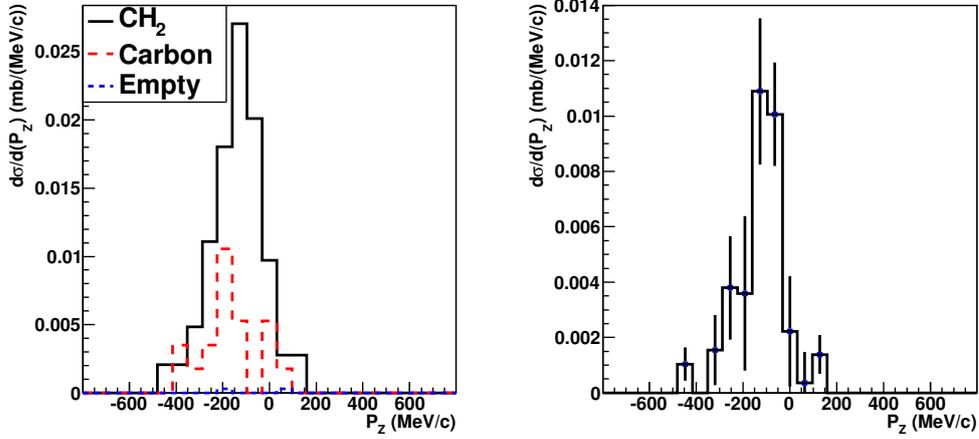
Figure 6.17: In the left plot are shown the longitudinal momentum distributions in the rest frame of the projectile for the CH_2, carbon and empty targets for the reacted ^{20}C. In the right plot is shown the longitudinal momentum distribution in the rest frame of the projectile for the reconstructed proton target.
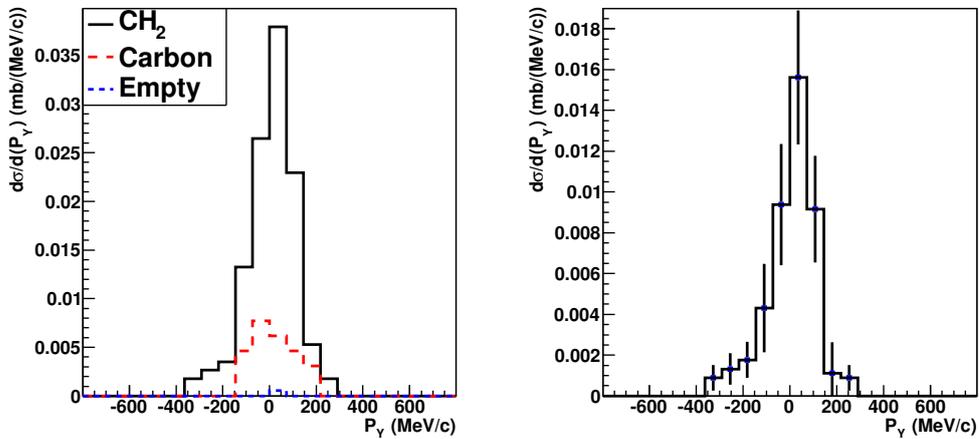
Figure 6.18: In the left plot are shown the transversal momentum distributions in the laboratory frame for the CH_2, carbon and empty targets for the reacted ^{20}C. In the right plot is shown the transversal momentum distribution in the laboratory frame for the reconstructed proton target.

studied. This channel was investigated by measuring in coincidence the outgoing fragment ^{19}N and a neutron in the LAND detector in coincidence.

The neutron multiplicity distribution measured with the ^{19}N fragment after selecting an incoming ^{21}N and quasi-free scattering conditions is shown in figure 6.19. In most of the cases only one neutron is observed.
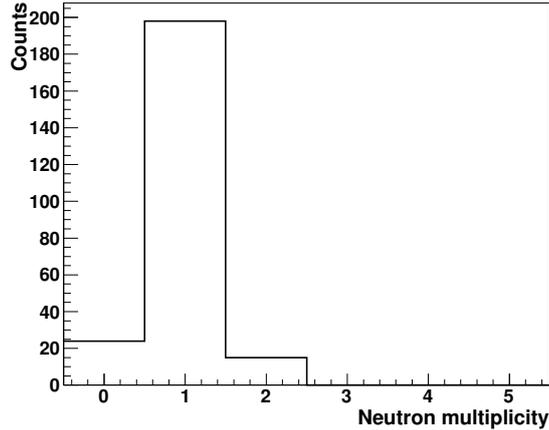
Figure 6.19: Neutron multiplicity in LAND for coincidences with (p,pn) reactions in QFS regime in the CH$_2$ target.

The time of flight between the target and LAND was used together with the position information obtained from the neutron detector to calculate the neutron velocity [47]. To calibrate the time of flight, γ rays produced in the target are used. These γ's present a narrower distribution than the neutrons and appear at earlier times because γ's travel with the speed of light. The LAND time offset is set by moving this γ peak to zero. The *land02* package includes an algorithm which reconstructs the spherical coordinates [47] of the neutron hits in LAND. The information needed from the fragment is obtained via the tracking program and the two SSDs after the target. In the left plot of figure 6.20 is shown the neutron velocity distribution, which has a mean value of (22.02±0.94) cm/ns. The angle between the fragment and the neutron is shown in the right plot of figure 6.20 and has a mean value of 42.37 mrad ($\sim 2.86^o$) and an RMS of 20.5 mrad.

The neutrons arising from an evaporation reaction reach LAND with a velocity very similar to the beam. The background events coming from reactions which occur after the target are slower than the evaporated neutrons and could be identified by plotting the neutron energy vs. the fragment mass. In figure 6.21 is shown an example of the neutron velocity distribution as a function of the fragment mass for a CH$_2$ target for the incoming projectile ^{21}N. The events inside the window at (20, 25) cm/ns are neutrons which came from evaporation. The tail for lower velocities observed at mass A =
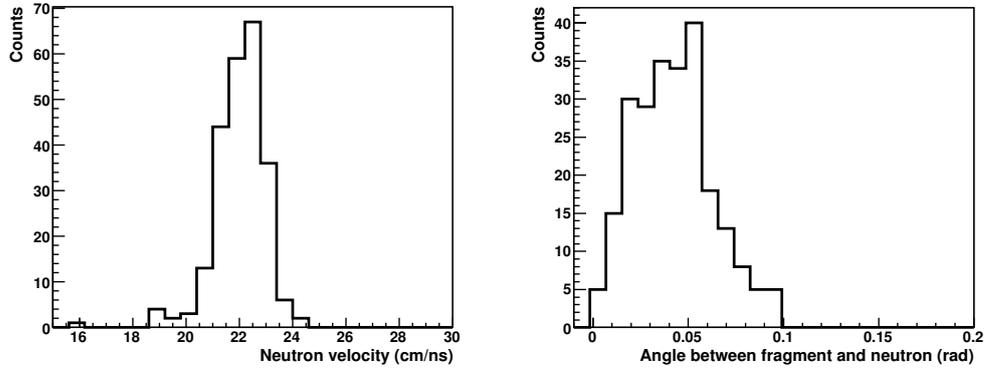
Figure 6.20: Neutron velocity distribution in LAND (left) and their angles with the ^{19}N fragments (right) measured in coincidence with the (p,pn) reactions for the CH$_2$ target (see text for further explanation).

21 is due to the beam. Only events inside the mentioned window are used for the calculation of the excitation energy and the cross section.
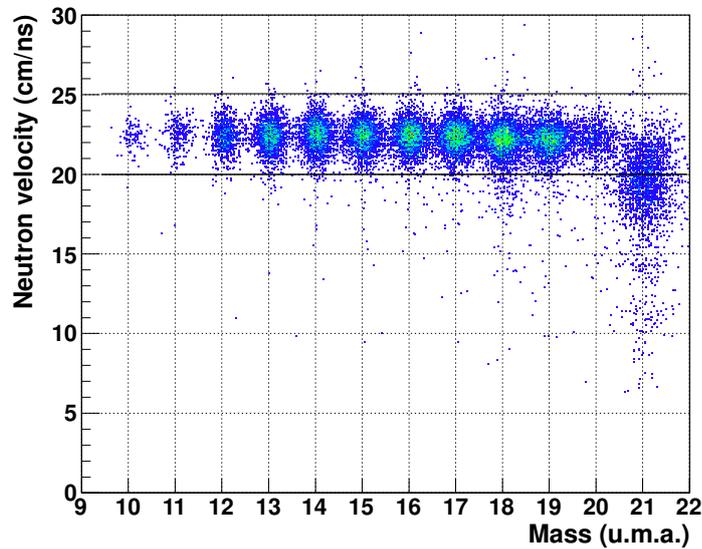
Figure 6.21: Neutron velocity vs. fragment mass for the incoming ion ^{21}N. The LAND trigger was selected. The band between the two black lines shows the neutron events from evaporation.

The probability of detecting one neutron in LAND for a given channel has a strong dependence on the neutron kinetic energy. The number of detected

neutrons has to be corrected for the detector efficiency. An efficiency distribution was provided by D.Rossi [77] using the simulation code LEG[1]. Figure 6.22 shows the efficiency distribution of detecting one neutron in LAND. The drop in the reconstructed efficiency above 3.3 MeV is due to the acceptance of LAND. Up to that neutron energy, LAND has almost a 100 % acceptance. Beyond that energy, a portion of the neutrons pass through LAND, and that portion increases with the increasing of the neutron energy.
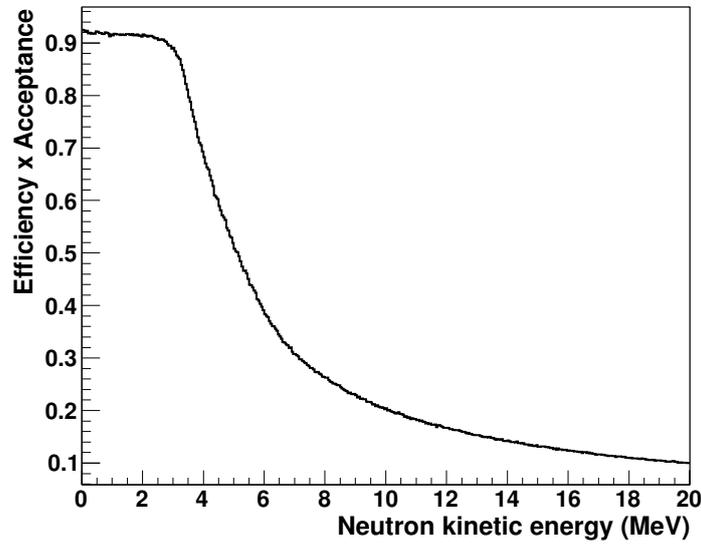
Figure 6.22: Detection efficiency as a function of the neutron kinetic energy for the detection of one neutron in LAND calculated via simulation using the LEG code (see text for details).

To correct for the efficiency, the neutron kinetic energy must be determined. For that purpose the Lorentz-transformation of momentum-energy is used:

$$\begin{pmatrix} E^{RF} \\ p_\parallel^{RF} \end{pmatrix} = \begin{pmatrix} \gamma_f & -\beta_f\gamma_f \\ -\beta_f\gamma_f & \gamma_f \end{pmatrix} \begin{pmatrix} E \\ p_\parallel \end{pmatrix} \tag{6.3}$$

where E^{RF} and $p_\parallel^{RF}$ are the energy and the longitudinal momentum in the rest frame, β_f and γ_f are the velocity and the Lorentz factor and E and $p_\parallel$ are the energy and longitudinal momentum in the laboratory frame. With

---

[1]Land Event Generator

the help of equation 6.3 it is possible to relate the energy of a particle in the rest frame with its energy in the lab frame

$$E^{RF} = \gamma_f E - \beta_f \gamma_f p_\parallel \tag{6.4}$$

Using $E = \gamma m_0 = E_{kin,n} + m_0$ and equation 6.4, the neutron kinetic energy in the rest frame is expressed as

$$E_{kin,n} = \gamma_f \gamma_n m_n - \beta_f \gamma_f p_{\parallel,n} - m_n \tag{6.5}$$

where γ_f and γ_n are the Lorentz factors for the fragment and the neutron respectively, m_n is the neutron rest mass, β_f is the velocity of the fragment and $p_{\parallel,n}$ is the longitudinal momentum of the neutron in the lab frame which is calculated as follows

$$p_{\parallel,n} = m_n \beta_n \gamma_n cos\theta \tag{6.6}$$

with θ the angle between the outgoing fragment produced in the quasi-free scattering reaction and the neutron.

In figure 6.23 is shown an example of the excitation energy distribution before and after correcting for the detection efficiency for the reaction ^{21}N(p,pn)^{20}N*$\rightarrow^{19}$N+n in a CH$_2$ target in quasi-free scattering conditions.
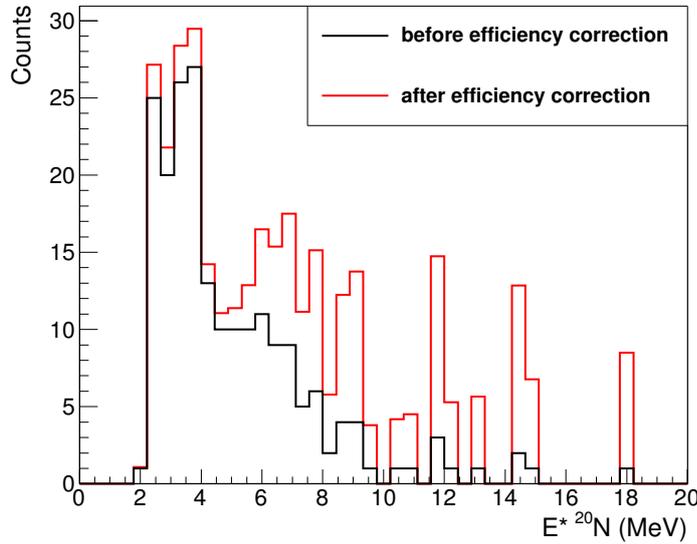
Figure 6.23: Example of the efficiency correction for the excitation energy of ^{20}N in a CH$_2$ target. The black curve is the excitation energy before efficiency correction, the red curve is the result of the correction.
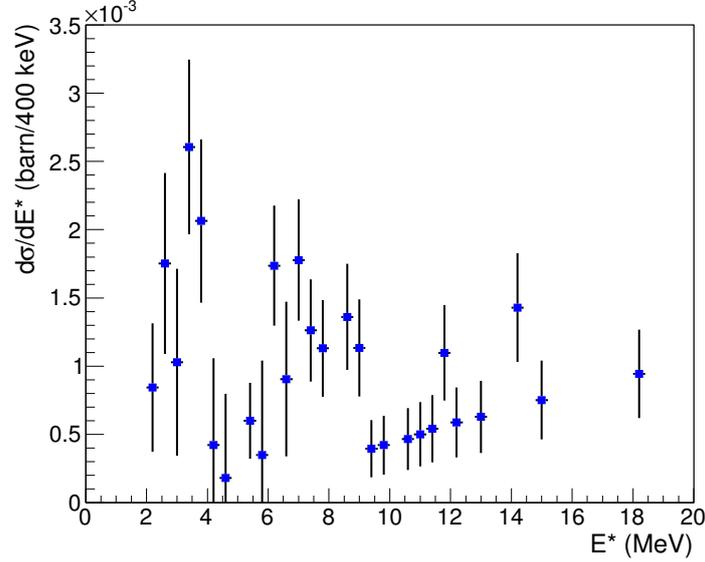
Figure 6.24: Excitation energy distribution after efficiency correction of ^{20}N reconstructed for the proton target. The neutron separation energy is 2.161 MeV.

As we are interested in the quasi-free scattering reactions which occur with the protons in the target, the contribution from the carbon and empty target need to be subtracted. In figure 6.24 is shown the excitation energy spectrum for the reconstructed hydrogen target. The cross section obtained for the neutron break-up channel is (27.08 ± 5.00) mb. The spectra begins above 2.161 MeV, the neutron separation energy for the ^{20}N. Despite the high uncertainty due to the lack of the statistics, two peaks are observed. In order to check it, we have performed a set of minimizations including two Breit-Wigner functions and a background function. The Breit-Wigner functions were characterized by their width (Γ) and peak position (E_r), as follows

$$f(E; E_r, \Gamma) = \frac{\Gamma}{(E - E_r)^2 + \Gamma^2/4} \tag{6.7}$$

The background function was chosen as the product of an error and an exponential function,

$$f(E) = a \times erf(bE) \times e^{-cE} \tag{6.8}$$

The combination of the Breit-Wigner and background functions was convoluted with the experimental response obtained via LEG simulation. Then

a minimization was performed, obtained as a result (pink curve) the plot shown in figure 6.25. The grey distribution is the combination of the two Breit-Wigner and the background functions previous to the experimental response filter. The first resonance was found to be at 3.2±0.3 MeV with a width Γ of $0.96^{+0.5}_{-0.4}$ MeV. The second resonance is at $6.77^{+0.4}_{-0.3}$ MeV. Its width have a very high uncertainty. According to [18], it has been observed a γ ray with an energy of 2.1 MeV which corresponds to a decay from an state of 2.943 MeV in the continuum. Our first resonance is in agreement with the reported energy value. Regarding to the second resonance, shell model calculations are needed in order to extract some conclusion.
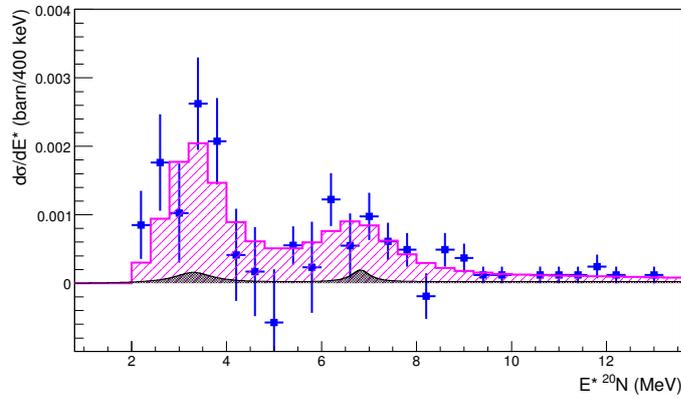
Figure 6.25: Excitation energy spectrum of the unbound states in ^{20}N. The experimental points are shown as blue points, while the result of the minimization is the pink histogram. The black function corresponds to the original resonances and the background functions, previous to the experimental response filter. Two resonances are observed at 3.2±0.3 and 6.77±0.4 MeV.

Chapter 7

Discussion of the results

After the description of the analysis methods and their application to a particular case, this chapter will be devoted to the interpretation and evaluation of the results.

The first part of this chapter will focus on the discussion of the results for the inclusive cross sections in the (p,pn) and (p,2p) reactions for the projectiles ^{21}N, ^{23}O and ^{22}O. Next, the results for the respective momentum distributions and γ ray emission will be discussed. The last part will be devoted to the discussion of the one neutron break-up channels: ^{21}N(p,pn)^{20}N$^* \rightarrow^{19}$N+n, ^{23}O(p,pn)^{22}O$^* \rightarrow^{21}$O+n and ^{22}O(p,pn)^{21}O$^* \rightarrow^{20}$O+n.

7.1 Inclusive cross sections

This section summarizes the results for the cross sections associated to the (p,pn) and (p,2p) channels of the projectiles ^{21}N, ^{23}O and ^{22}O. The results are shown in table 7.1. It is observed that the cross section for the reaction channel (p,pn) is larger than that of (p,2p) for a given projectile. This is due to various reasons: all the projectiles are neutron-rich nuclei and, therefore, there are more neutrons than protons available for reactions. Also, the neutron $0d_{5/2}$ shell is almost full in the cases under study, giving rise to a large value of the spectroscopic factors for the neutrons removed from this shell. Moreover, the binding energy of the outermost neutrons is smaller than that of the protons, thus favouring the neutron removal process. Another important difference relies on the underlying NN interaction involved in each case. Under quasi-free scattering conditions, the (p,2p) and (p,pn) processes are mainly induced by the pp and pn interactions. These two interactions are very different in nature and hence one expects differences in the corresponding knockout cross sections. Between 400 MeV and 500 MeV, the

np interaction cross section is larger than that of pp [78]. Most important, however, is the fact that the pp scattering is only allowed for isospin T = 1, while for np scattering isospin T = 0 and T = 1 are permitted with equal weight, with the T = 0 giving the dominant contribution.

From this discussion, it is clear that a reliable prediction of the quasi-free scattering cross sections requires the use of a realistic NN interaction. In the standard DWIA approach [79], traditionally used in the analysis of quasi-free scattering experiments with stable beams, the scattering amplitude (whose square provides the differential cross section) can be expressed as a product of a realistic NN transition amplitude times some kinematical factors. In more sophisticated reaction frameworks, such a factorization is not possible but, still, a key basic ingredient is the NN transition amplitude, such as in the AGS/Faddeev approach [80, 81] or, equivalently, a realistic NN interaction, as it is done in the transfer to the continuum approach [82, 83]. Preliminary calculations performed with the latter method for some of the reactions studied in this work, confirm the dominance of the (p,pn) cross sections over the (p,2p) cross sections [84].

E_{beam} (MeV/u)	Reaction	σ(mb)
417	^{21}N(p,pn)^{20}N	43.1±9.0
	^{21}N(p,2p)^{20}C	2.08±0.49
445	^{23}O(p,pn)^{22}O	63±17
	^{23}O(p,2p)^{22}N	5.4±1.3
414	^{22}O(p,pn)^{21}O	36.1±7.2
	^{22}O(p,2p)^{21}N	5.28±0.58

Table 7.1: Inclusive cross sections for the (p,pn) and (p,2p) reactions for the projectiles ^{21}N, ^{23}O and ^{22}O, corrected for the Crystal Ball efficiency in a proton target.

Figure 7.1 shows the total inclusive cross sections for the (p,pn) (left) and (p,2p) (right) as a function of the neutron and proton number of the projectile, respectively. It is observed for the (p,pn) channels that the cross section is larger for N = 15 than for N = 14. This can be understood in terms of the shell model: N=14 can be interpreted as a closed sub-shell with the level $0d_{5/2}$ completely full, holding six neutrons, while the N = 15 has a single neutron in the $1s_{1/2}$ shell. This magicity of the N = 14 was already

observed in previous works [17, 18, 19].

The valence protons of these projectiles all reside in the same shell. The oxygen isotopes have the two least bound protons saturating the $0p_{1/2}$ shell, the nitrogen having one proton less in the same shell. It is more probable to remove a proton from the oxygens because of the higher occupancy.
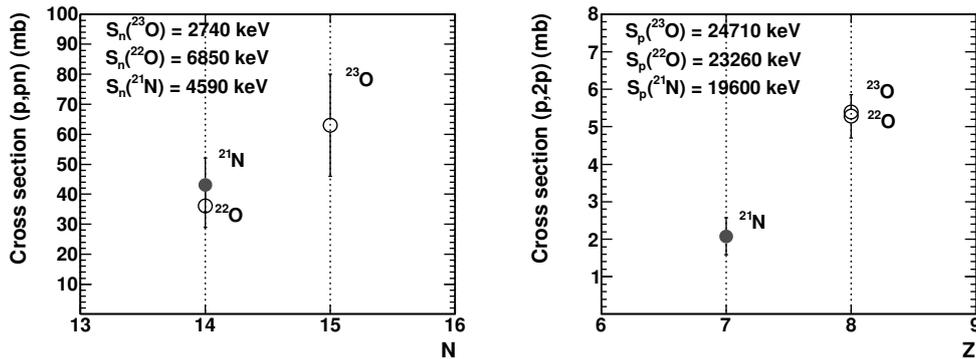
Figure 7.1: Left: cross section for the (p,pn) channel as a function of the neutron number for the projectiles ^{21}N and ^{23,22}O. Right: cross section for the (p,2p) channel as a function of the proton number for the projectiles ^{21}N, ^{23,22}O. In both cases, the one neutron (proton) separation energy for each projectile is included in the plot, taken from http://ie.lbl.gov/toi2003/MassSearch.asp.

7.2 Momentum distributions

The width and shape of the momentum distribution contains information about the structure of the projectiles. In Appendix C, all the plots showing the longitudinal and transversal momentum distributions of the fragments are included, for the reactions previously described. The experimental setup has a better resolution for the momentum transversal component than for the longitudinal one. Thus, the discussion will be based on the results extracted for this component.

In order to obtain a reliable value for the full width at half maximum (FWHM), this was studied as a function of the number of bins and bin offsets. It was observed that the FWHM is higher for a relative low number of bins (affected by the bin width itself), then decreases with an increase of the bin number, until this stabilizes. When the number of bins is too high, statistical fluctuations appear, making the FWHM oscillate from one histogram

granularity to the next. With the purpose of obtaining an absolute value, the distribution of the FWHM given by the different histograms representation was studied, characterized by its mean and RMS values.

In table 7.2 and figure 7.2 the results obtained for the transversal momentum distributions for all different channels are presented. The given FWHM values were corrected by the full width at half maximum of the unreacted beam without target FWHM (as shown in equation 6.2).

Reaction	FWHM (MeV/c)
^{21}N(p,pn)^{20}N	190±33
^{21}N(p,2p)^{20}C	204±41
^{23}O(p,pn)^{22}O	108±25
^{23}O(p,2p)^{22}N	95±51
^{22}O(p,pn)^{21}O	240±16
^{22}O(p,2p)^{21}N	254±12

Table 7.2: Transversal momentum distribution FWHM for the (p,pn) and (p,2p) reactions for the projectiles ^{21}N, ^{23}O and ^{22}O.
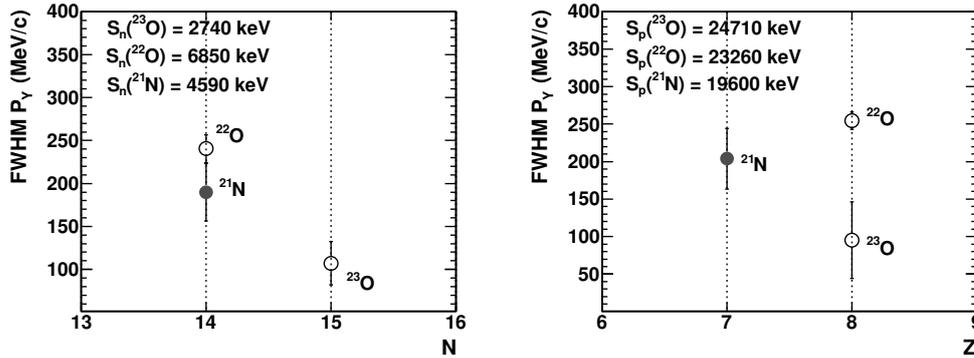
Figure 7.2: Left: FWHM of the transversal momentum distribution for the (p,pn) channel are represented as a function of the neutron number for the projectiles ^{21}N and ^{22,23}O. Right: same, but for the (p,2p) channel represented as a function of the proton number.

For the two oxygen isotopes, it is observed that the momentum FWHM decreases with the increasing of the neutron number. This is explained in

the shell model context. The N=14 valence neutrons are in the $0d_{5/2}$ shell, while the single valence neutron for N=15 is in the $1s_{1/2}$. This change from the d shell (angular momentum l=2) to the s shell (angular momentum l=0) explains the narrowing in the momentum distributions. In the (p,2p) channels if we focus on the N=14 shell, it is observed that the FWHM for the ^{22}O is bigger than the one for the ^{21}N. The reason is that the oxygen isotope has its valence sub-shell completely full, rendering the nucleus tightly bound and so more compact, which translates into a wider momentum distribution. An accurate comparison between the two oxygen isotopes is limited by the lack of statistics and does not allow to extract any conclusions, since the ^{23}O has very low statistics for the (p,2p) channel. Despite this, is observed a very narrow distribution compared with the ^{22}O.

This behaviour for the neutron shells of these N=14 nuclei was already observed in previous works [85, 86] where the experimental observations support the existence of a sub-shell for N=14.

In order to investigate the angular momentum of the projectile's shell where the nucleon was removed, theoretical calculations have been performed. First calculations were performed for the reaction ^{21}N(p,pn)^{20}N by using the Distorted Wave Impulse Approximation (DWIA) theory and eikonal wave functions by C. Bertulani. The theoretical formulation includes multiple scattering based on medium modified NN (nucleon-nucleon) cross sections [87].

The ^{21}N structure can be described as a combination of the ^{20}N in its ground state with a neutron in the $0d_{5/2}$ and the ^{20}N in an excited state 1^- with a neutron in an $1s_{1/2}$, each coupled to produce the ^{21}N ground state spin and parity $1/2^-$. The configuration will be as follows

$$\left|^{21}N(gs)\right\rangle_{1/2^-} = a \cdot [\left|^{20}N(2^-)\right\rangle \otimes \left|0d_{5/2}\right\rangle] + b \cdot [\left|^{20}N(1^-)\right\rangle \otimes \left|1s_{1/2}\right\rangle] \quad (7.1)$$

Figure 7.3 shows transversal components for the d and s waves calculated by the theory using the mentioned approaches. To calculate the weight of each wave function a Pearson χ^2 on the experimental data was performed. Figure 7.4 shows the result. The weights obtained for the $0d_{5/2}$ and $1s_{1/2}$ are 0.91 ± 0.18 and 0.09 ± 0.18. From the fit it is observed that the main contribution to the ^{21}N ground state is due to the ^{20}N(2^-) coupling with the neutron in the $d_{5/2}$.

The few-body Faddeev/Alt-Grassberger-Sandhas (Faddeev/AGS) reaction framework [80, 88] can be viewed as a multiple scattering expansion in terms of the transition amplitude of each interacting pair. Calculations were made by R. Crespo, E. Cravo and A. Deltuva [89], for the reaction ^{22}O(p,pn)^{21}O, assuming that the ^{22}O can be well described as an inert core
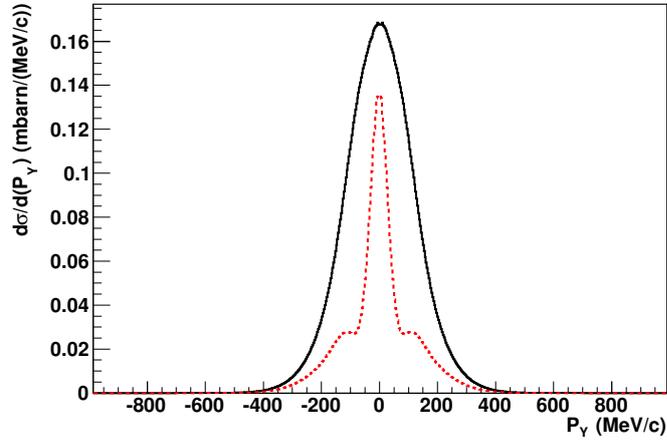
Figure 7.3: Transversal momentum distribution extracted from the contribution of different neutron states for the $0d_{5/2}$ (solid black line) and $1s_{1/2}$ (dashed red line) waves following the approximations from [87], courtesy of C. Bertulani.
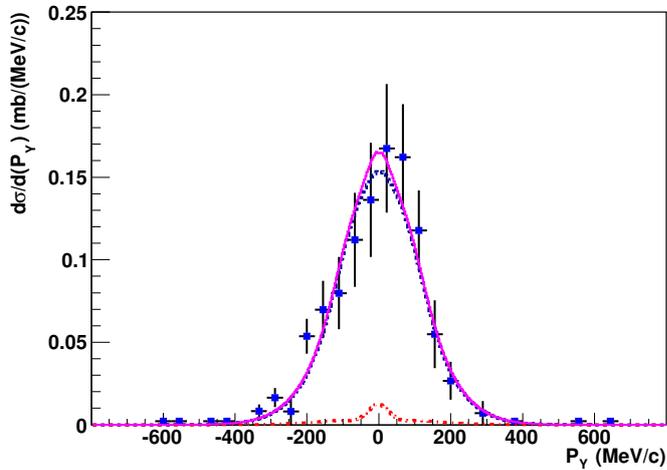
Figure 7.4: Results for the comparison of the experimental transversal momentum obtained in this work for the reaction channel ^{21}N(p,pn)^{20}N (points) compared with the theoretical transversal momentum obtained in the approximation [87] and scaled by their corresponding factors obtained by the a Pearson χ^2 method.

of ^{21}O and a valence neutron. The ^{22}O ground state could be in principle be described as

$$\left|^{22}O(gs)\right\rangle_{0^+} = a\cdot[\left|^{21}O(gs)\right\rangle_{5/2^+}\otimes\left|0d_{5/2}\right\rangle]+b\cdot[\left|^{21}O(exc)\right\rangle_{1/2^+}\otimes\left|1s_{1/2}\right\rangle] \quad (7.2)$$

Taking the core in the $5/2^+$ ground state the theoretical calculations have shown that contributions beyond the single scattering term where the proton scatters from the valence neutron are very significant and reduce the momentum distributions by about 50%. It was also found that the contribution of the wave function were the core is the $1/2^+$ excited state is also sizable.

As before, a Pearson χ^2 minimization has been performed comparing the shape given by the theoretical approach and the experimental one. The results, in figure 7.5, show clearly that the d shell contribution from the theory (solid blue line) is not enough to reproduce the experimental momentum distribution obtained in this work. Excluding the four central points, a much better fit is obtained (dashed pink line). This makes even more evident that the contribution from the s wave is not negligible. The function where the core is the $1/2^+$ excited state is under study.
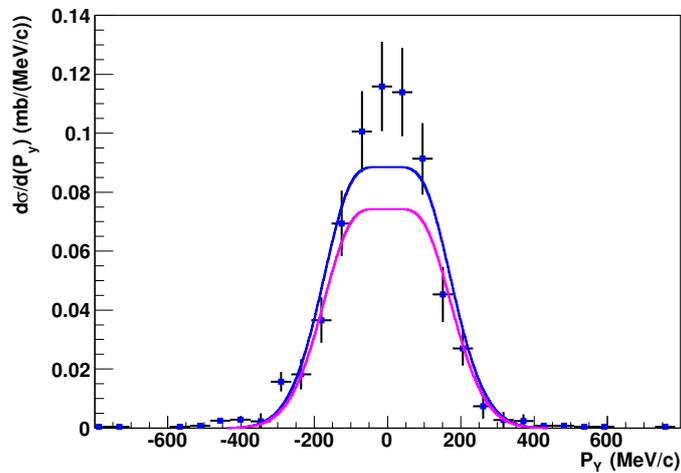
Figure 7.5: Experimental transversal momentum distribution obtained in this work for the reaction channel $^{22}O(p,pn)^{21}O$ (points) compared with the theoretical transversal momentum obtained in the few-body Faddeev approximation. The solid blue line is the result for the minimization including all the experimental points, the dashed pink line is the result of excluding the four points in the middle.

7.3 γ rays

The Crystal Ball detector was used to measure the deexcitation γ rays in coincidence with the outgoing fragments for the following quasi-free scattering channels: ^{21}N(p,pn)^{20}N, ^{21}N(p,2p)^{20}C, ^{23}O(p,pn)^{22}O, ^{23}O(p,2p)^{22}N, ^{22}O(p,pn)^{21}O and ^{22}O(p,2p)^{21}N. Due to statistical reasons and to the complexity of some spectra, we have focused our study on the γ ray spectra of the nuclei ^{22}O, ^{21}N and ^{21}O. For these cases it was possible to extract the relative intensities of the emitted γ rays. In order to find the relative intensities, we have performed a set of simulations in R3BRoot, obtaining the complete response of the calorimeter in efficiency and resolution to a given energy emission. The γ-ray energies have been taken from the literature where accurate determination of the decay schemes were available. The atomic background is represented as an exponential function, taking particular care to apply this function in regions where no γ ray was expected. Other background determination was tested, in particular studying the gamma ray spectra of ^{16}O, where the situation of the lowest excited state, located at 6.05±0.01 MeV, forbids the emission of a low energy γ. An appropriate scaling of the ^{16}O spectrum, taking into account the number of reactions, leads to a very small background correction, and therefore will not be used herein. In any case, the test served to confirm the simple exponential shape of the background above a given energy threshold.

In order to compare the simulation with the experimental data, we have minimized via the Pearson χ^2 method the distance between the experimental and the simulated peaks, scaled by factors which will be used to determine the relative γ-ray intensities. To ensure that this determination is completely robust, the minimization has been performed for a set of energy thresholds (100, 200, 300 and 400 keV) and number of histogram bins (20-50), characterizing the probability distribution function of gamma intensities resulting from each minimization. From the results of this probability function, estimates and uncertainties of the gamma intensities could be obtained on solid grounds.

The first spectrum that will be discussed has been obtained in coincidence with the fragments from the reaction ^{23}O(p,pn)^{22}O. Based on the level scheme of the ^{22}O, taken from [17, 85], this isotope has three dominant γ rays in cascade, with energies: 1383 keV, 2354 keV and 3199 keV. ^{23}O ground state can be described as the combination of the wave function of a nucleon in the $0d_{5/2}$ shell or in the $1s_{1/2}$ shell coupled to the ^{22}O core. According to references [17, 85], the ground state of ^{23}O has spin and parity $1/2^+$. The ground state of ^{22}O is a 0^+ and the excited states are 2^+, 3^+ and $(0^-,1^-)$. This last state is not observed in the reference [17]. According to the spin

^{22}O	E_x^{th} (keV)	E_x^{exp} (keV)	C^2S, $1s_{1/2}$	C^2S, $0d_{5/2}$	C^2S, $0d_{3/2}$
0^+	g.s.	g.s.	0.796	-	-
2^+	3374	3199	-	2.076	0.053
0^+	4613	4909	0.115		-
3^+	4829	4582	-	3.079	-
2^+	6502	6509	-	0.237	0.0049
3^+	8317	-	-	0.164	-

Table 7.3: Spectroscopic factors for different core + neutron coupling obtained from shell model calculations. The first column shows the spin and parity of the ^{22}O core states. The second and third columns show the theoretical [84] and experimental [17] energies of the states listed in the first column, respectively. The last three columns show the spectroscopic factors (occupancies) for the different core + neutron coupling possibilities calculated with OXBASH [90] using the WBT interaction.

and parity and shell model calculations shown in table 7.3 using the WBT interaction [84], only the coupling of the ^{22}O ground state to a neutron in $1s_{1/2}$ or the excited states 3^+ at 4582 keV and 2^+ at 3199 keV to a neutron in $0d_{5/2}$ could be observed.

In order to calculate the relative intensity for each γ ray, we have tried to minimized the difference between the experimental points and a simulation curve including the two γ rays with energies of 1383 and 3199 keV and an exponential function representing the background. The experimental spectrum showed a clear indication that the peak, originally assigned to 3199 keV, appears at lower energy, probably due to energy losses not correctly evaluated in the Crystal Ball detector simulation for gammas of high energy. We have performed two different studies of the spectrum for this nucleus: the first including a contribution at 3199 keV and the second replacing it by the response to a lower energy, 2900 keV, to compensate for the unaccounted losses. The last one produces a much better χ^2 and the results of this second analysis provide intensities which are in better agreement with the ones from [17]. The experimental γ ray spectrum (black points) together with the result for the minimization performed (solid red line) for this second analysis are shown in figure 7.6.

The relative intensities for each γ ray are shown in table 7.4. The obtained results are compatible with the literature [17, 85]. In both articles the most
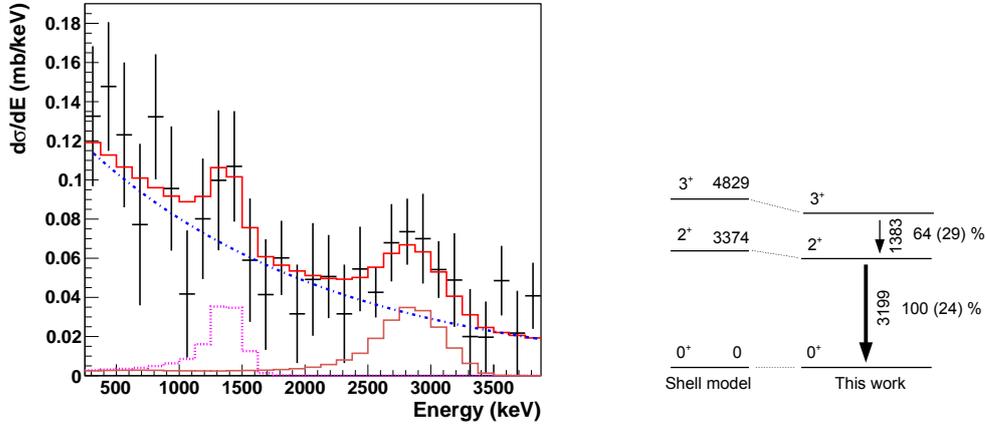
Figure 7.6: Left: experimental γ ray spectra (black markers) and best minimization (red histogram line) for ^{22}O. The individual contributions of each gamma are shown, according to the simulated response of the Crystal Ball detector to each monoenergetic gamma emission. Right: level scheme used in this work showing the energies and relative intensities together with their uncertainties for the gamma rays. Shell model calculations by A. Moro [84].

energetic γ was found to be the most intense, corresponding to the decay of the first excited state 2^+. According to [17] the lowest energetic γ transition has a relative intensity of 43 ± 8 %, being in a reasonable agreement with our calculation of 60 ± 29 %.

	Results from this work	Results from [17]
E_γ (keV)	I_γ (%)	I_γ (%)
1383	60 $\pm$29	43 $\pm$8
3199	100 $\pm$24	100 $\pm$15

Table 7.4: Relative intensities determined for the gamma rays of ^{22}O, using the simulated energies of 2900 and 1383 keV.

The γ ray spectrum corresponding to ^{21}N was also studied, from the gamma coincidences with the fragments from the reaction ^{22}O(p,2p)^{21}N. According to reference [18], this nucleus has a γ ray at 1177 keV, with the strongest intensity. This transition is in coincidence with the energies at 1228, 2142, 2438, 1790 and 884 keV (see figure 7.8). All the information
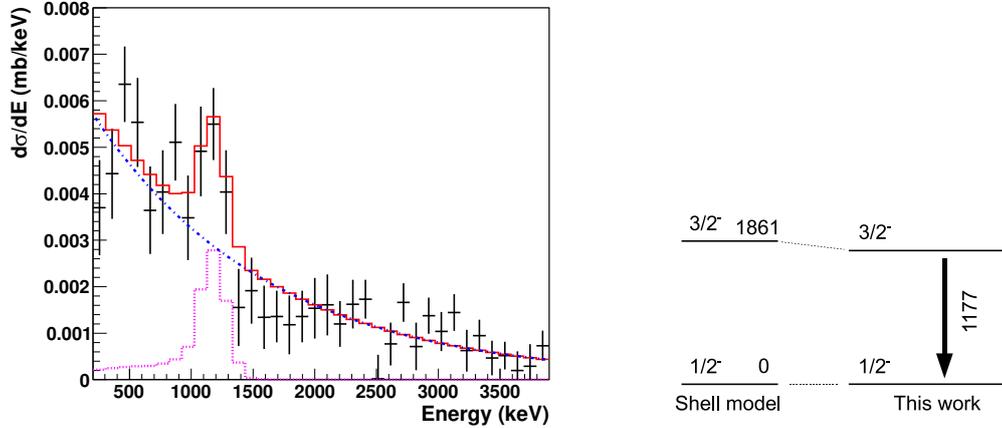
Figure 7.7: Left: experimental γ ray spectra (black) and best minimization (red) for ^{21}N. Right: level scheme used in this work showing the energy and relative intensity for the existent gamma ray. Shell model calculations taken from [84].

about the spin and parity of the different states has been taken from [18]. As it was done in the previous case, the ^{22}O can be described as a core of ^{21}N coupled to a proton in the $0p_{1/2}$ or $0p_{3/2}$ shells. Taking into account the spin and parity of the ground and excited states of ^{21}N, we expect to observe only the γ ray corresponding to the first excited state at 1177 keV ($3/2^-$). Then, we first try to interpret the experimental data from the minimization of this unique contribution, additionally to the exponential background. The result can be found in figure 7.7; no additional gamma contribution was found to be necessary to interpret the experimental decay scheme. The exclusive cross section obtained for the state at 1177 keV was found to be (1.1±0.1) mb.

The last spectrum presented in detail here is the corresponding to the ^{21}O. The decay scheme has been studied previously [17]. According to this reference there are four branches. Two of them are composed by one gamma with energies of 1218 and 3026 keV respectively. The remaining two branches are formed by two γ rays, namely 2133 + 881 keV and 3073 + 1854 keV. ^{22}O ground state can be described as a nucleon occupying either the shell $0d_{5/2}$ or the shell $1s_{1/2}$, coupled to ^{21}O core. According to reference [17] the ground and excited states of ^{21}O have spin and parity $5/2^+$, $1/2^+$, $3/2^+$, $7/2^+$ and $9/2^+$ (see figure 7.8). So, the combinations that are possible to describe the ^{22}O in its ground state would be mainly the ground state of ^{21}O which has spin and parity $5/2^+$ and the first excited state $1/2^+$. There are other states, at higher energies, for example the $5/2^+$ at around 3000 keV, but according

Figure 7.8: Left: level scheme for ^{21}N proposed in the reference [18]. Right: level scheme for ^{21}O proposed in the reference [17].

to shell model calculations using the WBT interaction [84] the probability to populate this state is very low. The spectroscopic factor for this state is 0.12, while the spectroscopic factor of the ground state is 4.79. In principle it would be possible to produce other excited states via processes like dynamic excitation of the core, but the dynamic excitation requires an exchange of energy which should be not compatible with the conditions of the quasi-free scattering selected in the analysis.

Taking into account all this information, the initial attempts were performed with a single gamma emission at an energy of 1218 keV. The result of the minimization is shown in figure 7.9. The exclusive cross section obtained for the state at 1218 keV was found to be (0.4 ± 0.2) mb.

The ^{20}N has a very complicated spectra to be analysed with the Crystal Ball detector, because it has four γ rays (615, 843, 944 and 1052 keV) in an energy range relatively small, making it difficult to distinguish the contributions due to the detector's limited resolution (around 20% for a γ ray with an energy of 1 MeV). However, a minimization was performed using the relative intensities and energies from the literature [18]. Our results are compatible with these relative intensities set from [18], but different parameter combinations produce similar χ^2 values, resulting in very different relative intensities which makes it impossible to extract accurate information from

Figure 7.9: Left: experimental γ ray spectra (black) and best minimization result (red) for ^{21}O. Right: level scheme used in this work showing the energy and relative intensity for the existent gamma ray. Shell model calculations by A. Moro [84]

this spectrum. The lack of statistics for the most exotic available nuclei, ^{20}C and ^{22}N, do not allowed us to perform a detailed study.

7.4 The breakup channels

In a similar approach to the analysis of the unbound states for the one neutron breakup channel of the projectile ^{21}N, the excitation energy spectra for the reaction channels ^{23}O(p,pn)^{22}O$^* \rightarrow ^{21}$O+n and ^{22}O(p,pn)^{21}O$^* \rightarrow ^{20}$O+n were investigated. The excitation energies for the nuclei ^{22}O and ^{21}O were reconstructed by measuring the coincidence between the breakup reaction fragments ^{21}O and ^{20}O and their respective emitted neutrons in quasi-free scattering conditions. The cross sections for these two channels were determined by subtracting from those obtained for the CH$_2$, the carbon and empty target contributions. The values obtained are (14.7$\pm$6.9) mb for the ^{23}O(p,pn)^{22}O$^* \rightarrow ^{21}$O+n and a cross section of (13.9$\pm$3.3) mb for the channel ^{22}O(p,pn)^{21}O$^* \rightarrow ^{20}$O+n. The excitation energy spectra, corrected by the efficiency of detecting one neutron in the LAND detector, are shown in figure 7.10 for the two studied cases. The possibility of emitting a neutron for the ^{22}O begins when the energy is above 6.85 MeV (left), while for the ^{21}O this channel opens for energies above 3.806 MeV (right)[1].

---

[1]Separation energies taken from http://ie.lbl.gov/toi2003/MassSearch.asp
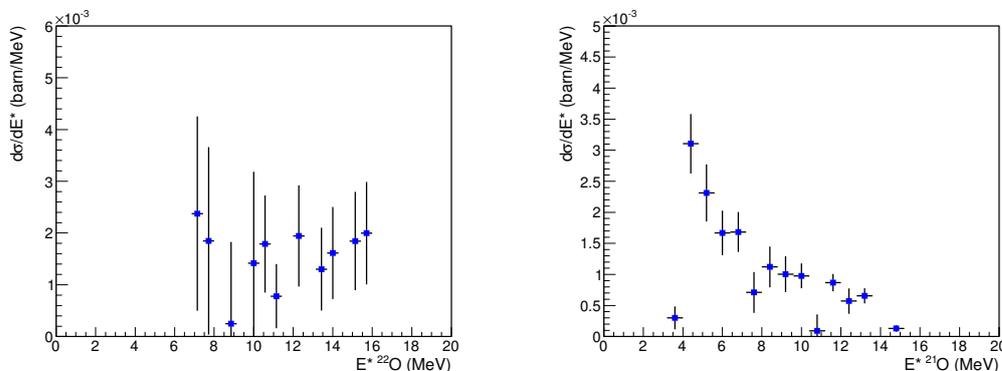
Figure 7.10: Excitation energy distribution for the ^{22}O (left) and ^{21}O (right) reconstructed for the neutron decay channel. The one-neutron separation energies are 6.850 and 3.806 MeV for the ^{22}O and ^{21}O, respectively

The excitation energy distribution for the ^{21}O can be compared with previous results measured by B. Fernández-Domínguez et al. [91]. In this work they investigated the spectroscopy of ^{21}O using transfer reactions in inverse kinematics at the SPIRAL facility in GANIL. They observed two resonances, one at 4.77±0.10 and the other one 6.17±0.11 MeV.
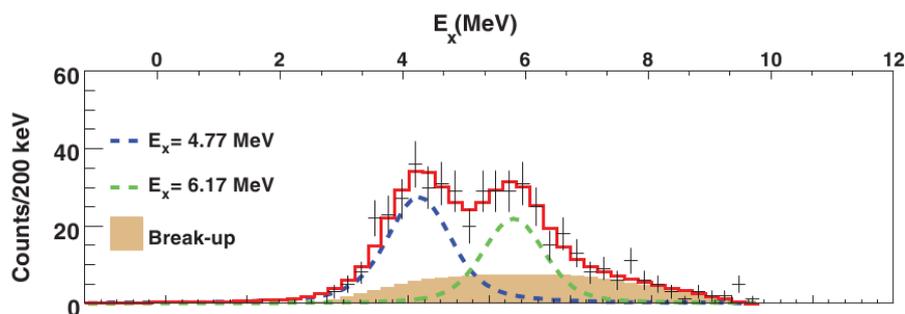
Figure 7.11: Excitation energy for the unbound states for ^{21}O obtained by B. Fernández-Domínguez et al. [91].

From the observation of the obtained excitation energy for ^{21}O, it seems evident the presence of three structures that could correspond to three separate resonances. In order to check it, we have performed a set of minimizations following the procedures described for the analysis of the excitation energy spectrum of ^{20}N (see Section 6.3). The positions of the three resonances according to the minimization are: 4.41±0.07 MeV, 5.52±0.10 MeV and 6.74±0.50 MeV. In the case of the first resonance we provide a width of $\Gamma = 0.280 \pm 0.140$ MeV. For the other two resonances we are only able to give

a superior limit of 0.300 and 0.450 MeV, respectively. The result obtained for the first resonance are close to the previous value obtained by [91].
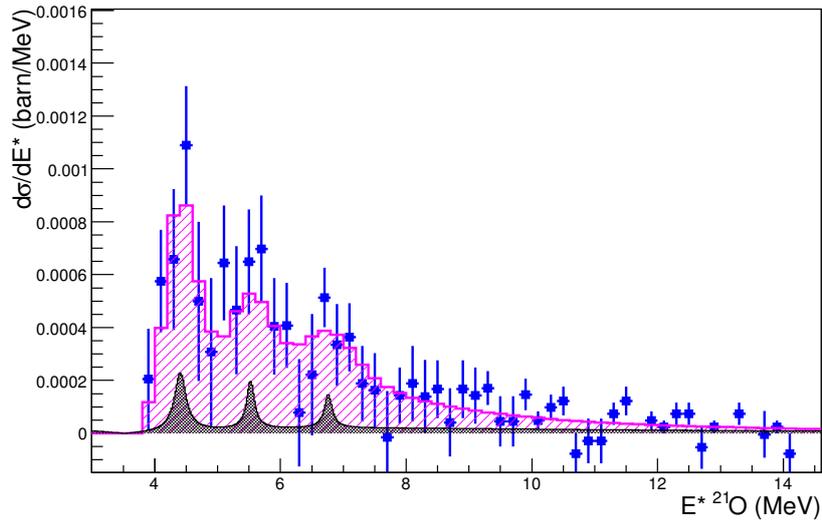
Figure 7.12: Excitation energy for the unbound states for ^{21}O. The points correspond to the experimental data, the pink curve is the simulated response of the excitation function included in black (see text for details).

The excitation energy distribution for the ^{22}O presents very low statistics to perform a detailed analysis of the resonances. But, the fact that the spectrum starts directly above the threshold could be an indicative of a resonance at an energy very close to the neutron emission threshold. In [92] the structure of ^{22}O was investigated by measuring the β decay of ^{22}N in an experiment performed at the National Superconducting Cyclotron Laboratory (NSCL). According to [92] the first state above the neutron emission threshold is at 7.65 MeV. This state seems to be compatible with our observation.

Chapter 8

Conclusions

Light neutron-rich nuclei around N=14 (^{23}O, ^{22}O and ^{21}N) have been for the first time investigated via quasi-free scattering (p,2p) and (p,pn) reactions with a view to study the proton and neutron shells, respectively.

The S393 experiment was performed at GSI in 2010, employing six different settings centred on different A/Q ratios. The setup was placed at the LAND-R^{3}B experimental area at Cave C. An ^{40}Ar primary beam was accelerated in the SchwerIonenSynchrotron (SIS-18) up to an energy of about 490 AMeV. The beam was then directed to the FRagment Separator area (FRS) where, using a beryllium production target, a secondary beam produced via fragmentation was selected depending on the A/Q ratio of the desired species. Following this selection, the isotopes of interest were guided to Cave C, where the reaction target and the detectors needed for the analysis were located.

Two key observables have been studied with the aim of shedding light upon the structure of these nuclei. The inclusive cross sections and transversal momentum distributions for the (p,pn) channels reveal a change in the structure of these nuclei when we move from the N $= 14$ to the N $= 15$, i.e., from the $0d_{5/2}$ shell to the $1s_{1/2}$. For the (p,2p) reactions, the measurement of the same observables allowed the same study for the $0p_{3/2}$, $0p_{1/2}$ proton sub-shells. The comparison of the experimental data with the theoretical calculations allowed to extract spectroscopic information of the neutron shells in the projectiles ^{21}N and ^{22}O.

The results obtained for the cross sections are shown in table 8.1. It is observed that the inclusive cross sections obtained for the (p,pn) channels are higher than the ones obtained for the (p,2p). This is due to various reasons: there are more neutrons than protons available for the quasi-free scattering. The spectroscopic factors for the neutrons removed from the $0d_{5/2}$ are larger because the shell is almost filled in the cases under study. Moreover, the binding energy of the outermost neutrons is smaller than the

one for the protons making easier to remove a neutron. In the region between 400 MeV and 500 MeV, the n-p interaction cross section is bigger than the p-p contributing to the increasing of the (p,pn) channels cross section. But, the most important is the fact that in the (p,2p) reactions, the two particles in the final state are identical allowing only the T = 1 configuration. Nevertheless, in the (p,pn) reactions the T = 0 and T = 1 are allowed, having the first one a cross section several times larger than the second one. It was observed, for the neutron shells, that the ^{23}O has the higher cross section. This could be explained by its lower separation energy. Also, the other two nuclei (^{22}O and ^{21}N) have the valence neutrons in a closed shell. For the (p,2p) channels it was observed that the nuclei with Z = 8 have the same cross section because they have the same number of protons in the same shell. They have a higher cross section than the ^{21}N due to the larger number of valence protons to be knocked-out.

Reaction	σ(mb)
^{21}N(p,pn)^{20}N	43.1±9.0
^{21}N(p,2p)^{20}C	2.08±0.49
^{23}O(p,pn)^{22}O	63±17
^{23}O(p,2p)^{22}N	5.4±1.3
^{22}O(p,pn)^{21}O	36.1±7.2
^{22}O(p,2p)^{21}N	5.28±0.58

Table 8.1: Inclusive cross sections for the (p,pn) and (p,2p) reactions for the projectiles ^{21}N, ^{23}O and ^{22}O.

Regarding the momentum distributions, it was observed for the (p,pn) channels that the FWHM decreases when moving from N = 14 to N = 15; this can be interpreted as neutrons passing from a d-shell with angular momentum l = 2 to an s-shell with angular momentum l = 0, which has a narrower momentum distribution and a wider spatial distribution. The measured FWHM are found in table 8.2. From the comparison with theoretical calculations, it was possible to obtain the weights for the different waves. In the case of the ^{21}N nucleus, a contribution of 0.91±0.18 and 0.09±0.18 for the d and s waves, respectively has been measured. For the ^{22}O, it has been observed that the composition of the ground state requires some strength of the s wave, coupled with the first excited state of ^{21}O. The (p,2p) channels

were also investigated, obtaining the FWHM shown in table 8.2. From the comparison of the FWHM for the two oxygen isotopes, it is observed that the ^{23}O has a narrower momentum distribution because it has a larger separation energy.

Reaction	FWHM (MeV/c)
^{21}N(p,pn)^{20}N	190±33
^{21}N(p,2p)^{20}C	204±41
^{23}O(p,pn)^{22}O	108±25
^{23}O(p,2p)^{22}N	95±51
^{22}O(p,pn)^{21}O	240±16
^{22}O(p,2p)^{21}N	254±12

Table 8.2: Transversal momentum distribution FWHM for the (p,pn) and (p,2p) reactions for the projectiles ^{21}N, ^{23}O and ^{22}O.

The γ ray spectra for the nuclei ^{22}O, ^{21}N, ^{21}O and ^{20}N were studied by measuring the coincidence of these isotopes with the gamma rays measured in the Crystal Ball detector. For ^{22}O, ^{21}N and ^{21}O cases, the gamma rays relative intensities or exclusive cross sections were determined. It was found via the observation of the γ rays with energies of 3199 and 1383 keV, that ^{23}O could be described as the combination of an ^{22}O core in its ground state coupled to a neutron in the $0s_{1/2}$, an ^{22}O core in its first excited state (3199 keV) 2^+ coupled to a neutron in the $0d_{5/2}$ and an ^{22}O core in its second excited state (4582 keV) 3^+ coupled to a neutron in the $0d_{5/2}$. The calculated relative intensities were found to be in good agreement with previous results from [17, 85]. The study of the ^{21}N γ ray spectrum revealed that the ground state of the ^{22}O can be described as a combination of the ^{21}N core either in its ground state (spin and parity $1/2^-$) coupled to a proton in the $0p_{1/2}$ or in its first excited state $3/2^-$, where will emit a γ ray with an energy of 1177 keV. The exclusive cross section for the excited stated at 1177 keV was found to be (1.7±0.4) mb. The neutron shells for the ^{22}O were studied via the γ ray spectrum of ^{21}O. ^{22}O ground state can be described as a nucleon occupying either the shell $0d_{5/2}$ or the shell $1s_{1/2}$, coupled to the ground state of ^{21}O or to the first excited state at 1218 keV, respectively. The exclusive cross section for the first excited state was found to be $(0.85^{+0.97}_{-0.85})$ mb.

The study of the excitation energy spectra allowed the determination of

three resonances for the unbound states of ^{21}O. The resonances are found to be at 4.41±0.07 MeV, 5.52±0.10 MeV and 6.74±0.50 MeV, being the width of the first resonance 0.280±0.140 MeV. The energy obtained for the first resonance is close to a previous value obtained by [91]. The study of the excitation energy spectrum for the ^{20}N revealed the existence of two resonances at 3.2±0.2 MeV and 6.77±0.4 MeV. The first one is compatible with the result found by [18] where they measured a state in the continuum at 2.943 MeV. Despite the lower statistics in the case of the excitation energy spectrum for ^{22}O, the fact that the spectrum rises steeply just above the one neutron separation energy could be an indication of the existence of a resonance around 7.5 MeV.

Chapter 9

Resumen

Las primeras investigaciones en física nuclear comenzaron en 1911 cuando Ernest Rutherford descubrió que cada átomo contenía un núcleo cargado positivamente [1]. Los núcleos pueden caracterizarse por su número de protones (Z) y por su número de neutrones (N). Para un determinado elemento (un Z) pueden existir varios isótopos (distinto N). Desde el decubrimiento del núcleo, más de 2800 isótopos han sido identificados y se ha predecido que existen más de 7000 que vivirían el tiempo suficiente para ser observados [2]. En la figura 9.1 se muestran los núcleos conocidos, representando su número de protones frente a su número de neutrones. Los isótopos estables aparecen dentro de celdas negras, mientras que las otras celdas representan a los isótopos radiactivos.

A lo largo de la historia, principalmente dos modelos han tratado de explicar la estructura de los núcleos, "el modelo de la gota líquida" y el "modelo de capas". El primero se basa en las similitudes de un núcleo con una gota de líquido incompresible para explicar sus propiedades macroscópicas. Pero este modelo no es capaz de predecir la existencia de ciertos números de nucleones (protones y neutrones) que hacían a los núcleos ser altamente estables. Este hecho fue observado por M. Goeppert Mayer [4] y también por Jensen et al. [5] en un trabajo independiente. Esta evidencia sugirió que los núcleos, al igual que los átomos tenían una cierta estructura de capas. A este modelo se le llamó "modelo de capas". Para poder reproducir todos los números mágicos se incluyó la interacción espín-órbita [6]. La figura 9.2 muestra las energías de partícula independiente en un modelo de capas que incluye los términos de oscilador harmónico y acoplamiento espín-órbita.

En general el modelo de capas explica muy bien la estructura de núcleos cercanos al valle de estabilidad. Para esos núcleos los números mágicos predichos por Mayer y Jensen son válidos, pero cuando nos vamos a núcleos con una alta asimetría en el número de neutrones y protones, esos números
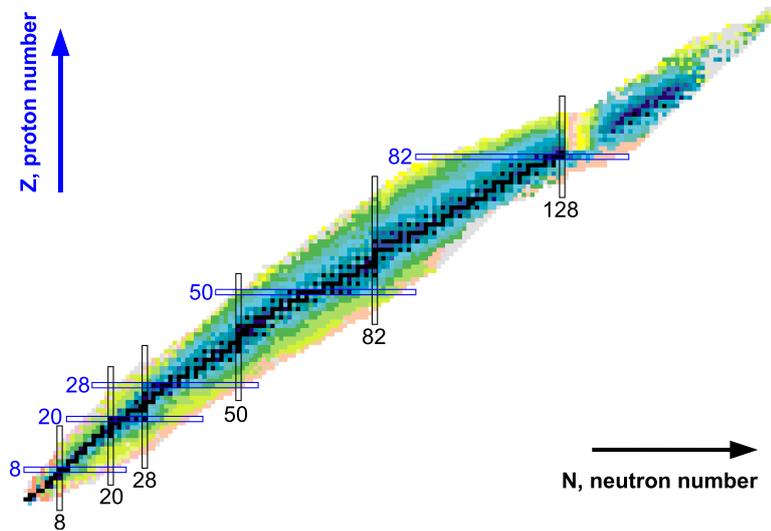
Figure 9.1: Carta de núcleos, mostrando el número de protones (Z) frente al número de neutrones (N). Los isótopos estables aparecen dentro de celdas negras. Las otras celdas representan los isótopos observados. El color depende de la vida media de dichos isótopos. Esta imagen ha sido tomada de *National Nuclear Data Center*, la información ha sido extraída de la base de datos de la carta de núcleos *Chart of Nuclides database*, http://www.nndc.bnl.gov/chart/.

mágicos dejan de ser válidos. Lo que se ha observado en los últimos años gracias a los avances tecnológicos que nos han permitido estudiar regiones lejos del valle de estabilidad, es que ciertas propiedades de los núcleos tienden a evolucionar cuando se presentan condiciones extremas.

Para estudiar las propiedades de núcleos ligeros ricos en neutrones, en Agosto de 2010 se realizó el experimento en cinemática inversa S393 en el laboratorio GSI Helmholtzzentrum für Schwerionenforschung, en Darmstadt [11], Germany. El mecanismo de reacción utilizado fue el quasi-free scattering, que a diferencia del knockout no se restringe al estudio de las capas más superficiales sino que permite estudiar las capas más profundas de los núcleos. En este tipo de reacciones, un nucleón (protón o neutrón) del proyectil colisiona con un protón del blanco como si ambas partículas fuesen libres y no existe interacción alguna entre el núcleo que sobrevive a la reacción (se considera un mero espectador) y los dos nucleones salientes.

En unos veinte días de haz se recogieron datos en el setup experimental de LAND-R^{3}B para diferentes settings de A/Q cubriendo la región desde
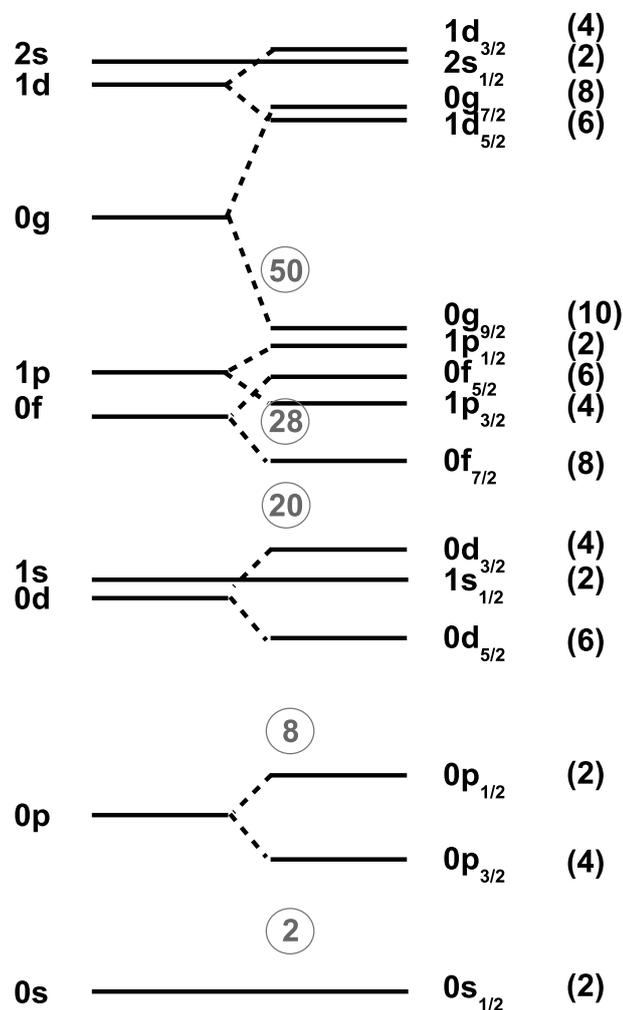
Figure 9.2: Esquema de los niveles de nergía en el modelo de capas de partícula independiente incluyendo los términos de oscilador harmónico y acoplamiento espín-órbita. Para cada nivel se indican los números cuánticos: n, l y j. Dentro de los paréntesis se indican las ocupaciones de las diferentes capas. Los números mágicos aparecen en color gris dentro de un círculo.

Z = 4 hasta Z = 10. Los estudios que se pretenden realizar con los datos tomados en este experimento son muy diversos y comprenden temas como: medidas de reacciones de interés astrofísico relevantes para el proceso r de nucleosíntesis y reacciones de knockout para estudiar la evolución de las capas y las estructuras de clusters, no sólo para núcleos cercanos a la línea de goteo sino también para aquellos que están más allá de ella.

El principal objetivo de este trabajo es el estudio de núcleos en la región

cercana a N = 14 para Z = 7, 8. Recientemente, se ha descubierto que esta región de la carta de núcleos es un cierre de sub-capa en el caso de los isótopos de oxígeno, pero existen evidencias de que este cierre se debilita para los nitrógenos e incluso desaparece en los carbonos. Para intentar esclarecer este hecho, y aportar nueva información en esta exótica región de la carta de núcleos poco conocida, hemos investigado las reacciones de quasi-free scattering (p,pn) y (p,2p) sufridas por los proyectiles ^{21}N y ^{23,22}O, y también los canales de evaporación de un neutrón para el estudio de los estados no ligados de estos núcleos.

Para obtener los isótopos de interés, se produjo un haz primario ^{40}Ar en una fuente de iones y se inyectó en un acelerador lineal, donde se aceleró hasta una energía de aproximadamente 490 AMeV. A continuación, este haz se dirigió hasta el separador de fragmentos (FRS), donde se produce y selecciona el haz secundario. A la entrada del FRS se colocó un blanco de producción de Be de 4.011 g/cm^2. Al golpear este blanco, por fragmentación nuclear se producen una serie de isótopos que luego son separados en el FRS dependiendo de su A/Q. Cuando una partícula con carga Q y masa A viaja a través de un campo manético de intensidad B experimenta la fuerza de Lorentz. Si la velocidad inicial de la partícula β es perpendicular al campo magnético uniforme, la fuerza magnética se iguala a la fuerza centrípeta, y por lo tanto, la partícula se moverá en un círculo de radio ρ, con

$$B\rho = \frac{p}{Q} \propto \frac{A}{Z} \cdot \beta\gamma \tag{9.1}$$

donde p es el momento de la partícula, Q se puede sustituir por Z ya que no existen estados de carga y γ es el factor de Lorentz. La selección de un núcleo con un A y Z determinados, se realiza a partir de la selección de intensidad de campo magnético B, ya que el radio ρ viene fijado por la geometría de los imanes del FRS. El FRS, además cuenta con la presencia de detectores que permiten determinar la trayectoria de los núcleos, en particular en este experimento se usaron dos centelleadores colocados en planos focales diferentes, que en combinación con otros detectores del dispositivo experimental LAND-R^{3}B permitieron la identificación de los fragmentos en velocidad.

Una vez se han seleccionado las especies deseadas, se conducen al área experimental (Cave C) donde se encuentra el setup (ver figura 9.3). En la primera parte de Cave C (antes del blanco) se identifican los núcleos en carga y en velocidad, usando medidas de pérdida de energía y tiempo de vuelo, respectivamente. A continuación, los isótopos colisionan con el blanco de reacción que está situado dentro de una cámara de vacío rodeado de ocho detectores de silicio que se usan para medidas de pérdida de energía (carga)

y posición (en X e Y). La cámara de vacío está a sus vez rodeada por un calorímero que se usa para medir la energía de los rayos γ producidos al de-sexcitarse los núcleos tras la colisión. Este detector, también se usa para identificar los eventos que se han producido por quasi-free scattering. Después de la reacción, los fragmentos que viajan hacia delante atraviesan un imán que los deflecta hacia las distintas ramas (neutrones, protones, partículas cargadas) de acuerdo a su carga y masa. Los neutrones, que no se desvían al pasar por el imán, van directamente a un detector de neutrones que mide su energía y distribución angular. La rama de fragmentos pesados, está compuesta por tres detectores, dos detectores de fibras que miden la posición de los núcleos en la dirección horizontal y el último mide el tiempo de vuelo y la posición en X y en Y. En la tercera rama se mide la posición y velocidad de los protones.

Conclusiones

Para poder obtener información estructural de estos núcleos, se han estudiado los siguientes observables físicos: secciones eficaces, distribuciones de momento, rayos γ y energía de excitación.

La sección eficaz es un observable físico que refleja la probabilidad de que una reacción nuclear ocurra. En la tabla 9.1 aparecen tabuladas las secciones eficaces inclusivas para los diferentes canales. En general, se observa que las secciones eficaces de los canales (p,pn) son mayores que las de los canales (p,2p). Este hecho puede explicarse teniendo en cuenta una serie de factores. El primero de ellos es que estamos estudiando núcleos ricos en neutrones y entonces existen más neutrones en el núcleo disponibles para reaccionar. Los factores espectroscópicos de los neutrones extraídos de la capa $0d_{5/2}$ son mayores porque esa capa esta casi llena en los casos que estamos estudiando. Además, la energía de ligadura de los neutrones más externos es menor que la de los protones, haciendo que sea más fácil arrancar un neutrón. Las interacciones p-p y p-n, son las resonables del arranque de un nucleón. En la región de energías en la que estamos trabajando (400 - 500 MeV), la sección eficaz de interacción n-p es mayor que la de p-p [78] contribuyendo de este modo al aumento de la sección eficaz de los canales (p,pn). Pero, la mayor contribución al incremento de la sección eficaz de los canales (p,pn), es el hecho de que en (p,2p) las dos partículas en el estado final son idénticas permitiendo sólo la configuración T = 1. Sin embargo, en los canales (p,pn) las configuraciones T = 0 y T = 1 están permitidas, teniendo la primera una sección eficaz unas cuantas veces mayor que la segunda. Estos cálculos han sido realizados por A. Moro [84]. Se ha estudiado también cual es la
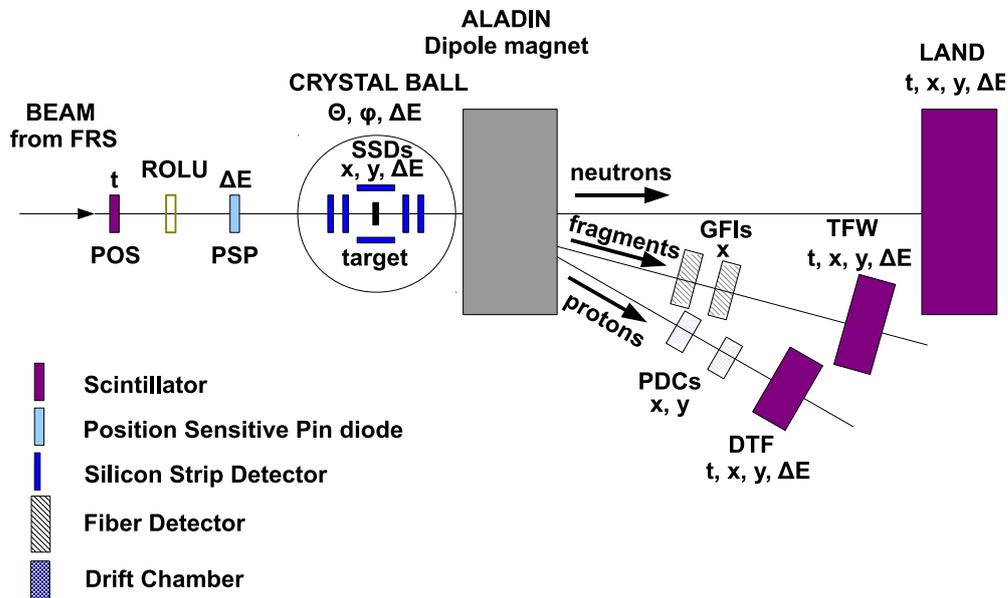
Figure 9.3: Esquema del dispositivo experimental usado en el experimento S393. El haz viene desde la izquierda y encuentra el centelleador POS que junto con el último detector del FRS mide el tiempo de vuelo que nos permite identificar los fragmentos en velocidad. Después está colocado ROLU, que está compuesto por cuatro plásticos centelleadores que pueden moverse para definir el tamaño y la posición del haz en el blanco. El siguiente detector es PSP se usa para medidas de posición y pérdida de energía (Q). En la zona del blanco tenemos ocho detectores de silicio; los cuatro de la línea de haz se utilizan para determinar las trayectorias de los fragmentos e identificarlos en carga; los cuatro que rodean al blanco se usan para la identificación de los eventos producidos por el mecanismo de reacción quasi-free scattering. Rodeando al blanco tenemos el calorímetro Crystal Ball para medidas de rayos γ y partículas ligeras emitidas en el poceso de quasi-free scattering. Los siguientes elementos del dispositivo experimental son: ALADIN: dipolo de gran aceptancia que desvía las partículas dependiendo de su A/Q; LAND: determinación de trayectorias y momento de los neutrones; GFI's: medida de la posición horizontal de los fragmentos pesados; TFW : posición en X e Y, pérdida de energía y tiempo de vuelo de los fragmentos pesados; DCHs: reconstrucción de la trayectoria de los protones; DTF: medidas de posición, pérdida de energía y tiempo de vuelo de los protones.

dependencia de la seccción eficaz con el número de neutrones y protones, para los canales (p,pn) y (p,2p) respectivamente. Se observa para el (p,pn) que la sección eficaz del ^{23}O (N = 15) es mayor que la del ^{21}N y ^{22}O (N = 14). Esto es debido a que el neutrón de valencia del ^{23}O tiene una energía de separación menor que los otros núcleos y también puede explicarse en términos del modelo de capas donde la N = 14 constituye una capa cerrada con seis neutrones llenando la capa $0d_{5/2}$, mientras que la N = 15 tiene un único neutrón de valencia en la capa $1s_{1/2}$. Este comportamiento de la N = 14 ya ha sido observado con anterioridad en trabajos previos como [17, 18, 19]. Por primera vez se han estudiado las capas de protones para estos núcleos mediante las reacciones (p,2p). Los protones de valencia de estos núcleos se encuentran todos en la misma capa, la $0p_{1/2}$. La diferencia entre el nitrógeno y los oxígenos, es que estos últimos tienen un protón más y por consiguiente es más probable arrancarles uno.

Reacción	σ(mb)
^{21}N(p,pn)^{20}N	43.1±9.0
^{21}N(p,2p)^{20}C	2.08±0.49
^{23}O(p,pn)^{22}O	63±17
^{23}O(p,2p)^{22}N	5.4±1.3
^{22}O(p,pn)^{21}O	36.1±7.2
^{22}O(p,2p)^{21}N	5.28±0.58

Table 9.1: Secciones eficaces inclusivas para las reacciones (p,pn) y (p,2p) de los proyectiles ^{21}N, ^{23}O y ^{22}O, corregidas por la eficiencia de Crystal Ball y en un blanco de hidrógeno.

La anchura y la forma de las distribuciones de momento contienen la información acerca de la estructura de los proyectiles. El dispositivo experimental usado posee mejor resolución para el momento transversal que para el longitudinal, por lo tanto las conclusiones extraídas en este trabajo se han basado en el estudio de esta componente. En la tabla 9.2, se muestran los resultados para la anchura a mitad de altura (FWHM) para todos los canales estudiados. Para obtener la información de la estructura, se realizó un estudio similar al realizado para la sección eficaz. Se ha observado que la FWHM decrece con el aumento del número de neutrones. Esto puede ser explicado haciendo uso del modelo de capas, ya que los neutrones de valencia para N

= 14 están en la capa $0d_{5/2}$ que tiene momento angular l = 2, sin embargo el neutrón de valencia para N= 15 están en la capa $1s_{1/2}$ que posee un momento angular l = 0. Por lo tanto la distibución de momento de l = 0 es más estrecha. En los canales (p,2p), se observa que la FWHM del ^{22}O es mayor que la del ^{21}N, esto sucede porque el ^{22}O está en capa cerrada lo cual hace que el núcleo sea más compacto espacialmente y por lo tanto su distribución de momento es más extensa. Para hacer un estudio más detallado de las distribuciones de momento, los datos experimentales han sido comparados con cálculos teóricos que nos han permitido obtener información espectroscópica.

Reacción	FWHM (MeV/c)
^{21}N(p,pn)^{20}N	189.97±33.40
^{21}N(p,2p)^{20}C	203.86±40.61
^{23}O(p,pn)^{22}O	107.56±25.25
^{23}O(p,2p)^{22}N	95.12±50.92
^{22}O(p,pn)^{21}O	240.49±16.22
^{22}O(p,2p)^{21}N	254.54±11.77

Table 9.2: Transversal momentum distribution FWHM for the (p,pn) and (p,2p) reactions for the projectiles ^{21}N, ^{23}O and ^{22}O.

Los espectros de rayos γ para los núcleos ^{22}O, ^{21}N, ^{21}O y ^{20}N han sido estudiados midiendo en coincidencia los fragments salientes de la reacción con los rayos γ en el detector Crystal Ball. Para los isótopos ^{22}O, ^{21}N and ^{21}O, las intensidades relativas de los rayos γ o secciones eficaces exclusivas de su estado excitado han sido determinadas. Se ha encontrado, a través de la observación de los rayos γ con energías de 3199 y 1383 keV, que ^{22}O puede describirse como una combinación del core ^{21}O en su estado fundamental acoplado a un neutron el la capa $0s_{1/2}$, un core de ^{21}O en su primer estado excited (3199 keV) 2^+ acoplado a un neutrón en la caps $0d_{5/2}$ y un core de ^{21}O en su segundo estado excitado (4582 keV) 3^+ acoplado a un neutrón en la capa $0d_{5/2}$. Los cálculos de las intensidades relativas realizados están en buen acuerdo con resultados previos de [17, 85]. El estudio del espectro de rayos γ del ^{21}N ha revelado que el ^{22}O puede ser descrito como una combinación del core de ^{21}N o bien en su estado fundamental (espín y paridad $1/2^-$) acoplado a un protón en la capa $0p_{1/2}$ o en su primer estado excitado $3/2^-$, donde emitirá un rayo γ con una energía de 1177 keV. Siendo la sección eficaz

exclusiva del estado $3/2^-$ (1.7±0.4) mb. Del estudio del espectro de rayos γ del ^{21}O se ha obtenido que el estado fundamental del ^{22}O puede ser descrito como el estado fundamental del ^{21}O acoplado a un neutrón en la capa $0d_{5/2}$ o como el primer estado excitado a 1218 keV acoplado a un neutrón en la $1s_{1/2}$. La sección eficaz exclusiva de este último caso es de $(0.85^{+0.97}_{-0.85})$ mb.

Cuando el núcleo posee una energía de excitación que está por encima de algún umbral de separación de partícula, la emisión de rayos γ compite con la emisión de otras partículas. A través de la reconstrucción de la energía de excitación es posible el estudio de los canales no ligados situados en el continuo. En nuestro caso se han estudiado los canales ^{23}O(p,pn)^{22}O* $\rightarrow^{21}$O+n, ^{22}O(p,pn)^{21}O* $\rightarrow^{20}$O+n y ^{21}N(p,pn)^{20}N* $\rightarrow^{19}$N+n por medio de la detección en coincidencia del fragmento producido después de la evaporación y el neutrón. Estos estudios han servido para comparar en el caso de la energía de excitación del ^{21}O con resultados previos obtenidos por B. Fernández-Domínguez et al. [91]. Se observa en este trabajo la existencia de dos resonancias, una a 4.77 MeV y otra a 6.17 MeV [91]. El estudio del espectro de energía de excitación del ^{20}N y del ^{22}O revela existencia de tres resonancias a 4.41±0.07, 5.52±0.10 y 6.74±0.50. Los resultados obtenidos son compatibles con [91]. La distribución de energía de excitación analizada para la reacción el ^{22}O, a través de la ^{23}O(p,pn)^{22}O* $\rightarrow^{21}$O+n. A pesar de que este caso tiene muy poca estadística, el hecho de que el espectro comience justo por encima de la energía de separación de ^{22}O podría ser un indicativo de la existencia de una resonancia. La reconstrucción del espectro de energía de excitación para el ^{20}N permitió la determinación de dos resonancias a energías de 3.2±0.3 MeV y 6.77 MeV. La observación de la primera resonancia podría confirmar el resultado previo obtenido en [19], donde observaron un estado en el continuo a 2.943 MeV.

Appendices

Appendix A

SSDs alignment

In this appendix are shown some results of the SSDs alignment performed using a linear least squares fit. The positions of three of the four in-beam SSDs were varied to determine the configuration with the minimum distance between the real hits in the SSDs detectors and the ones defined by a straight ion trajectory. Two and three dimensional plots for every two offset combination are shown in figure A.1 for the X coordinates and in figure A.2 for the Y coordinates. The plots on the left show one SSD offset versus another. The χ^2 values are given by the color scale, where violet indicates the smallest. The black dots in the two dimensional plots mark the position of the minimum obtained. It is observed from the plots a strong correlation between the offsets of the first and second SSD, which is not observed with the fourth SSD. This is due to the fact that the third SSD positions are fixed, so when the first is moved in one direction the second moves in the same. This observation was also confirmed by studying the covariance matrix and the global correlation coefficients.
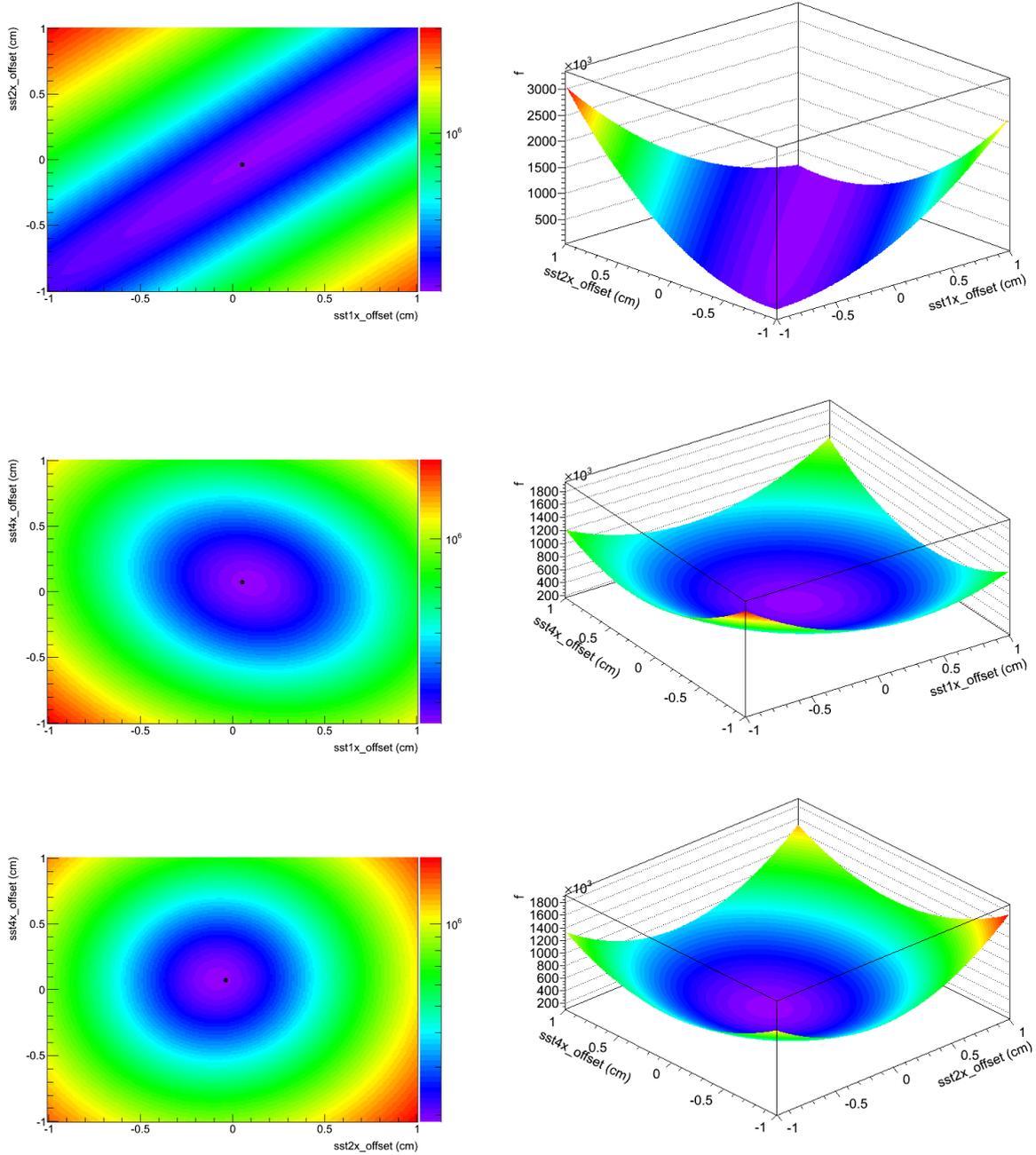
Figure A.1: Functional maps for the X coordinates in two (left) and three (right) dimensional plots for each set of two parameters. The different SSDs offsets mapped are in the X and Y axes. The Z axis is the functional value, shown in the color scale in the left plots and in color and height in the right plots. The minimal areas can be distinguished in the plots, highlighted by a dot.
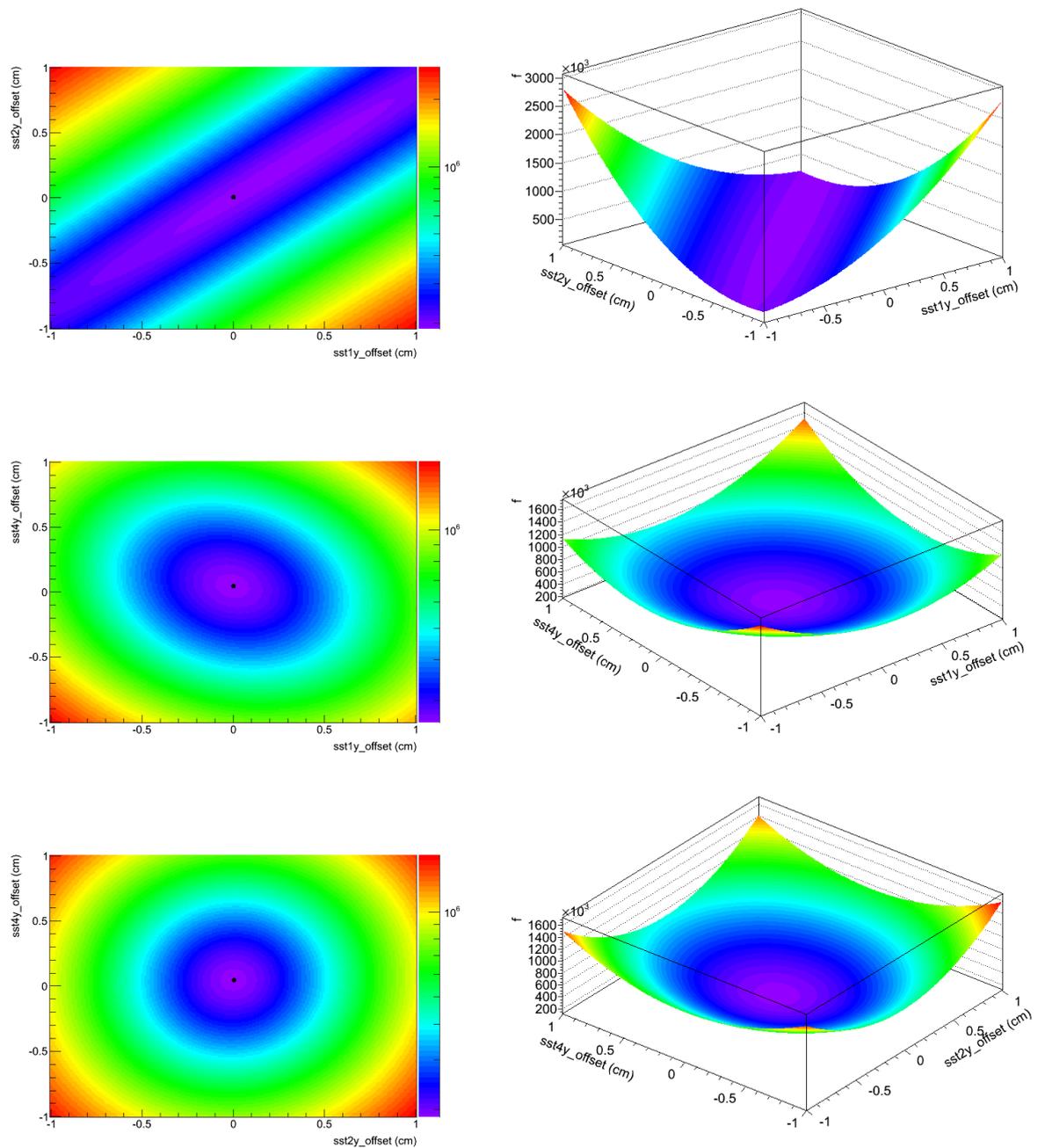
Figure A.2: Functional maps for the Y coordinates in two (left) and three (right) dimensional plots for each set of two parameters. The minimal areas can be distinguished in the plots.

Appendix B

Cross sections

This appendix contains a table summarizing the total inclusive cross sections for the projectiles ^{21}N, ^{23}O and ^{22}O. The table contains the results for the different targets and using the two analysis methods described in Section 6.1.1. The final inclusive cross sections resulting from this work for the (p,pn) and (p,2p) reactions can be found in Section 8.

Target	Reaction	2-dimensional σ(mb)	1-dimensional σ(mb)
CH_2	$^{21}N(p,pn)^{20}N$	129±16	130±15
C	$^{21}N(p,pn)^{20}N$	43.8±8.0	42.9±7.8
H	$^{21}N(p,pn)^{20}N$	42.4±8.9	43.7±8.6
CH_2	$^{21}N(p,2p)^{20}C$	5.70±0.56	5.76±0.55
C	$^{21}N(p,2p)^{20}C$	1.69±0.49	1.46±0.45
H	$^{21}N(p,2p)^{20}C$	2.00±0.37	2.15±0.35
CH_2	$^{23}O(p,pn)^{22}O$	161±28	152±26
C	$^{23}O(p,pn)^{22}O$	35±18	26±15
H	$^{23}O(p,pn)^{22}O$	63±17	63±15
CH_2	$^{23}O(p,2p)^{22}N$	12.7±1.8	10.2±1.9
C	$^{23}O(p,2p)^{22}N$	1.1±1.0	0.67±1.1
H	$^{23}O(p,2p)^{22}N$	5.8±1.0	4.8±1.1
CH_2	$^{22}O(p,pn)^{21}O$	120±13	135±14
C	$^{22}O(p,pn)^{21}O$	49.4±5.9	60.6±7.3
H	$^{22}O(p,pn)^{21}O$	35.4±7.1	37.0±8.1
CH_2	$^{22}O(p,2p)^{21}N$	15.05±0.56	14.01±0.51
C	$^{22}O(p,2p)^{21}N$	4.17±0.41	3.77±0.44
H	$^{22}O(p,2p)^{21}N$	5.44±0.34	5.12±0.34

Table B.1: Inclusive cross sections for the (p,pn)- and (p,2p)-type reactions for the projectiles ^{23}O, ^{22}O and ^{21}N, corrected by the Crystal Ball efficiency.

Appendix C

Inclusive momentum distributions

This appendix contains the longitudinal and transversal components of the momentum distribution for the different reactions studied in this work. The longitudinal and the transversal component of the momentum distributions were measured in the laboratory frame and then transformed to the projectile's rest frame. The reaction channels ^{23}O(p,pn)^{22}O, ^{23}O(p,2p)^{22}N, ^{22}O(p,pn)^{21}O and ^{22}O(p,2p)^{21}N are presented in the next figures. On the left hand side the momentum distributions for the CH$_2$, carbon and empty targets are shown and on the right hand side the momentum distributions for the hydrogen target are shown. Figures C.1, C.2, C.3 and C.4 show the longitudinal momentum distributions in laboratory frame for the channels ^{23}O(p,pn)^{22}O, ^{23}O(p,2p)^{22}N, ^{22}O(p,pn)^{21}O and ^{22}O(p,2p)^{21}N, respectively. For the same reactions, figures C.5, C.6, C.7 and C.8 show the longitudinal momentum distributions in the rest frame of the projectile. Finally, again for the same reactions, figures C.9, C.10, C.11 and C.12 show the transversal momentum distributions in laboratory frame.
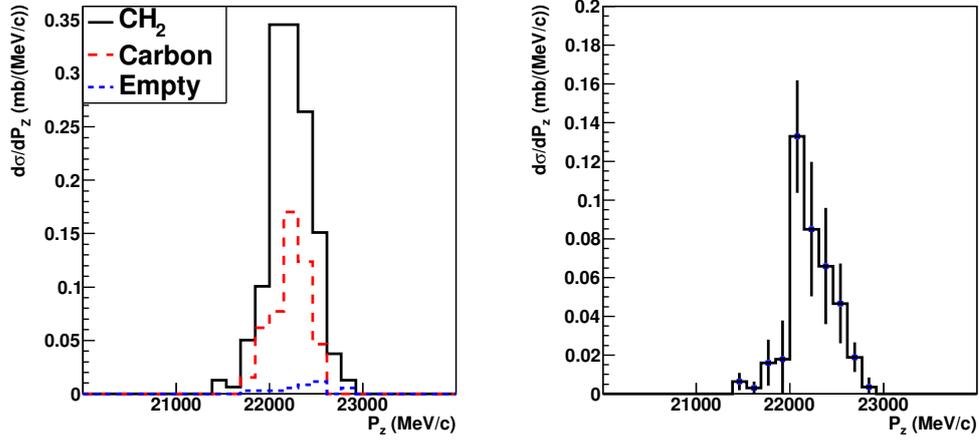
Figure C.1: Longitudinal momentum distributions in laboratory frame for the channel ^{23}O(p,pn)^{22}O.
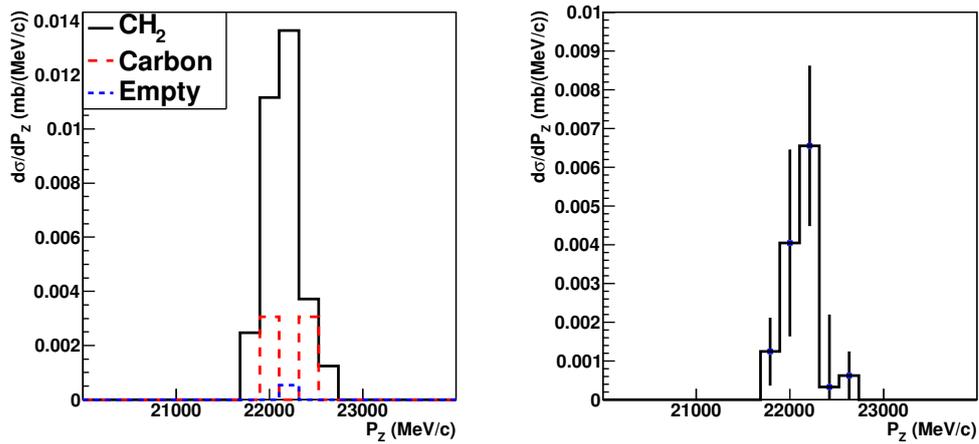
Figure C.2: Longitudinal momentum distributions in laboratory frame for the channel ^{23}O(p,2p)^{22}N.
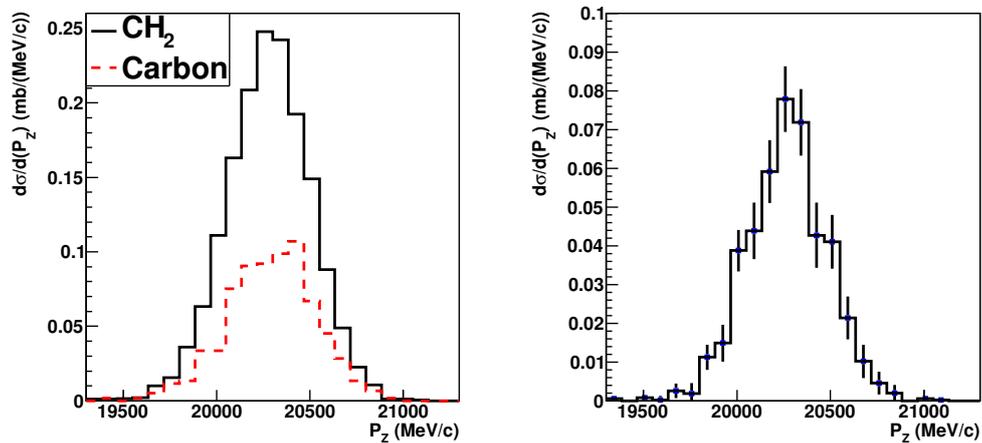
Figure C.3: Longitudinal momentum distributions in laboratory frame for the channel ^{22}O(p,pn)^{21}O.
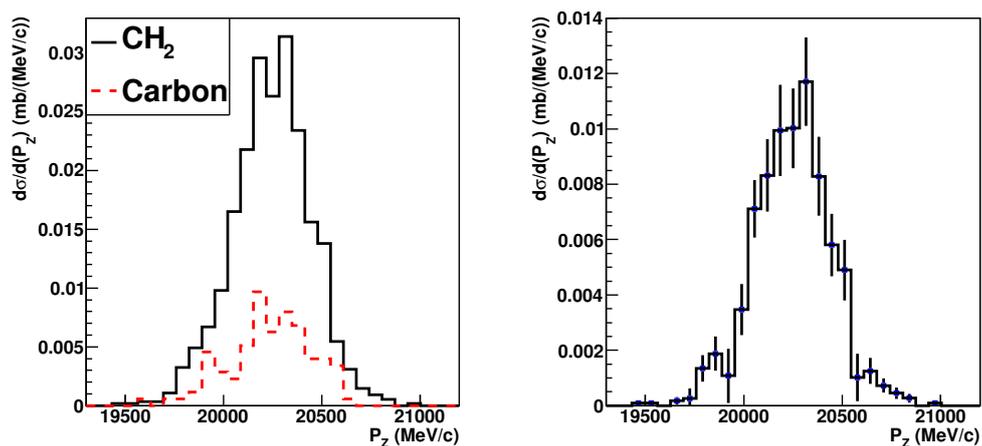
Figure C.4: Longitudinal momentum distributions in laboratory frame for the channel ^{22}O(p,2p)^{21}N.
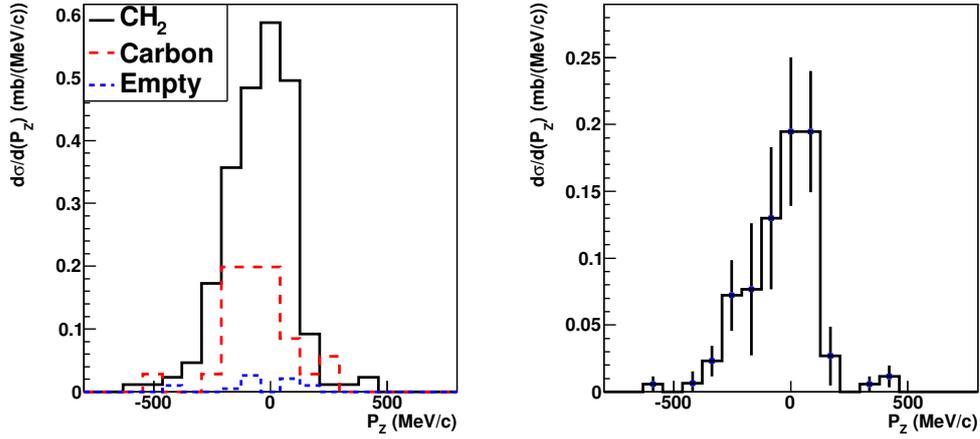
Figure C.5: Longitudinal momentum distributions in the rest frame of the projectile for the channel $^{23}O(p,pn)^{22}O$.
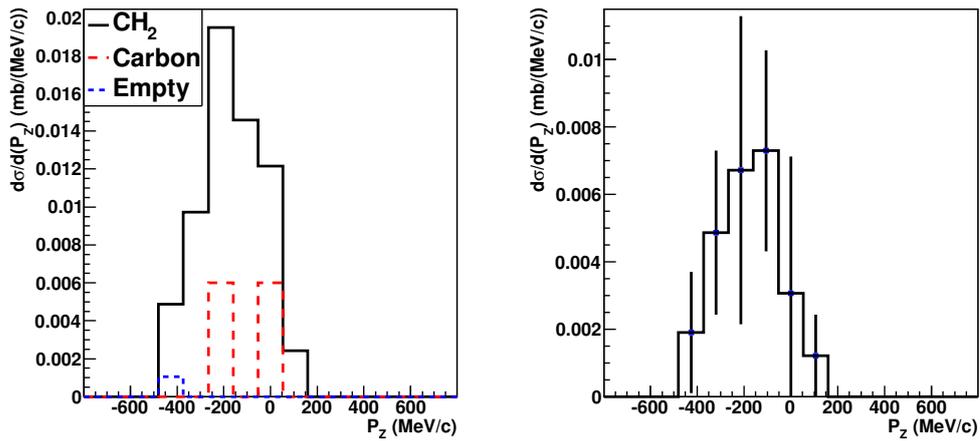
Figure C.6: Longitudinal momentum distributions in the rest frame of the projectile for the channel $^{23}O(p,2p)^{22}N$.
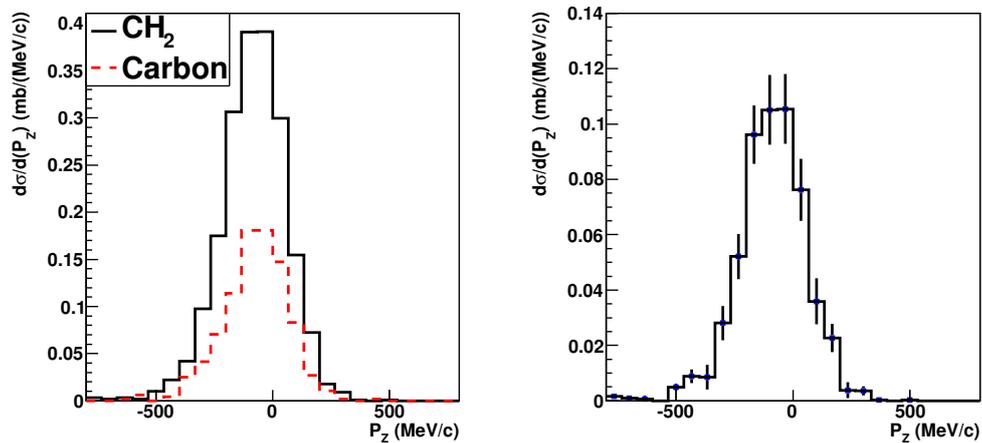
Figure C.7: Longitudinal momentum distributions in the rest frame of the projectile for the channel ^{22}O(p,pn)^{21}O.
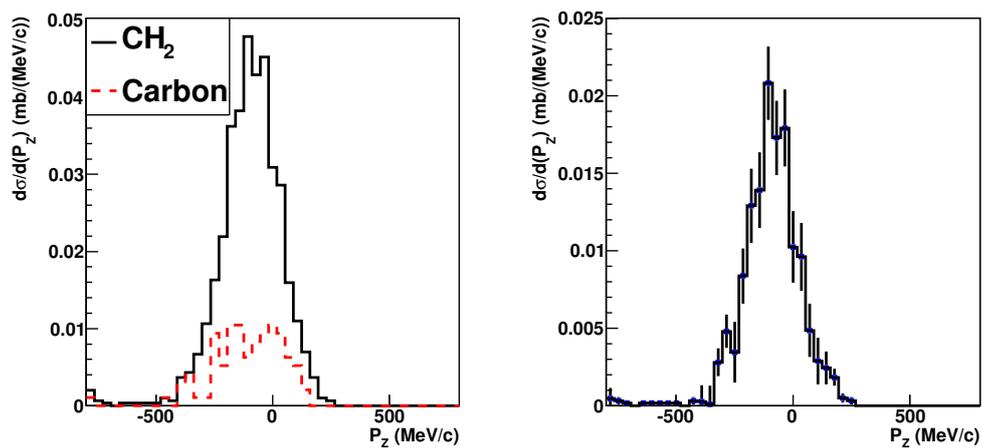
Figure C.8: Longitudinal momentum distributions in the rest frame of the projectile for the channel ^{22}O(p,2p)^{21}N.
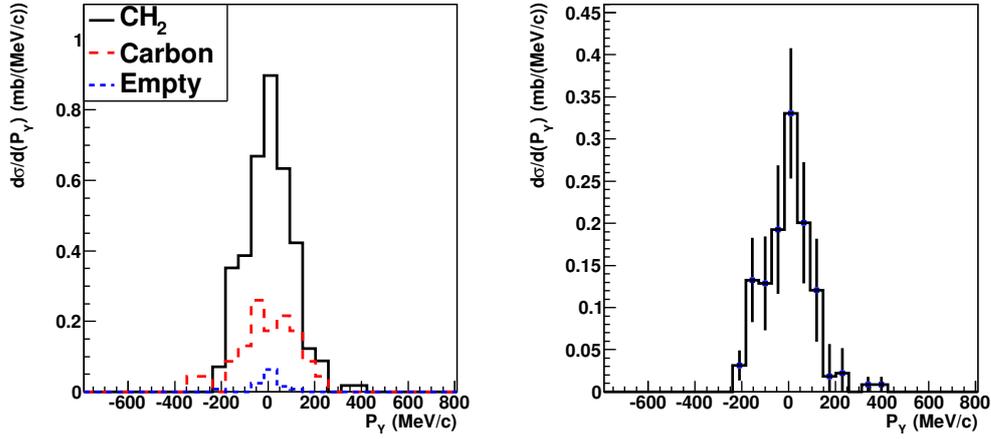
Figure C.9: Transversal momentum distributions in laboratory frame for the channel $^{23}O(p,pn)^{22}O$.
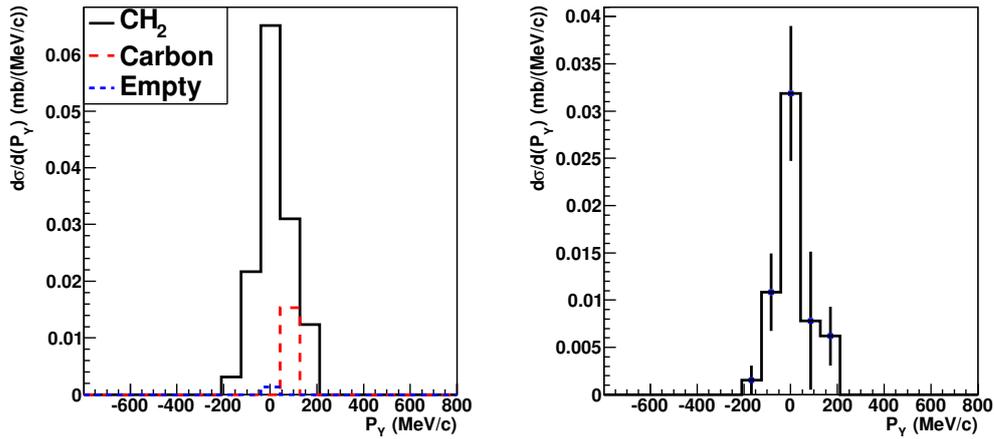
Figure C.10: Transversal momentum distributions in laboratory frame for the channel $^{23}O(p,2p)^{22}N$.
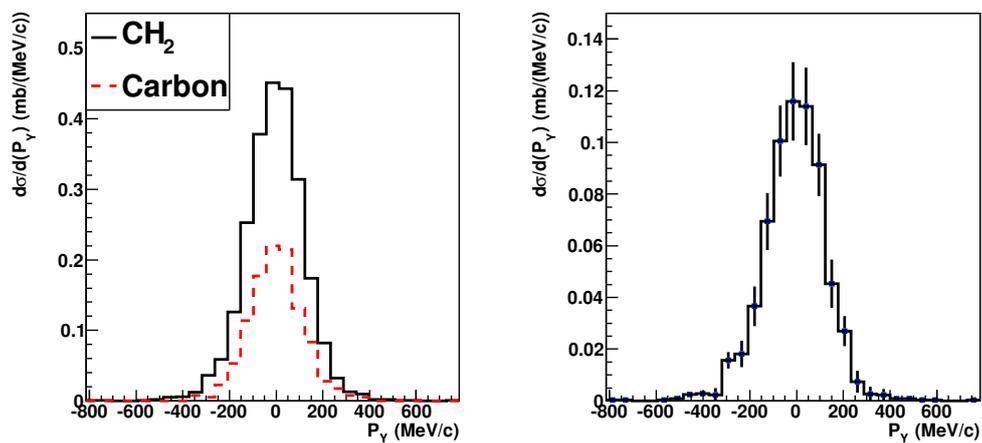
Figure C.11: Transversal momentum distributions in laboratory frame for the channel $^{22}O(p,pn)^{21}O$.
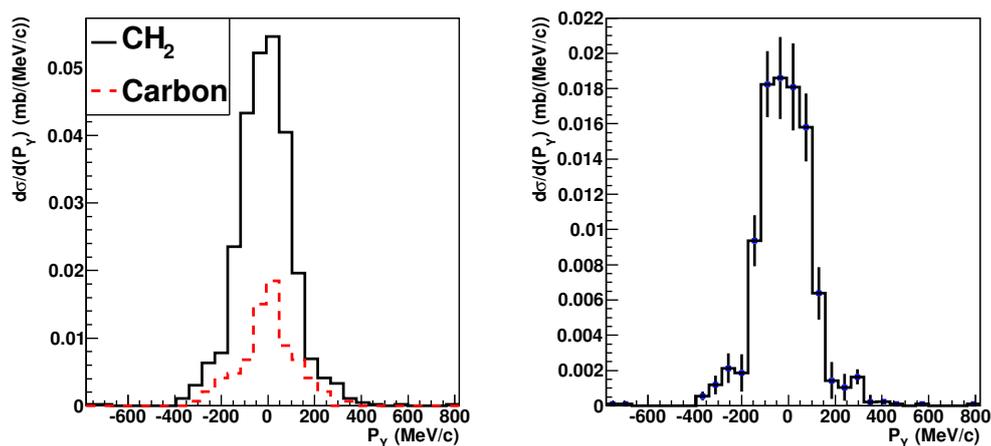
Figure C.12: Transversal momentum distributions in laboratory frame for the channel $^{22}O(p,2p)^{21}N$.

Bibliography

[1] E. Rutherford, *The scattering of alpha and beta particles by matter and the structure of the atom.* Philosophical Magazine, vol. 21, 669-688 (1911)

[2] David J. Rowe, John L. Wood, *Fundamentals of nuclear models.* World Scientific Publishing Co. Pte. Ltd. (2010)

[3] C. Bertulani, *Nuclear Physics in a Nutshell.* Princeton University Press (2007)

[4] M. G. Mayer, *On Closed Shells in Nuclei.* Phys. Rev. 74, pp. 235 - 239 (1948)

[5] O. Haxel, J. H. Jensen, and H. E. Suess, *On the "Magic Numbers" in Nuclear Structure.* Phys. Rev. Volume 75, 1766 - 1766 (1949)

[6] M. G. Mayer, *Nuclear Configurations in the Spin-Orbit Coupling Model. I. Empirical Evidence.* Phys. Rev. 78, 16-21 (1950)

[7] Lawrence Berkeley National Laboratory, http://www.lbl.gov/

[8] I. Tanihata et al., *Measurements of Interaction Cross Sections and Nuclear Radii in the Light p-Shell Region.* Phys. Rev. Lett. 55, 2676-2679 (1985)

[9] P. G. Hansen and J. A. Tostevin, *Direct Reactions with Exotic Nuclei.* Annual Review of Nuclear and Particle Science, vol. 53, pp. 219-261 (2003)

[10] N.A. Orr et al., *Momentum Distributions of ^9Li Fragment Following the Breakup of ^{11}Li.* Phys. Rev. Lett. 69 2050-2053 (1992)

[11] GSI, Helmholtzzentrum für Schwerionenforschung http://www.gsi.de.

[12] GANIL, Grand Accelerateur National d'Ions Lourds, http://www.ganil-spiral2.eu/

[13] RIKEN, Nishina Center for Accelerator-Based Science, http://www.rarf.riken.go.jp/Eng/

[14] R. Kanungo et al., *One-Neutron Removal Measurement Reveals ^{24}O as a New Doubly Magic Nucleus*. Phys. Rev. Lett. 102, 152501 (2009)

[15] C.R. Hoffman et al., *Evidence for a doubly magic ^{24}O*. Phys. Lett. B 672, 17-21 (2009)

[16] Robert V. F. Janssens, *Nuclear physics: Unexpected doubly magic nucleus*. Nature 459, 1069-1070 (2009)

[17] M. Staniou et al., *N=14 and N=16 shell gaps in neutron-rich oxygen isotopes*. Phys. Rev. C 69 034312 (2004)

[18] D. Sohler et al., *In-beam γ-ray spectroscopy of the neutron-rich nitrogen isotopes $^{19-22}N$*. Phys. Rev. C 77 044303 (2008)

[19] C. Rodriguez-Tajes et al., *Structure of ^{22}N and the N=14 subshell*. Phys. Rev. C 83 064313 (2011)

[20] M.Staniou et al., *Dissapearance of the N=14 shell gap in the C isotopic chain*. Phys. Rev. C 78 034315 (2008)

[21] J. A. Tostevin, *Core excitation in halo nucleus break-up*. J. Phys. G: Nucl. Part. Phys. 25 735 (1999)

[22] T. Berggren and H. Tyren, *Quasi-Free Scattering, Annual Review of Nuclear and Particle Science*. vol. 16, pp. 153-182 (1966)

[23] G. Jacob and T. A. Maris, *Quasi-Free Scattering and Nuclear Structure*. Reviews of Modern Physics, vol. 38, pp. 121-142 (1966)

[24] O. Chamberlain and E. Segrè., *Proton-Proton Collisions within Lithium Nuclei*. Phys Rev. vol. 87, pp. 81-83 (1952)

[25] J. B. Cladis, W. N. Hess, and B.J.Moyer, *Nucleon Momentum Distributions in Deuterium and Carbon Inferred from Proton Scattering*. Phys. Rev. vol. 87, pp. 425-433 (1952)

[26] H. Tyrén, T. A. Maris and P. Hillman, *Inner Shell Structure Of Nuclei*. Nuovo Cimento, 6, 1507-1509 (1957)

[27] https://www.gsi.de/en/work/research/nustarenna/kernreaktionen/activities/r3b.htm

[28] Valerii Panin: *Fully Exclusive Measurements of Quasi-Free Single-Nucleon Knockout Reactions in Inverse Kinematics.* PhD thesis, TU Darmstadt (2012)

[29] John Taylor: *Proton Induced Quasi-free Scattering with Inverse Kinematics.* PhD thesis, University of Liverpool (2011)

[30] Felix Wamers: *Quasi-free Knockout Reactions with the Proton-dripline Nucleus ^{17}Ne.* PhD thesis, TU Darmstadt (2011)

[31] https://www.gsi.de/en/research/fair.htm

[32] D. Cortina-Gil, *Direct reactions at relativistic energies, a new insight into the single-particle structure of exotic nuclei* (2013)

[33] The R3B Collaboration, *Neutron-rich Nuclei at and Beyond the Dripline in the Range Z=4 to Z=10 Studied in Kinematically Complete Measurements of Direct Reactions at Relativistic Energies.* S393 proposal (2010)

[34] C. Caesar, *Beyond the Neutron Drip-Line: Superheavy Oxygen Isotopes.* PhD thesis, TU Darmstadt (2012)

[35] A. Najafi, *Quasi-free knock-out reactions on oxygen isotopes* (talk). European Nuclear Conference (2012)

[36] P. Díaz-Fernández, *An investigation into quasifree scattering of neutron-rich carbon and nitrogen nuclei around N=14* (talk). European Nuclear Conference (2012)

[37] A. Herriques, *Neutron knockout of the halo nucleus ^{11}Be at Quasi-Free Scattering conditions* (talk). European Nuclear Conference (2012)

[38] P. Velho, *Study of ground state properties of halo nuclei via quasi-free scattering reactions at the R^3B setup* (talk). European Nuclear Conference (2012)

[39] H. Geissel et al., *The GSI projectile fragment separator (FRS): a versatile magnetic system for relativistic heavy ions.* Nucl. Instr. Meth. B 70 (1992)

[40] M. Stanoiu et al, *Fragment tracking with Si microstrip detectors.* GSI Scientific Report (2006)

[41] V. Metag et al., *The Darmstadt-Heidelberg-Crystal-Ball.* Proc. Geiger Memorial Meeting (1982)

[42] A. Henriques, *A new Trigger Logic system for the LAND/R³B setup*, Master Thesis, University of Lisbon (2012)

[43] J. Cub et al., *A large-area scintillating fibre detector for relativistic heavy ions.* Nucl. Instr. Meth. A 402 67-74 (1998)

[44] T. Blaich et al., *A large area detector for high-energy neutrons.* Nucl. Instr. Meth. A 314 136-154 (1992)

[45] Håkan T. Johansson, *Hunting Tools Beyond the Driplines.* PhD Thesis, Göteborg (2010)

[46] R. Plag, *Land02: featuring the unofficial guide to the unofficial version of land02, http://web-docs.gsi.de/~rplag/land02/*

[47] D. Rossi, *Investigation of the Dipole Response of Nickel Isotopes in the Presence of a High-Frequency Electromagnetic Field.* PhD thesis, Mainz (2009)

[48] Saúl Beceiro, *Coulomb Dissociation of ^{27}P at 498 AMeV: an indirect measurement of the astrophysical $^{26}Si(p,g)$ reaction.* PhD thesis, Universidade de Santiago de Compostela (2011)

[49] J. Alcaraz et al., *The alpha magnetic spectrometer silicon tracker: Performance results with proton and helium nuclei.* Nucl. Instr. Meth. A 593 376-398 (2008)

[50] The calibration was performed with a script package developed by Valerii Panin and modified by Matthias Holl.

[51] http:www.nndc.bnl.govnudat2

[52] Instructions to use the Crystal Ball calibration scripts http://web-docs.gsi.de/ rplag/land02/index.php?page=detectors/cb/CB_doc

[53] Scripts written by F.Wamers and O.Ershova (see ref. [52]) to calibrate the gamma energy branch of the Crystal Ball detector.

[54] Olga Ershova, *Coulomb Dissociation Reactions on Molybdenum Isotopes for Astrophysics Aplications.* PhD thesis, Frankfurt am Main (2011)

[55] Ronja Thies, *Prototype tests and pilot experiments for the R^3B scintillator-based detection systems.* Master Thesis, Göteborg (2011)

[56] K. Mahata, H.T. Johansson, S. Paschalis, H. Simon, T. Aumann, *Position reconstruction in large scintillating fibre detectors*. Nuclear Instruments and Methods in Physics Research A 608 331-335 (2009)

[57] Scripts written by Dominic Rossi to calibrate the TFW detector

[58] http://www-linux.gsi.de/∼weick/atima/

[59] http://www-linux.gsi.de/∼rplag/land02/index.php?page=tracking2

[60] R. Hagedorn., *Relativistic kinematics: A guide to the kinematic problems of high-energy physics*. W. A. Benjamin, Inc. (1964)

[61] Particle Data Booklet 2012. J. Beringer et al. (Particle Data Group), Phys. Rev. D86, 010001 (2012)

[62] R3BRoot instalation instructions and repository, http://fairroot.gsi.de/?q=node/11

[63] http://fairroot.gsi.de/

[64] http://root.cern.ch/

[65] http://wwwasd.web.cern.ch/wwwasd/geant/

[66] Geant (for GEometry ANd Tracking) is a platform for "the simulation of the passage of particles through matter", using Monte Carlo methods (http://geant4.web.cern.ch/geant4/). The two main reference papers for

[67] H. Álvarez-Pol, M. Al-Turany, D. Bertini and D. Kresan for the R^{3}B collaboration, *R3BRoot:a FAIRRoot-based development for the analysis and simulation of the R^{3}B experiment*. GSI Scientific Report (2012)

[68] Internal Report by Pablo Cabanelas (2013)

[69] P. Díaz Fernández, *Simulaciones en Geant4 para el prototipo del calorímetro CALIFA*. Tesina, Universidade de Santiago de Compostela (2009)

[70] L. Chulkov, private communication (2012)

[71] A.S. Goldhaber, *Statistical models of fragmentation processes*. Phys. Rev. B, 53 306-308 (1974)

[72] P. Van Isacker, G. Auger, and C. Grosjean, *Quantal versions of Goldhaber's fragmentation model*. Technical report, GANIL,CAEN (2002)

[73] William A. Friedman, *Heavy ion projectiles: A reexamination.* Phys. Rev. C, vol. 27, number 2 (1983)

[74] Matthias Holl, private communication (2013)

[75] Journal of Physics G: Nuclear and Particle Physics. Volume 33 July 2006

[76] R. Kanungo, *A new view of nuclear shells.* Phys. Scr. T152 014002 (2013)

[77] Dominic Rossi, private communication (2013)

[78] S. K. Charagi, S. K. Gupta, *Coulomb-modified Glauber model description of heavy-ion reaction cross sections.* Phys. Rev. C, vol. 41, number 4 (1990)

[79] N.S. Chant and P.G. Ross, *Distorted-wave impulse-approximation calculations for quasi-free cluster knockout reactions.* Phys. Rev. C vol 57 (1977); ibid, *Spin orbit effects in quasi-free knockout reactions.* Phys. Rev. C 27, 1060 (1983)

[80] L. D. Faddeev. Zh. Eksp. Teor. Fiz. 39, 1459 (1960)

[81] R. Crespo, private communication (2013)

[82] A. M. Moro, F. M. Nunes, *Transfer to the continuum and breakup reactions.* Nuclear Physics A, 767, 138-154 (2006)

[83] H. B. Jeppesen et al., *Study of ^{10}Li via the $^{9}Li(^{2}H, p)$ reaction at REX-ISOLDE.* Physics Letters B, 642(5), 449-454 (2006)

[84] A. Moro, private communication (2013)

[85] D.Cortina-Gil et al., *Shell structure of the new-dripline nucleus ^{23}O.* Phys. Rev. Lett 93, 062501 (2004)

[86] Carme Rodríguez Tajes, *Study of light neutron-rich nuclei via one-neutron knockout reactions.* PhD thesis, Universidade de Santiago de Compostela (2009)

[87] T. Aumann, C. A. Bertulani, J. Ryckebusch, *Quasi-free (p,2p) and (p,pn) reactions with unstable nuclei.* Submitted to Phys. Rev. C (2013)

[88] E. O. Alt, P. Grassberger, W. Sandhas, *Reduction of the three-particle collision problem to multi-channel two-particle Lippmann-Schwinger equations.* Nucl. Phys. B 2 (2): 167-180 (1967)

[89] R. Crespo, A. Deltuva, M. Rodríguez Gallardo, E. Cravo, and C. Fonseca, *Spectroscopy of unbound states under quasi-free scattering conditions: One-neutron knockout reaction of ^{14}Be.* Phys. Rev. C 79, 014609 (2009)

[90] OXBASH, B. A. Brown, H. Liu, A. Etchegoyen, N. S. Godwin, W. D. M. Rae, W. A. Richter, W. E. Ormand, E. K. Warburton, J. S. Winfield, L. Zhao and C. H. Zimmerman, MSU-NSCL report number 1289.

[91] B. Fernández-Domínguez et al., *Emergence of the N = 16 shell gap in ^{21}O.* Phys. Rev. C 84 011301 (2011)

[92] C. S. Sumithrarachchi, et al., *States in ^{22}O via β decay of ^{22}N.* Phys. Rev. C 81 014302 (2010)

Acknowledgements

This Thesis would have not been possible without the help and support of so many people which worked with me along these years. With these lines I would like to say them Thank you.

First of all I would like to say Thank you very much to my supervisor, Héctor Álvarez Pol. His work was not only guiding me but also helping me in the day by day tasks and giving me so many advices. Without him this Thesis could not be finished.

I would also like to thank to Dolores Cortina Gil, because she always had time to help me with my problems. Two persons who deserve a special mention are Manuel Caamaño Fresco and Beatriz Fernández Domínguez, because they helped me a lot in the daily work. Clearly without them it would be impossible to finish the PhD. With them I learned a lot about Nuclear Physics and I also had so many good moments discussing and talking about so many topics. I also want to say Thank you to all my officemates along these years: Saúl, Marisol, Yassid, Jossitt, Diego, Esther, Carme, Noe, Martín and José Luis. But specially I would like to express my gratitude to Marisol and Saúl, because they supported me not only in a profesional way. Also a special mention to Yassid, Jossitt, Esther and Diego because we expend so many hours in and out of the office. I want to say Thank you also to Benjamin Pietras for helping me a lot in the understanding of Nuclear Structure and also for correcting my English so many times. I would like to say Thank you to the Grupo Experimental de Núcleos y Partículas (GENP) for let me be part of this adventure called Nuclear Physics. Thanks to all the members of the GENP which shared some of these years with me.

Another two persons who contribute a lot in the interpretation of the results and I would like to thank, are Antonio Moro and Raquel Crespo.

Thanks to all the collaborators of the experiment S393 and to the R3B collaboration who made this Thesis much easier and who always were there to answer my millions of emails. Special thanks to: Thomas Aumann, Konstanze Boretzky, Michael Heil, Haik Simon, Ralf Plag, Dominic Rossi, Valerii Panin, Jon Taylor, Felix Wamers, Alina Movsesyan, Ana Henriques and Leyla

Atar.

Finally, I would like to say Thank you to my family. Specially to my husband Pablo, because the last year was specially stressful for me and he was always supporting me. He also help me in so many topics related with the Thesis. To my parents and syblings to be comprehensive and to understand my not so often visits. To my friends of Viveiro (Ana, Nuria, Natalia, Alba, Isa, ...) and to my friends in Santiago (Marisol, Anita, Mari Jose y Bárbara) I just want to say Thank you for been there always.

Thanks too to all the people that contributed to this Thesis in so many different ways.